PASSIVE FLOW CONTROL IN AN S-DUCT INTAKE

COMMANDE PASSIVE DE L'ÉCOULEMENT DANS UNE PRISE D'AIR SINUEUSE

A Thesis Submitted to the Division of Graduate Studies
of the Royal Military College of Canada
by

Courtney S. Rider, BASc

In Partial Fulfillment of the Requirements for the Degree of
Master of Applied Science in Aeronautical Engineering

April, 2021

© This thesis may be used within the Department of National Defence
but copyright for open publication remains the property of the author.

Acknowledgements

I would like to thank my supervisors, Dr. William D. E. Allan and Dr. Grant Ingram, for imparting a large amount of knowledge on aircraft engine design, experimental testing and computational modeling. The guidance and lessons they have provided has contributed greatly to my thesis and will remain with me.

I would also like to thank the other Masters and PhD students who have provided friendship and knowledge throughout this process. Specifically I would like to thank Satpreet Sidhu for his assistance in the experimental testing and discussion of results. I would also like to extend my thanks to the technical staff in the machine shop in the Mechanical and Aerospace Engineering Department for their ability to support the multitudes of research being performed. Last, but not least, I would like to thank my external friends and family for their continued support.

Abstract

The performance of aircraft depends to a great deal on engine behaviour, which is itself governed by that of its major components, including the compressor. Compressor efficiency is highly dependent on the flow distribution with which it is presented, since cyclic loading can cause fatigue, compressor rotating stall and/or engine surge. On some aircraft, where there is an embedded engine, or where propellers or gearbox require offset inlets, an S-duct is used. S-ducts direct and diffuse free-stream flow to the conditions required by the compressor. In this thesis an S-duct with operationally representative diffusion, offset and aspect ratio was chosen for an inlet Mach number of 0.8. The baseline S-duct was adapted with passive flow control, in the form of tubercles, along both inner radii of the S-trajectory. The tubercle profile has an asymmetric amplitude and a wavelength of 7% of the exit diameter, chosen based on previous successful work on S-ducts and airfoils, noting improved performance to reduced tubercle size. Experimental testing was performed in a new transonic wind tunnel on the baseline duct, a previously tested flow control duct and new flow control duct. Surface static pressure measurements along the duct meridian showed separation of flow on both inner radii, in the baseline duct. The first inner radius separation was reduced in size and the second was eliminated with the implementation of flow control. Total

and static pressure were measured at the Aerodynamic Interface Plane with a traversing five-hole *AeroProbe*. The total pressure recovery and total pressure distortion coefficients revealed performance improvement in the flow control ducts. Exit swirl reduction with the tubercled S-ducts suggest that secondary flows were less intense in the flow control ducts. The baseline results were compared computationally, and an automation system was created for use in future numerical campaigns. The computational work compared in trends but not magnitude to the experimental work. The $k - \omega$ SST turbulence model was used and was more successful than previous attempts at predicting separation points. Implementation of the automation system with this turbulence model is a solid step towards automating and optimizing S-duct design. Of significance, the tubercle geometry used in the flow control duct presented in this thesis was successful in mitigating or eliminating separation in an operationally representative S-duct in the transonic regime.

Résumé

La performance des avions dépend en grande partie des moteurs, et les performances des groupes motopropulseurs sont elles-mêmes régies par celles de leurs principaux composant, dont le compresseur. Le rendement du compresseur dépend fortement du champ de vitesse de l'écoulement entrant, car un chargement cyclique peut provoquer la fatigue, le décrochage et/ou le pompose du moteir. Sur certains appareils on le moteur intégré dans le fuselage du compressor, ou lorsque les hélices ou la boîte de vitesses imposent des prises d'air décalées, un conduit sinueux est employé. Les conduits sinueux diffusent et dirigent l'écoulement pour obtenir les conditions d'entrée requises par le compresseur. Dans ce mémoire, un conduit sinueux diffusant un décalage et un rapport de cadre représentatifs des conditions d'opération sont choisis pour un nombre de Mach à l'entrée de 0,8. Le conduit de référence a été adapté avec une commande passive de l'écoulement, sous la forme de tubercules, le long des deux rayons intérieurs de la trajectoire de la chicane. Le profil de tubercule avec un rapport d'amplitude asymétrique et une longueur d'onde égale à 7% du diameter de sortive a été choisi basé sur des travaux antérieurs sur les conduits en S, et de nouveaux travaux sur les profils aérodynamiques montrant une meilleure performance avec des tubercules de taille réduites. La référence, un conduit avec une commande pas-

sive de l'écoulement précédemment testé et un nouveau conduit ayant une commande d'écoulement différentes ont été testés dans une nouvelle soufflerie transsonique. Les mesures de pression statique à la surface le long du méridien du conduit ont montré une séparation de l'écoulement sur les deux rayons intérieurs pour le conduit de référence. Les régions de rayon intérieur, le premier et le second, ont été respectivement éliminées et réduites en taille avec la mise en œuvre de la commande de l'écoulement. Les pressions, totale et statique, ont été mesurées au plan d'interface aérodynamique avec une *AeroProbe* à cinq trous balayant le plan. Les coefficients de rendement et de distorsion de la pression totale ont révélé une amélioration des performances dans les conduits à commande passive de l'écoulement. La réduction du tourbillon de sortie avec les conduits sinueux tuberculés suggère que les écoulements secondaires étaient moins forts dans les conduits à commande passive de l'écoulement. Les résultats de base ont été comparés avec une simulation numérique, et un système d'automatisation du processus a été créé pour les simulations numériques futures. Les tendances des travaux numériques sont comparables à celles de résultats expérimentaux mais les valeurs absolues ne le sont pas. Le modèle de turbulence SST $k-\omega$ a été utilisé et s'est avéré plus efficace que les tentatives précédentes pour prédire les points de séparation. La mise en œuvre du système d'automatisation avec ce modèle de turbulence constitue un progrès dans l'automatisation et l'optimisation de la conception des conduits sinueux. Plus précisément, la géométrie du tubercule utilisée dans le conduit avec à commande de l'écoulement présenté dans cette thèse a réussi à atténuer ou à éliminer la séparation dans un conduit sinueux soumis à des conditions d'opérations représentatives dans le régime transsonique.

Contents

List of Tables

List of Figures

Nomenclature

Latin Letters

A	Amplitude of tubercle	mm
AR	Aspect ratio	–
C_p	Coefficient of pressure	–
D	Exit diameter	m
$DC(60)$	Circumferential distortion coefficient	–
$DPCP_{\text{ave}}$	Circumferential distortion coefficient	–
$DPRP_{\text{max}}$	Radial distortion coefficient	–
Ma	Mach number	–
p	Pressure	kPa
R	Ratio of duct parameters	–
Re	Reynolds number	–
SD	Swirl directivity at AIP	–
SI	Swirl intensity at AIP	–
SP	Swirl pairs coefficient at AIP	–
SS^+, SS^-	Mean swirl angle in a given sector at AIP in the positive and negative direction respectively	–

v	Secondary velocity	$\frac{\mathrm{m}}{\mathrm{s}}$

Greek Letters

α	Swirl angle at AIP	$^\circ$
δ	Uncertainty	$-$
γ	Total pressure loss coefficient	$-$
λ	Wavelength of tubercle	mm
ω	Uncertainty of measured variables	-
π	Total pressure coefficient	$-$
θ	Circumferential direction	-

Subscripts

$+$	Positive direction
$-$	Negative direction
0	Total condition
1	Inlet condition
2	Outlet condition
i	Annulus counter
j	60° sector at AIP
k	Circumferential index at AIP
m	Overall number of annulus sectors
LD	Length-to-diameter
OD	Offset-to-diameter
OL	Offset-to-length

s	Static condition
x	axial-location down duct from inlet

Acronyms

3D	3-Dimensional
AIP	Aerodynamic Interface Plane
BLI	Boundary Layer Ingesting
CFD	Computational Fluid Dynamics
CRV	Counter Rotating Vortex
csv	Comma separated values
DDES	Delayed Detached Eddy Simulation
FC	Flow Control
igs	Initial graphics exchange specification
LES	Large Eddy Simulation
PIV	Particle Image Velocimitry
RANS	Reynolds-Averaged Navier-Stokes
RMC	The Royal Military College of Canada
SA	Spalart-Allmaras
SAE	Society of Automotive Engineering
SST	Shear Stress Transport
VBA	Visual Basics Application
VG	Vortex Generators

1 Introduction

S-ducts are used in aircraft to direct oncoming air flow to the inlet of an embedded engine. Figure 1.1 shows a Falcon 900EX with an S-duct on the centre engine. Here the entrance to the S-duct is on the top of the aft fuselage, and the exhaust of the embedded engine is located under the empennage. While S-ducts are required for a 3-engine aircraft, they are also used in single engine aircraft, missiles, and automotive vehicles.

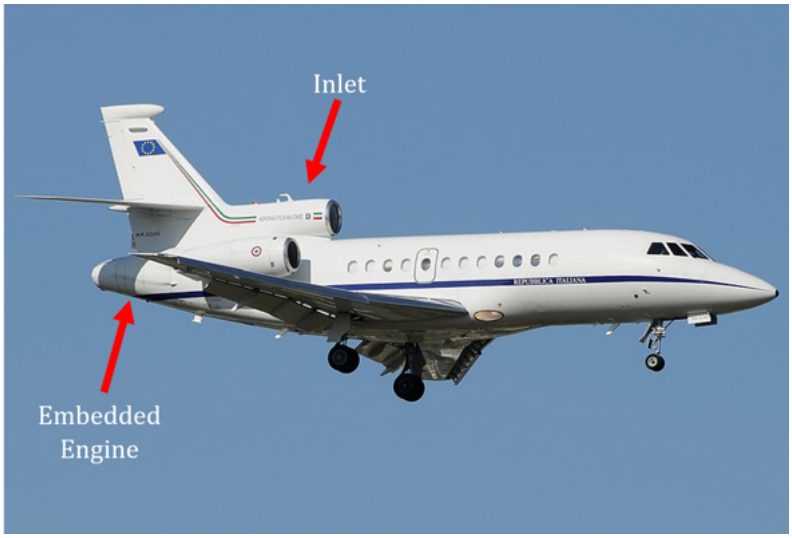

Figure 1.1: Falcon 900EX [1]

Figure 1.2: Section of Falcon 900EX showing S-duct [1]

Figure 1.2 shows a section of the nacelle removed and the S-duct itself is visible, connecting the inlet on the top of upper aft section of the fuselage to the engine embedded in the fuselage. The center engine in this image has been removed and there is clearly a gap beneath the vertical stabilizer where the engine would mount. This figure illustrates the role S-ducts play in redirecting air to enter the engine. S-ducts are also implemented where an upstream gearbox or propeller demand offset inlets. Their purpose remains to redirect and diffuse incoming air to the conditions required by the compressor. The double-bend S-duct often causes high-speed entrance flows to separate when encountering the inner radii.

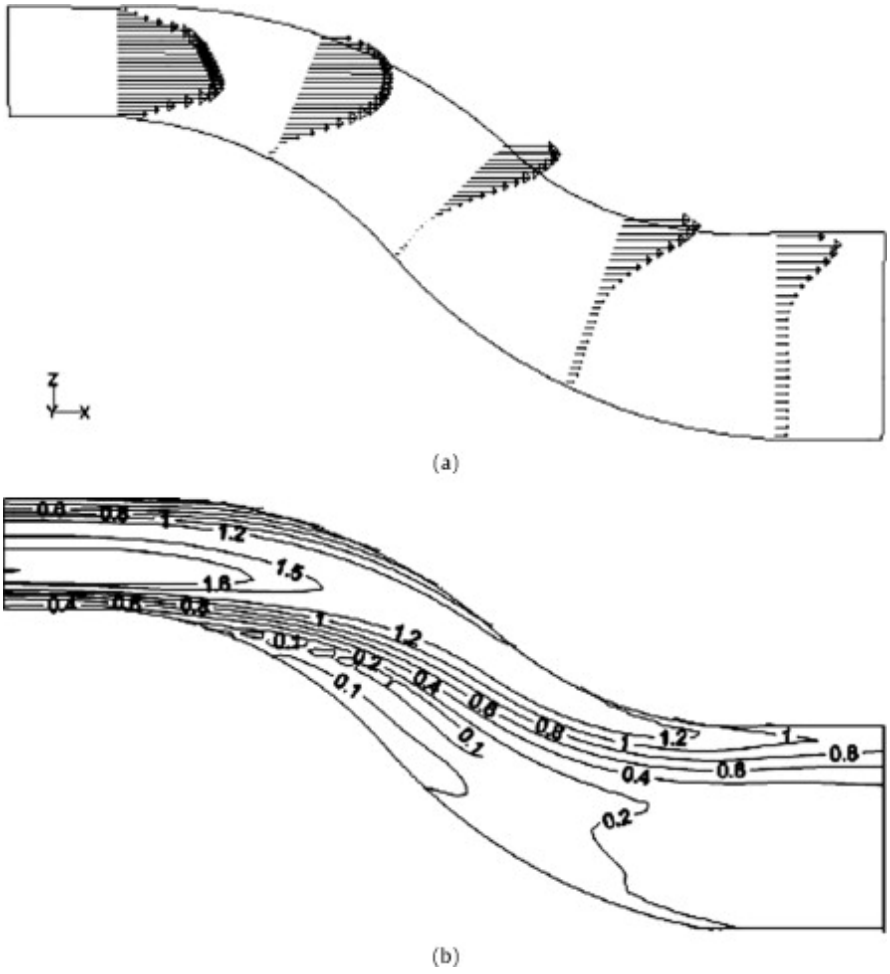

Figure 1.3: Velocity contour and isobars [2]

Figure 1.3a, from Paul *et al.* [2], shows velocity contours in an S-duct diffuser from the inlet on the left, to the exit plane on the right. Evidently the flow becomes distorted as it progresses along the duct and is non-uniform at the exit. Figure 1.3b depicts the same distortion in the pressure contours. Compressor performance is sensitive to inlet conditions, therefore if inlet distortion can be reduced, compressor performance could be improved. If there

is variation in pressure it causes cyclic loading and variation in velocities can cause cyclic stall or surge.

This has been a research focus at the Royal Military College of Canada (RMC) lab since 2015 in both numerical and experimental work. To put the present work in context, Chapter 3 goes through the details of previous work that has been completed at RMC by Asghar *et al.* looking at focus on flow control (FC) in S-ducts. Specifically they explored bio-inspired tubercles to reduce or eliminate the separation regions in S-ducts, described presently. These geometries apply FC in the form of sinusoidal tubercles upstream of the regions of separation in an operationally representative S-duct. This research is continued and expanded upon in the current work.

1.1 Tubercles

Tubercles are bio-inspired from the geometry of the humpback whale. They have been tested in many applications as successful passive flow control devices, usually as leading edge bumps on lifting surfaces. Figure 1.4 shows these undulations on the left pectoral flipper at the bottom of the image. They serve to allow the large mammal to manœuver through the water to chase prey. They help to keep the flow attached when at high angles of attack. This naturally-occurring geometry inspired many important links that will be reviewed in the next chapter. In most experiments, a sinusoidal pattern was chosen to model tubercles. Briefly, Fig. 1.5 shows an example of tubercle implementation on one of the test rigs at RMC. Here, one can see the sinusoidal undulations applied to the leading edge of the airfoil.

Figure 1.4: Humpback whale [3]

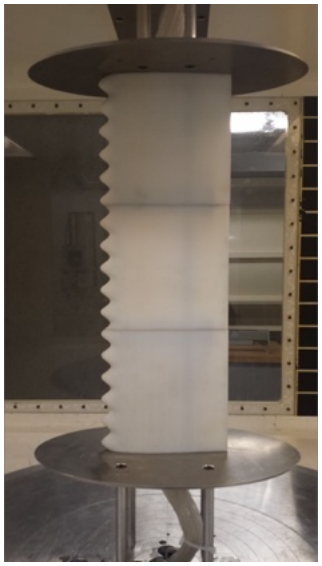

Figure 1.5: Tubercles on a 2D experimental airfoil (leading edge on the left)

When implementing such sinusoidal pattern tubercles, they are commonly sized based on the amplitude, A, and wavelength, λ, both shown in Fig. 1.6 and normalized with respect to the chord of the airfoil.

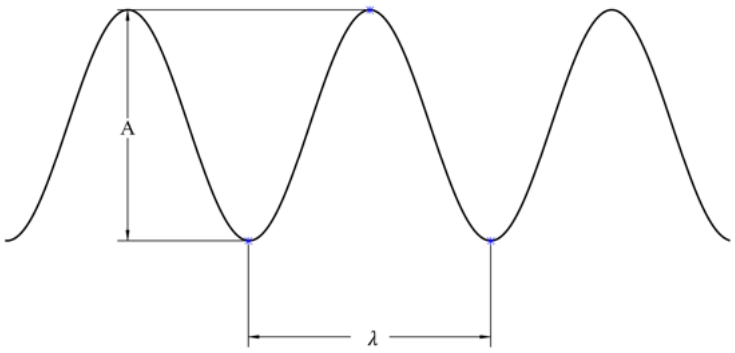

Figure 1.6: Tubercle wavelength and amplitude

In experiments, the tip of the tubercle, the furthest point away from the trailing edge, is known as the peak and half a wavelength away span-wise, is the trough or valley. As air flows across the leading edge of the wing, span-wise flow is induced due to local pressure gradients. The incident flow traveling towards the airfoil stagnates at the peak first, resulting in a locally higher pressure that induces flow towards the lower pressure regions aligned with the troughs, where air has not yet stagnated. This creates local span-wise flows along the leading edge tubercles of the airfoil.

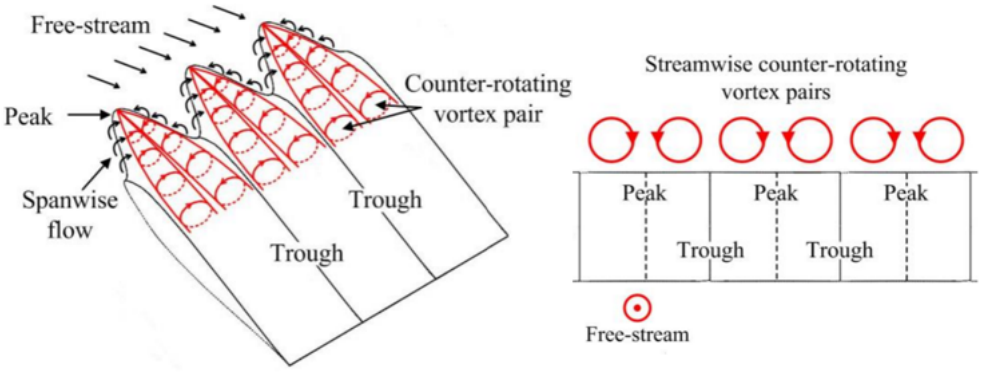

Figure 1.7: Flow around airfoil tubercles [4]

Figure 1.7, on the right, shows stream-wise vortex pairs motivating flow span-wise at the surface from peak regions. Flow in the troughs migrates normal to the surface to satisfy continuity, generating a pair of CRV, then travels towards the peak span location, where the vortices meet and divert normally down towards the airfoil surface. This down-wash entrains higher momentum free-stream fluid into the boundary layer to keep the flow attached in this region. On airfoils, this setup has helped reduce the suddenness of post-stall behaviour, avoiding dramatic lift loss, thereby enhancing the stability of the aircraft. The up-wash sections can create small areas of separated flow on the wing however, since separation does not occur at the same point on the chord for the full span of the airfoil, adding tubercles creates more gentle stall characteristics. And of greater significance, the bulk flow is not separated.

When implementing tubercles on an S-duct, there is no leading edge but there is a suction surface; there are two in fact. Stream-wise undulations are initiated in the vicinity of the adverse pressure gradient. The undulations, like leading edge tubercles, need to protrude into the free stream flow in order to generate periodic span-wise pressure gradients sufficient to produce CRV. Figure 1.8 shows the placement of stream-wise tubercles on the S-duct geometry used in this thesis. Figure 1.9 shows section cuts at both tubercle locations. Note that this is not to scale and is for the explanation purposes only. Section 4.4 expands fully upon the S-duct and tubercle geometry.

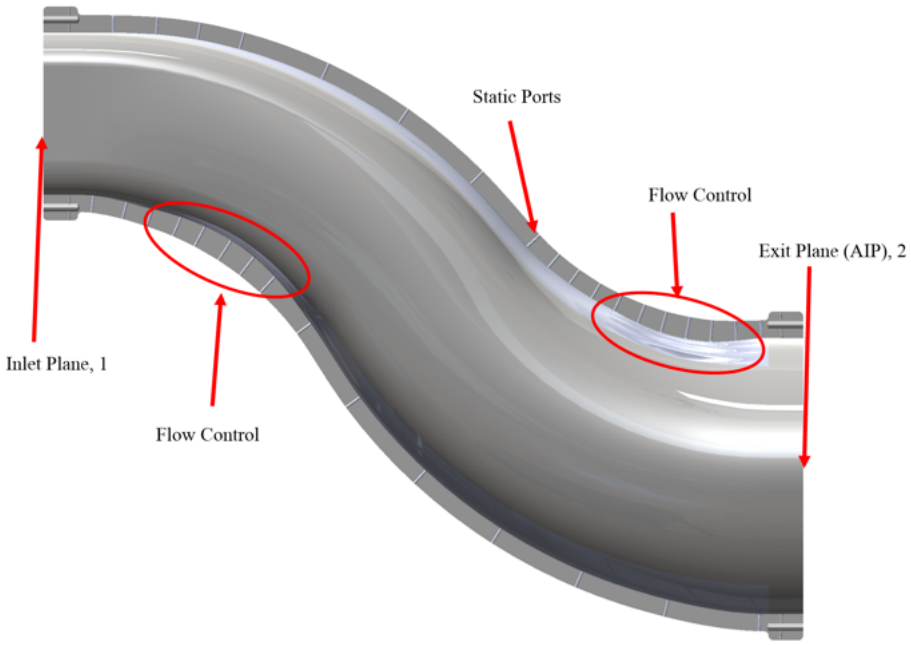

Figure 1.8: S-duct with details showing flow control regions

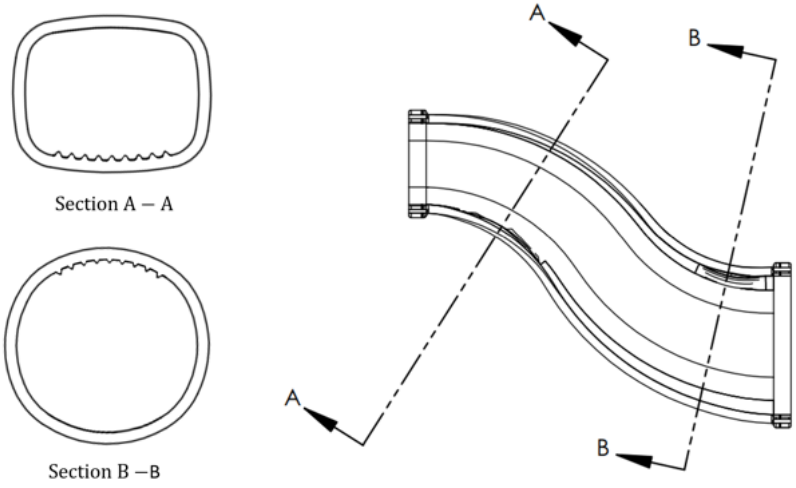

Figure 1.9: S-duct showing stream-wise tubercle cross sections

The previous work by Asghar *et al.* recommended further investigation into tubercle geometries related to their most successful design. This thesis developed a new design to compare to the previous work. This is elaborated in Section 4.2.1.

1.2 Research Motivation

In a high-subsonic flow, S-ducts are used on air vehicles with embedded engines. Based on the previous tests performed by Asghar *et al.*, a passive flow control scheme using stream-wise tubercles was attempted to mitigate separation regions and reduce inlet distortion [20]. Separation still occurred in the S-ducts tested and further improvements were sought by corroborating this with work done by Sidhu *et al.*[21]. Specifically, the tubercle size was reduced to 75% of the original wavelength and amplitude. Smaller tubercles have been shown to work more effectively on airfoils, so this was extrapolated to the S-duct problem. The tubercle size extends outside the boundary layer and is therefore able to initiate counter rotating vortices (CRV) to mix higher momentum free-stream fluid into the boundary layer. The goal is to increase momentum along the wall, instead of simply tripping a laminar boundary layer to turbulent state. While implementing tubercles was designed mainly for airfoils, it was used to assist with developing the new flow control design for the present work. The motivation is to implement new flow control to eliminate all separation in the duct and improve aerodynamic interface plane (AIP) conditions. To improve AIP conditions more uniform total pressure and reduced secondary flows is investigated. These secondary flows have not been measured experimentally and are being investigated in this work at transonic inlet speeds.

1.3 Scope, Research Goal, and Objectives

This thesis work experimentally tested the baseline and two FC S-ducts establishing flow quality coefficients and AIP-relevant information. The scope includes the computational fluid dynamics (CFD) analysis of the baseline duct, and automation of the meshing process for FC S-ducts.

The goal of this thesis is to experimentally investigate improvements that can be made with passive flow control on internal aerodynamics in an S-duct. This work develops an automation program to be implemented towards advanced S-duct design. This can improve the flow quality at the engine face, increasing the stability and performance of gas turbine engines.

This project is structured in phases at two labs: the Royal Military College of Canada (RMC) and Durham University (DU). There is an existing, long standing relation between RMC and DU on S-duct analysis, computationally and experimentally. The project objectives were:

- Design, fabricate and test an baseline and two Flow Control S-ducts experimentally in a transonic wind-tunnel (RMC).
- Numerical modeling of baseline S-duct and compare to experimental work(DU).
- Create automated system to export S-duct flow control mesh, based on user defined tubercle geometry (RMC and DU).

1.4 Thesis Outline

This report begins with discussing relevant theory of general topics and flow control in Chapter 2. This leads into a higher level review of the relevant

literature in the area of study in Chapter 3. It will include, but will not be limited to, the review of S-ducts, flow control, the implementation of internal flow control on S-ducts, and CFD for various applications.

Chapter 4 will present the configuration of the apparatus and instrumentation used in the experimental work. This section will acknowledge an uncertainty analysis that was performed on the experimental results, which is presented in Appendix A. The same configuration for the numerical modeling the baseline duct will then be described in Chapter 5.

The experimental, Chapter 6, and computational, Chapter 7, work will be analyzed and compared. Chapters 8 and 9 will present the concluding remarks and recommendations for future work, respectively.

2 Theory

S-ducts are required in aircraft with embedded engines to supply air flow to the engine face. S-ducts are also used in aircraft for stealth purposes since they conceal the rotating fan blades from search radars. They are used for reducing noise by suppressing pressure waves that propagate away from the engine fan. The development of secondary flow and separation can lead to flow non-uniformity at the exit of the S-duct, which can be mitigated by implementing flow control. The problem, as mentioned in Chapter 1, is having directed airflow entering the compressor unevenly. There is a need to have well designed S-ducts, mitigating or eliminating flow separation. This can be done through implementing flow control. The flow phenomena described here will include flow distortion, separation and passive flow control techniques relevant to this work.

2.1 Distortion

Distortion refers to non-uniformities in the total pressure and hence streamwise velocity present at the AIP, shown in Fig. 2.1.

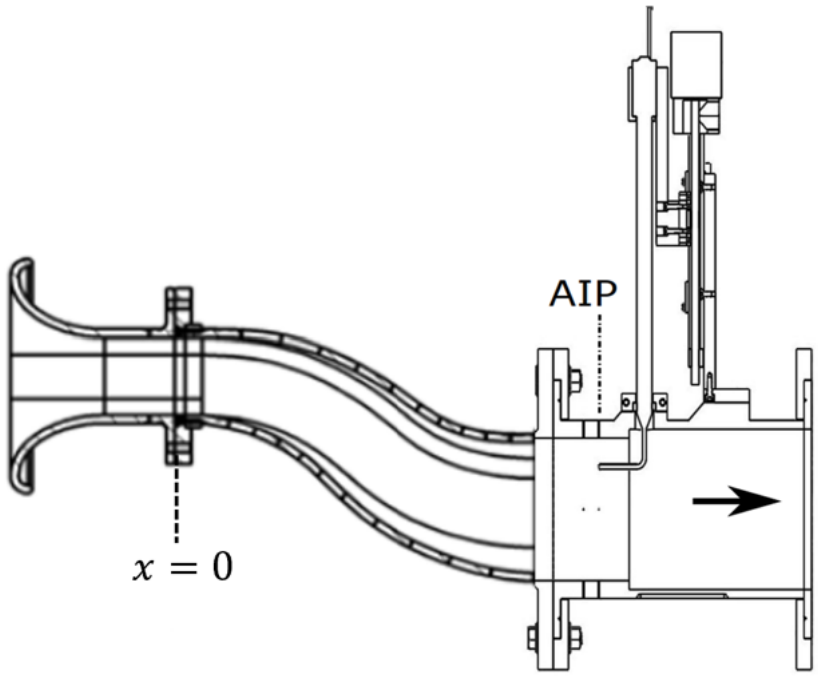

Figure 2.1: AIP location in the instrumentation S-duct, adapted from [5]

This can be a result of the secondary flows or separation. The secondary flow particular to S-duct is characteristic of pipe bends. The secondary flows that occur in pipes is shown in Fig. 2.2 assuming no separation. The flow is initially traveling horizontally from left to right and as it begins to navigate the elbow, the direction of the velocity, or momentum, of the flow must adjust to follow the pipe. Assuming this is fully-developed flow, the highest momentum flow is near the centre-line of the pipe. Since this flow needs to be redirected to follow the curvature, the high momentum flow approaches the outer radius. The fluid cannot travel through the wall, therefore it needs to be redirected and recirculates through the lower momentum regions along the walls. Figure 2.2, cut section A-A, shows the re-circulation region as seen at the exit of this

pipe. These two CRV are referred to as Dean vortices and the general flow phenomenon is called Dean flow [22].

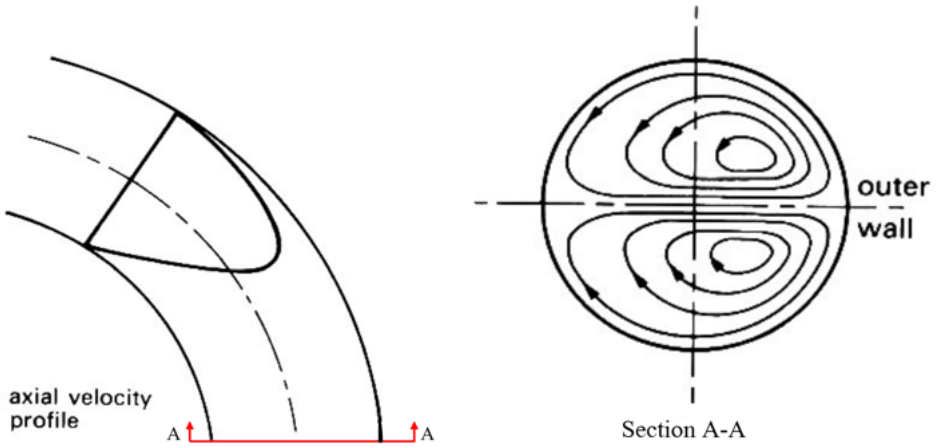

Figure 2.2: Dean vortex, adapted from [6]

Dean vortices are predominantly seen in pipe flow. Two similar secondary flow phenomena seen on concave and convex surfaces are the Görtler and Taylor vortices, respectively. A Görtler vortex is a boundary layer instability that develops as CRV in the boundary layer of laminar or turbulent flow, depicted in Fig 2.3 from Saric [7]. In some cases, these can cause a boundary layer transition from laminar to turbulent sooner than it otherwise might. These vortices form over concave surfaces such as the pressure surface of turbine or compressor blades. They grow slowly and stay within the boundary layer.

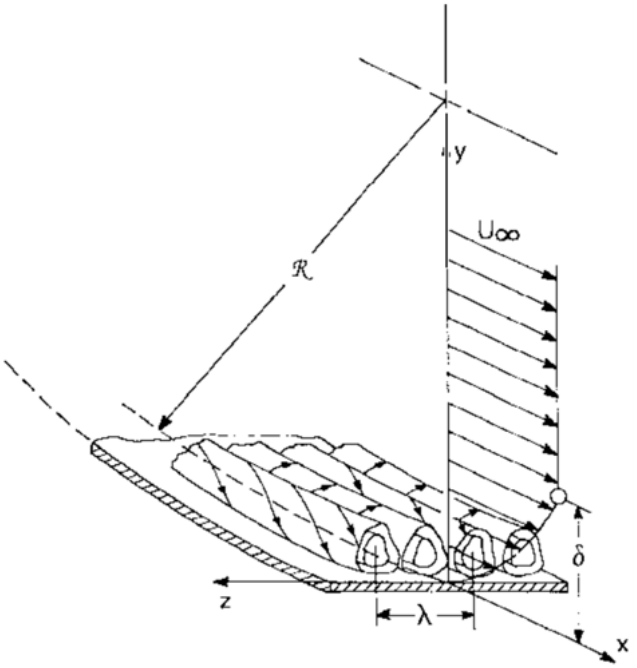

Figure 2.3: Görtler vortex [7]

Figure 2.4 shows concentric cylinders. Here the outer cylindrical casing is stationary and a inner cylinder is rotating producing a Taylor vortex. Taylor vortices can be confused with Dean vortices since both occur in the streamwise direction and are not limited to the confines of the boundary layer. The difference between the two is that Taylor vortices form in closed systems as shown in Fig. 2.4 [8]. Whereas in Fig. 2.2, the Dean vortex is a pair of CRV that forms in an open system. An S-duct is considered an open system since there is an open inlet and exit.

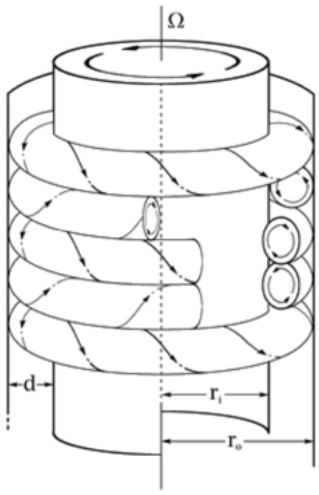

Figure 2.4: Taylor vortex [8]

Since the S-duct, which is the geometry being explored in this work, is also diffusing air, an adverse pressure gradient develops leading to boundary layer growth. The accumulation of low momentum flow along the duct walls allows secondary flows to develop faster within the duct making flow separation more likely, deteriorating flow quality, and increasing distortion before the flow reaches the AIP.

2.2 Separation

In the most fundamental condition, as fully-developed flow in a pipe travels around a bend, it can develop a region of flow separation. Separation is dependent on the radius and angle of the bend, as well as the Reynolds number of the flow with respect to pipe diameter. If separation occurs the region can have variations in length and size. Figure 2.5, from Bailes, shows the flow in two pipes entering at the left face and traveling around corners of two different

radii: a sharp 90° elbow (A) and a round 90° elbow (B) [9].

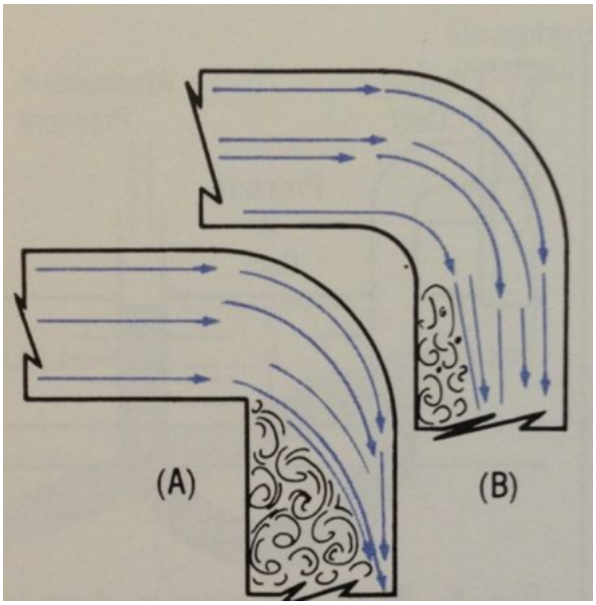

Figure 2.5: Separation in an elbow [9]

The flow must accelerate, then decelerate as it navigates any corner. In the deceleration period, similar to flow decelerating in a diffuser, an adverse pressure gradient forms. In Fig. 2.5 (A) the corner radius is infinitely small, therefore the adverse pressure gradient is infinitely great and the flow readily separates at the bend. In Fig. 2.5 (B) however, the flow has a larger inner radius to follow and is able to stay attached over a longer distance. Nevertheless, the adverse pressure gradient associated with the flow deceleration is still excessive and the flow detaches just downstream of the bend in this schematic. If the inner radius is increased, the separation region might be avoided entirely. However, in increasing a bend radius, the overall stream-wise length of an elbow must increase to allow the pipe to still turn the flow by 90°. In an S-duct, where there are two bends, the stream-wise length increase would

be doubled. In aircraft design, a major goal is to reduce overall weight of the inlet, making longer ducts undesirable. This classic design compromise is why some separation and inlet distortion is tolerated. If this distortion can be reduced, then the length and bend radii of the an S-duct inlet could be decreased, reducing overall nacelle and inlet weight.

The problem of separation in S-ducts is exacerbated by secondary flows that develop in the S-duct bends, similar to pipe flow. While distortion causes the conditions at the AIP to be non-uniform, separation creates areas of re-circulation that dissipate energy. This lost energy can not be converted to total pressure at the AIP and is therefore of greater concern than distortion. An S-duct can operate more efficiently if separation is reduced, and some distortion can be tolerated at the AIP.

2.3 Flow Control

The two broad classes of flow control are active and passive. Active flow control can be implemented through plasma, blowing or suction for instance. Active flow control in the form of suction or blowing jets is depicted in Fig. 2.6, from Harouni [10]. The suction section removes the lower part of the boundary layer, containing low momentum fluid. The blowing section introduces more momentum through jets of high velocity air. This and other types of active flow control demand some form of energy input to function. The focus of the present study is on passive flow control, which will be discussed in more detail. Active flow control requires energy to run. However in aircraft applications, it is preferable to have more power directed towards propulsion, making passive flow control more appealing.

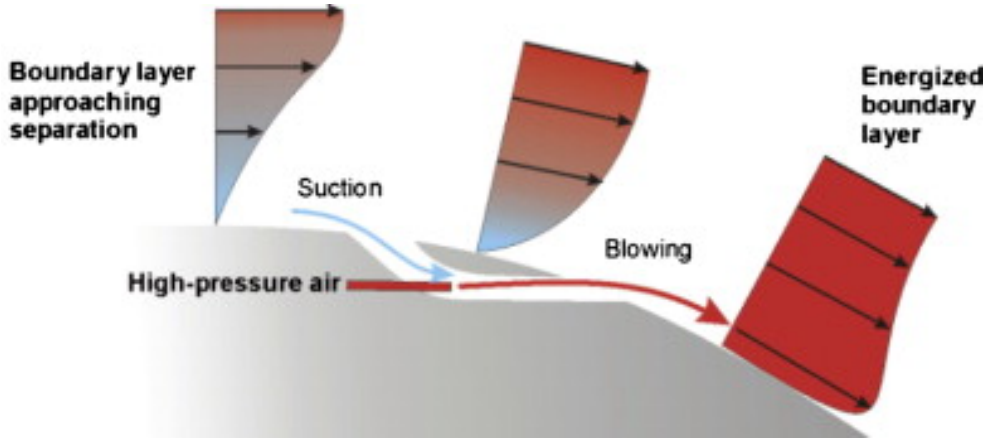

Figure 2.6: Sucking and blowing active flow control [10]

Passive flow control is implemented through bumps, grooves, ridges, vortex generators (VG) and tubercles among others, and require no external energy source to function. VG and tubercles are both fashioned into a surface to remove or mitigate separation. VG are used heavily on aircraft wings since they are easy to install and repair. Tubercles require more manufacturing into the structure of the aircraft and are less well known, therefore used less frequently. They both operate outside the boundary layer and their aim is not primarily to trip the boundary layer to become turbulent but to mix higher momentum flow further from the surface with lower momentum boundary layer flow. The key difference between tubercles and VG are the method by which the induced CRV are formed. Figure 2.7 shows streamlines traveling over a flat plate with VG, from Martinez [11]. CRV are driven by forced separation behind a VG vane, depicted in Fig. 2.8, where the red shaded area is the region of separation. The flow is traveling from left to right and separates at the lip of the vane, shown in the blue arrows.

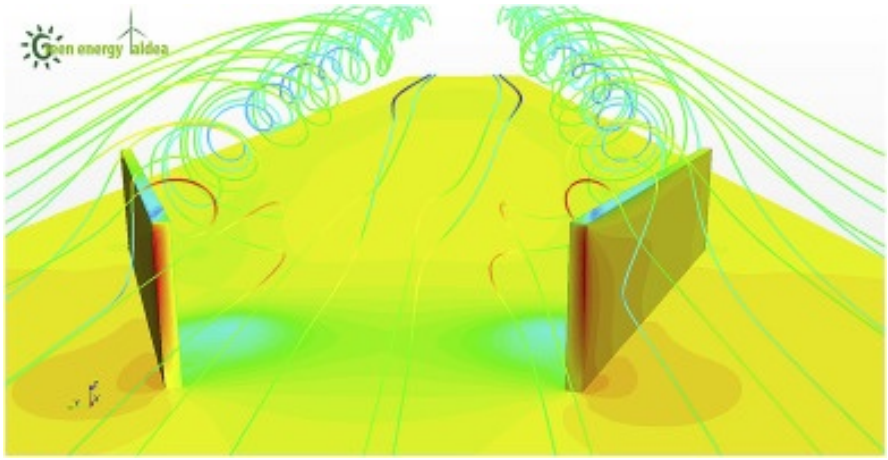

Figure 2.7: Vortex generator CFD flow of streamlines [11]

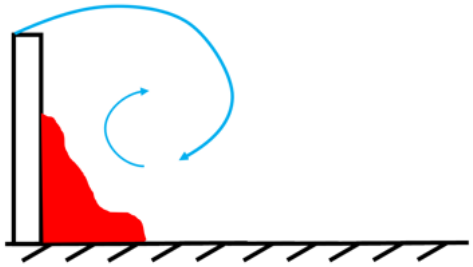

Figure 2.8: Singular VG vane depiction of separating flow

The separation region behind the VG vane leads to recirculating flow. The rotational flow travels downstream of a VG in the form of a stream-wise vortex. Since the VG vanes protrude outside the boundary layer, the CRV mix the high momentum free-stream flow with the low momentum boundary layer flow. This increases the momentum along the surface, of an airfoil, helping the flow to remain attached when it might otherwise separate.

2.4 Tubercles

Tubercles, initially described in Section 1.1, are included here to distinguish from VG. Compared to VG, tubercles behave similarly in that they generate stream-wise pairs of CRV. However the method of forming the CRV's is different. Figure 2.9 shows the cross-flow streamlines at a plan normal to the suction surface of an airfoil [12].

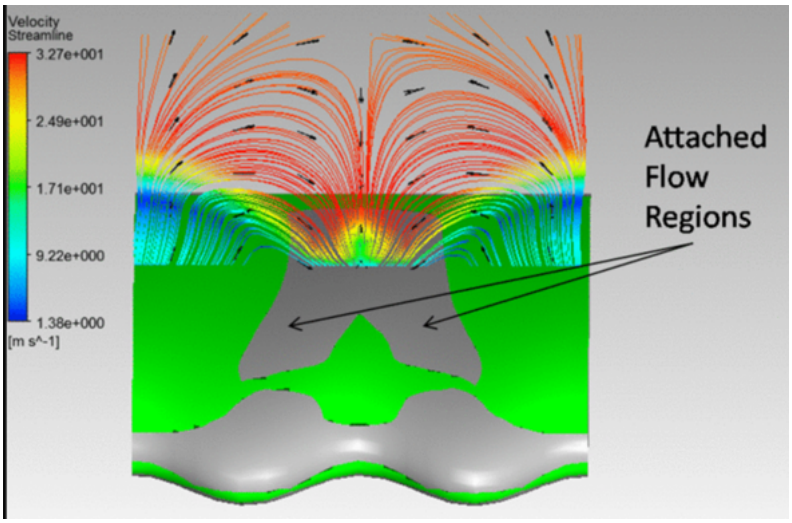

Figure 2.9: CFD showing two CRV on the surface of a tubercled airfoil [12]

The formation of CRV travel along the surface of the airfoil in the free-stream direction. This phenomenon is driven by a pressure gradient as opposed to forced separation from a VG. Delta wings behave in a similar fashion, shown in Fig. 2.10 [13].

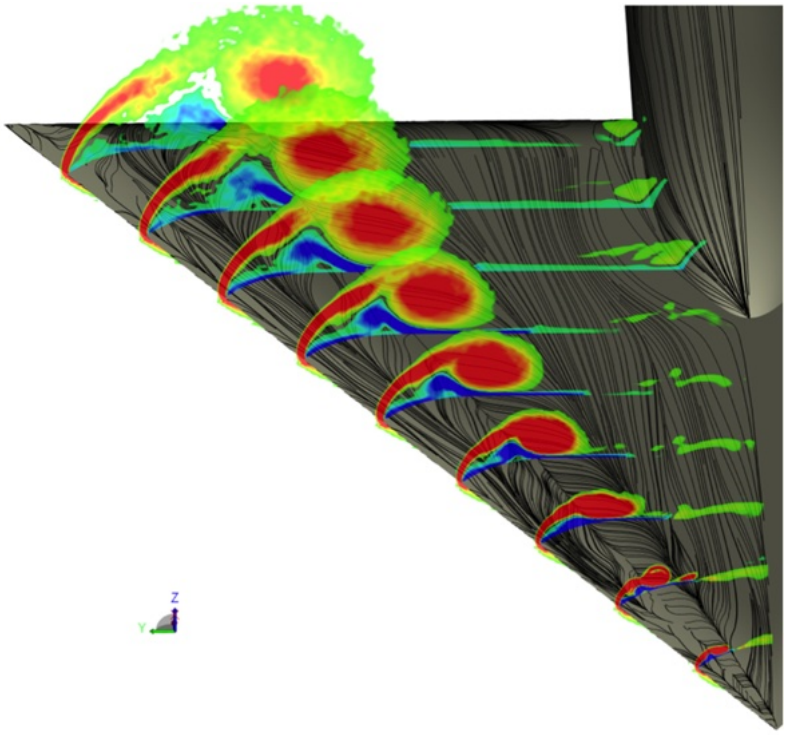

Figure 2.10: Delta wing formation of a leading edge vortex [13]

At high angles of attack, the low pressure region on the top of a delta airfoil causes flow from the higher pressure region below the airfoil. This generates a vortex which is driven by a pressure gradient. In fact, in previous work, by Bolzon *et al.* [23] and Wei *et al.* [4], tubercles have been described as small delta wings in their behaviour. The implementation of passive and active flow control on various suction surfaces has been investigated in previous research, discussed in Chapter 3.

3 Literature Review

S-duct intakes and their internal aerodynamics have been thoroughly investigated since they are integral to many propulsion designs. A comprehensive study was performed on previous research pertaining to the scope of this work. Topics include: integrated propulsion; flow control, with focus on passive techniques; S-ducts experimental and numerical work; and their numerical modeling. At the outset, it is critical to understand S-ducts and their application in aircraft, why they are needed and what compromises are made in the design.

3.1 Integrated Propulsion Systems

Propulsion systems in aircraft aim to have the engine operate at a high efficiency, free of instabilities. Engine stability and efficiency are related directly to the total pressure profile at the engine inlet. Instabilities in the engine can lead to surge or stall, mechanical stress, and low and high cycle fatigue. For externally-mounted propulsion systems oncoming air hits the engine inlet with a uniform velocity, typically via a pitot style inlet, the ideal configuration.

The flow into externally-mounted propulsion systems can be affected by angles of attack, yaw, shock-boundary layer interactions, and any protuberances such as landing gear, ancillary near the inlet, or equipment on the external

surface of the aircraft as described by Steenken [24]. Integrated propulsion systems on the other hand, have inherent efficiency challenges due to boundary layer ingestion (BLI) and inevitable distortion in engine inlet conditions imparted to the flow by ducting. The ducting to the engine inlet, the compressor or fan face, can significantly reduce engine efficiency if the flow is distorted, as noted by Brear *et al.* [14] and Harouni *et al.* [10]. To mitigate distortion or eliminate separation, flow control can be added to the inner surface of the S-duct, as discussed in Section 2.3. Brear *et al.* investigated a top-mounted S-duct that would have to overcome a greater degree of BLI, increasing the presence of low momentum flow in the duct. They measured pressure at the AIP and performed flow visualization using oil and dye flow. Their experimentation showed that adding a bell-mouth inlet improved pressure recovery by 2%, this may not be realistic for aircraft, however it is adopted for experimentation. Brear and his team noted that separation was contributing to the unsteady conditions at the AIP. They hypothesized a weak pair of CRV that start at the inner radii, present on the surface of the duct as presented in Fig. 3.1 [14]. These CRV, were also noted by many others a there that will prevail in this Chapter.

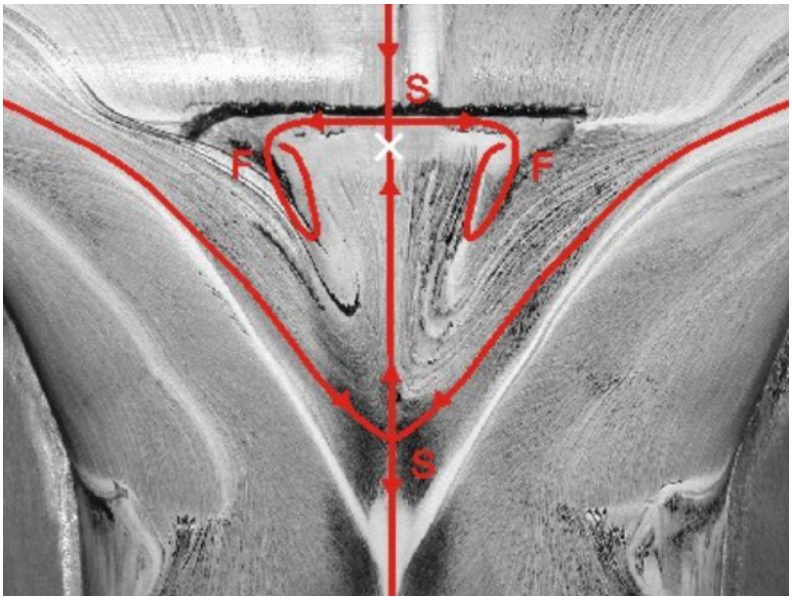

Figure 3.1: S-duct surface flow visualization in a region of reversing flow after an inner radius [14]

Separation, similar to CRV, is often a feature of inner radius bends. To aid in reducing the losses from separation, flow control can be added. This has been studied in depth by other researchers as well, and is reviewed in current work.

3.2 Flow-Control

The goal of flow control is to improve flow along a surface to eliminate or at least decrease the extent of separated regions. Implementing flow control seeks to increase the momentum of the boundary layer at its lowest levels, either by injecting momentum in the form of high velocity jets or mixing the higher momentum free-stream flow with the lower momentum boundary layer flow. This can be achieved with active or passive systems, as describes in

Chapter 2. This research is focused on a passive techniques, so the literature pertaining to such methods is described next.

The Reynolds numbers discussed in this chapter are non-dimensionalized with respect to length (L), diameter (D) or chord (c). Length is used in Reynolds number calculation for flat plates. The AIP diameter is used for duct Reynolds calculation and chord is used for airfoils. Reynolds numbers are presented for comparison and their characteristic lengths are noted

3.2.1 Vortex Generators

A common method of passive flow control is the use of VG. In 2001 Jenkins *et al.* saw the similarity of separation on airfoils and S-Duct intakes and implemented VG on S-ducts to reduce or mitigate the separated flow [25]. They found that micro-VG were effective at re-energizing the boundary layer flow in adverse pressure gradient situations.

Chronologically then, Allan *et al.* studied the performance of adding VG to flat plates, seeking to investigate the momentum near the boundary layer at $Re_L = 7.6 \times 10^6$ [26]. In 2002, Allan and his team compared the effects of VG vanes and active flow control of jets on flat plates to a numerical study, to evaluate if a CFD solver could accurately predict the effects of this flow control methods. They found the Shear Stress Transport (SST) turbulence model best matched the experimental results of their active and passive flow control techniques. They also looked into modifying the VG shape from a trapezoidal vane to a rectangular one and found that they both produced stream-wise CRV of equivalent strength.

This work was continued in 2011 by Parham *et al.* who implemented VG on an S-duct at an inlet Mach number of 0.85, and $Re_D = 4.94 \times 10^6$ [27].

Parham and his team described the VG as overcompensating the S-duct bends. The fence style VG decreased distortion, at the cost of total pressure loss. However, the fence and fin style VG increased distortion and total pressure loss. This proved that there is an optimal implementation of VG that needed to be further investigated. This was extrapolated on by Vaccaro *et al.* in 2015 through the implementation of active flow control in an S-duct at $Re_D = 1.77 \times 10^6$ [28]. They noted that the active flow control was able to improve total pressure ratio at the AIP. Another important conclusion of their work was that implementing non-intrusive static pressure measurements on the surface of the S-duct enabled the detection of flow separation. The phenomenon was visualized by Tanguy *et al.* in 2017 using Particle Image Velocimitry (PIV), at an inlet Mach number of 0.27 [15]. While VG showed some improvement in mitigating the separated flow, they can also cause regions of separated flow directly downstream. Figure 3.2 shows the swirl measured using PIV for multiple VG configurations.

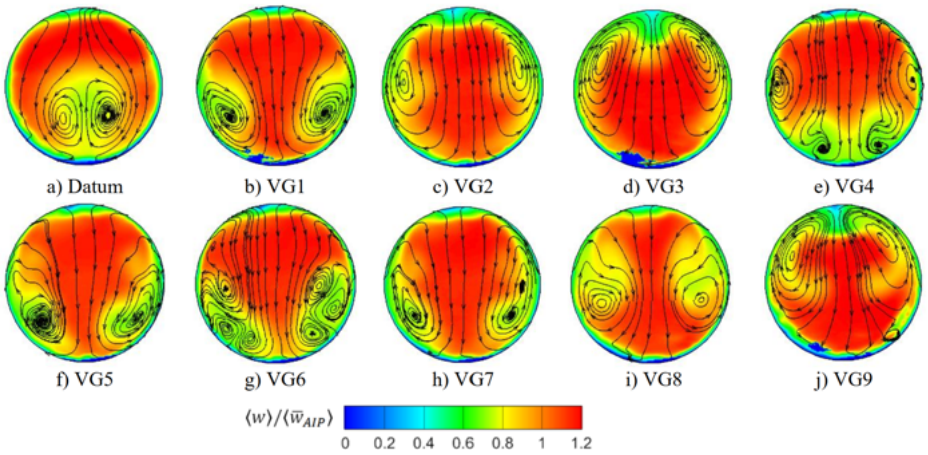

Figure 3.2: Non-dimensional time-averaged out-of-plane velocity with in-plane stream-lines at the AIP depicting the location and number of CRV, from [15]

In Figure 3.2 there is one pair of CRV at the lower half of figure (a), located at the AIP downstream the first bend. With different VG configurations the CRV have increased in number, as in e) and g). There are also configurations where they decrease in intensity and size, for example c) and d). Tanguy *et al.* proved that there are benefits to adding passive flow control in S-ducts, however it must be implemented in a way that is also reducing the distortion at the AIP.

3.2.2 Serrations and Tubercles

The literature on tubercles and serrations includes tests and simulations at a range of Reynolds numbers. Including representation from across the Reynolds spectrum was intentional due to the the difference in non-dimensional length, chord for an airfoil and diameter for a duct.

In 1972 Soderman experimented with passive flow control on a NACA $66_4 - 012$ airfoil [29]. The experimental work was at a Mach number of 0.13, and $Re_c = 2.32 \times 10^6$ with leading edge serrations on the airfoil. Soderman modified the placement and size of the leading edge serrations, implemented using a cut sheet of metal protruding from the leading edge. Behind the tangentially mounted serrations, there was a cavity which caused flow to separate before reattaching to the airfoil. He found that smaller serrations increased the magnitude and angle of attack of maximum lift for an airfoil, while drag decreased at higher angles of attack. However, if the serrations are too small the effect is more like sandpaper, simply tripping a laminar boundary layer into a turbulent state. The serrations were faired at the tips and roots, similar to a sinusoidal shape. This also increased the maximum lift, although not as drastically as jagged serrations did. Soderman hypothesized that this could

be attributed to the jagged serrations creating more intense vortices. Soderman also considered the placement of the serrations and found it had a large impact on their effectiveness.

In 2001, Watts and Fish noted that the leading edge of the humpback whale's pectoral flipper has undulations which aided the large mammal to manœuver and chase prey [30]. The undulations were defined as tubercles, and Watts and Fish then applied a sinusoidal tubercle profile to the leading edge of a NACA $63_4 - 021$ airfoil operating at $Re_c = 1.19 \times 10^4$. The aim was to test the benefits of tubercles for manœverability in airfoils and they noted an increase in lift and reduction of induced drag.

In 2007, Johari *et al.* applied tubercles to the leading edges of the same profile at $Re_c = 1.83 \times 10^6$ [31]. They noted, through visualizing the flow, that it separated non-uniformly, primarily at the tubercle valleys. Work was continued with tubercles on this profile at $Re_c = 1.83 \times 10^5$ by Custodio in 2007 [32]. He visualized the flow by applying tufts to the airfoils. Spanwise flow and delayed regions of separation on the tubercled airfoils were noted, compared to the baseline. In 2011, Hansen *et al.* visualized the flow on the same profile using PIV at $Re_c = 2.23 \times 10^3$ [33]. Through this visualization they were able to note the pair of CRV that form off a tubercle, noting that the circulation decreased with distance down the airfoil as energy dissipated and CRV's influence neighbouring vortices. The NACA $63_4 - 021$ airfoil at $Re_c = 1.8 \times 10^5$ to $Re_c = 3.0 \times 10^5$ was used again in 2012 by Dropkin *et al.*, this time in a computational study [16]. The authors numerically modeled a tubercle wavelength of 50%, and amplitude 12% normalized with respect to the mean chord length [16]. Using *ANSYS Fluent* as their solver, they were able to show the vortices that develop, shown in Fig. 3.3. The vortex pair at each tubercle appeared to help to keep the flow attached in span-wise sections

of the airfoil. Dropkin and his team noticed that through adding tubercles, a cyclic span-wise pressure, and therefore velocity, distribution was generated.

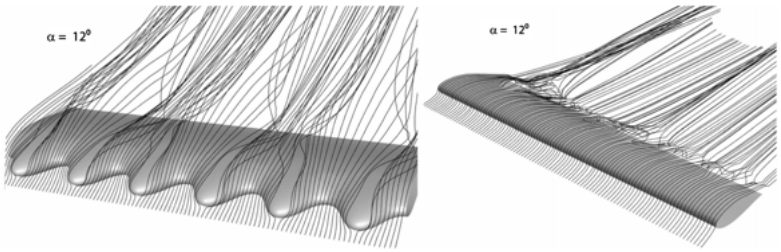

Figure 3.3: Flow separating over a NACA 63_4-021 airfoil, adapted from [16]

In 2014, Asghar *et al.* performed experimental work on low pressure turbine (LPT) blades with leading edge tubercles at $Re_{c_{axial}} = 5.5 \times 10^4$ [34]. This work was continued in 2019 by the same team using hot wire analysis [35]. The chosen airfoil has a known location of separated flow from previously recorded data. At the separation angle of attack, a laminar separation bubble tends to form and can reattach under some conditions. The airfoil was tested between Reynolds numbers of 1.5×10^4 and 6.0×10^4. Asghar and his team found that the smallest studied tubercle size had a noticeable positive impact on the performance of the airfoil near stall conditions.

Bolzon *et al.* focused on tubercle application to wind turbines in 2015 and the variation between flow control methods [23]. They noted that tubercles act similarly to VG by increasing the momentum in the boundary layer. They acknowledged that this has been previously done in delta wings, where a single pair of stream-wise CRV occur, providing only regions of down-wash on the wing. The effects of tubercles are much smaller and create compartments of flow behind a pair of tubercles. This creates isolated regions of attached flow, such that if one region stalls, adjacent regions may not and continue to

produce lift. Figure 3.3 on the left shows this compartmentalization, which is attributed to rendering stall more gradual for airfoils. Compartmentalization was initially noted in 2016 by Bolzon *et al.* [36]. In similar applications, tubercles have also been implemented on a horizontal axis wind turbine, performed experimentally and numerically in 2015 by Ibrahim *et al.* [37]. They noted an increase in power produced for severe wind conditions. Other applications of tubercles include tidal turbines to reduce cut-in speed and improve starting performance, Shi *et al.* 2016 [38, 39].

Wei *et al.* noted that in 2015 based on experiments using a NACA 63_4-021 airfoil at low Reynolds numbers ($Re_c = 2.74 \times 10^5$), that the area behind the tubercles remained attached in the post-stall regime [4]. Their conclusions matched those in the previous work by Dropkin *et al.*, and others [16].

Bolzon *et al.* continued the work in 2016 on the leading edge of a NACA 0012 airfoil [36]. Bolzon and his team and Serson *et al.* [40], in 2017, performed computational studies on the NACA 0012 airfoil at $Re_c = 1.2 \times 10^5$ and $1 \times 10^3 \geq Re_c \geq 5 \times 10^4$, respectively. Bolzon *et al.* saw the similarities between tubercle CRV and wing tip vortices. Serson and his team found experimentally that there was non-uniform flow over the tubercled airfoil which gave the wing higher lift coefficients in some span portions. Bolzon and his team then went on to implement a single tubercle on the tip on a swept NACA 0021 airfoil at $Re_c = 2.25 \times 10^5$ [41]. Addition of a tubercle increased the wingtip vortex strength, although it was dependent on whether it started at a peak or valley, which had opposite effects.

The demonstrated successful applications of tubercles on lifting surfaces led in 2018 to the idea of their implementation to internal aerodynamics. Asghar *et al.* [20] and Hickling [42] both looked at the comparison in three S-duct tubercle designs tested at Mach 0.8. Asghar and his team focused on

the experimental work and compared it to the computational work done by Hickling. In 2019, Hickling and Ingram [43], and Schneider [44] looked into various computational studies of S-duct flow control, this will be discussed further in the literary review of computational research. Rider *et al.* in 2020 discussed new experimental AIP data for one passive flow control S-duct and compared them to the previous computational work by Hickling [5].

Extrapolating from this research, in 2020, Sidhu *et al.* built a neural network to correlate tubercle size and Reynolds number with performance [21]. They found that a low-amplitude, low-wavelength tubercle (as normalized with chord) delivered the best results by improving post-stall performance and increasing maximum lift. They recommended that more experiments be conducted on smaller tubercle geometries.

3.3 S-Duct and Diffuser Work

This section will chronologically review the S-duct experimental work with Section 3.3.1 discussing the S-duct research performed previously at RMC. In 1983, Vakili *et al.* explored the secondary flows generated in compressible flow in S-ducts at $Re_D = 3.25 \times 10^8$ [45]. They concluded that at Mach 0.6, with the S-duct design they chose, the presence of secondary flow could be discerned at the AIP. This experiment work was continued in 1984 by Taylor *et al.* at $7.9 \times 10^2 \leq Re_D \leq 4.8 \times 10^4$ [46]. Through PIV, Taylor *et al.* were able to conclude that the pressure gradients driving secondary flows were exacerbated when a larger boundary layer was ingested. They noted no evidence of flow separation at these conditions, however as technology has progressed, the Reynolds numbers in S-duct intakes has increased significantly, leading to separation and subsequent blockage, which is a new challenge to

overcome for integrated propulsion.

Vakili *et al.* in 1984 performed experiments with a $30° - 30°$ S-duct, indicating the deflection of the two bends, and it did not have separated flow as noted in the surface oil flow pattern [47]. The Reynolds number and geometry are integral to the design of S-duct AIP conditions. This work was validated by Welborn *et al.* later on using a similar S-duct design [48]. In aerodynamic application the S-duct is shortened, increasing the angle of bends, causing the flow to separate as a compromise for reduced size and therefore weight.

Whitelaw and Yu [49], and Harloff *et al.* continued S-duct research with surface pressure and total pressure at the AIP [50, 51]. Welborn *et al.* [48] corroborated the findings separately from Whitelaw and Yu that discerned that there were strong pressure driven secondary flows that produced CRV. The CRV degraded the uniformity and magnitude of the total pressure at the AIP. Harloff *et al.* focused getting good agreement between numerical and experimental work, also noting the CRV present in the S-duct. In 1992, Anderson began work on VG in S-ducts at $1.158 \times 10^6 \leq Re_D \leq 1.848 \times 10^6$ to reduce the distortion at the AIP and increase total pressure ratio [52]. They mostly focused on numerical work but noted that the scaling of VG height needs to be further investigated.

Whitelaw and Yu continued S-duct work in 1993, with a focus on numerical and experimental work examining the effects of different turbulence models on flow prediction at the AIP [53]. Through experimental work, Whitelaw and Yu confirmed their theory of separation regions and CRV using laser flow visualization. They noted a larger BLI caused the separated region to be larger in size. Anderson *et al.* computationally modeled BLI S-ducts over a range of Mach numbers up to 0.8 [54]. BLI S-ducts experience a greater degree of separation due to an excess in low-momentum flow from the ingested boundary

layer, which developed over the upstream fuselage of the aircraft. In some cases, the S-duct is offset from the surface to stop the boundary layer from entering the duct. In the current project, BLI was not investigated, although it is noted that the flow in BLI S-ducts usually obtain worse distortion and total pressure ratio at the AIP compared to those without BLI.

In 1999, numerical work continued by Benhamaza and his team focused on building flow quality coefficients and the characteristics needed to qualify S-duct improvement at the AIP [55]. This work was used by Bouldin and Sheoran in 2002, and standardized by the Society of Automotive Engineering (SAE) [56]. Flow quality coefficients will be described in detail in Section 4.4. Much later, in 2010, Bissinger and Breuer developed the theory to determine flow quality metrics at the AIP for swirl [57]. This was a critical step to be able to non-dimensionally compare results from different studies.

Anabtawi and their team numerically and experimentally examined the effects of VG at an S-duct inlet Mach number of 0.85 [58]. In 1999, they reported an increase in total pressure ratio. In fact, very few studies have been performed investigating the flow through an S-duct at high subsonic Mach numbers. In 2000, Hamstra *et al.* began work on active flow control in the form of jets on S-ducts at $Re_D = 3 \times 10^6$ [59]. Hastra and his team were able to implement VG and microjets to increase pressure recovery and decrease distortion. The active flow control significantly improved performance over the baseline but required power to operate.

Conditions at the AIP are a function of S-duct geometry, flow and environmental conditions and location of the inlet. The inlet location drives how the flow enters the inlet, if it is ingesting significant boundary layer from the fuselage or if the majority of the boundary layer is diverted. Kohama looked into the environmental conditions and location of S-duct with respect

to aircraft fuselage since it held promise to improve aircraft stealth [60]. The experiment focused on 3-Dimensional (3D) boundary layer effects of flow over a yawed cylinder. It was determined that greater amounts of low-momentum flow created unstable conditions and the generation of the vortices were leading to separation of the duct flow. In 2003, experimental work was performed by Leuers [61], and Rabe both using active flow control jets [18]; and Tournier and Paduano looking at VG and jets [62, 63]. They all noted distortion at the AIP that was subsequently decreased when adding either passive and active flow control.

The experiments discussed to this point acknowledged the hypothesis that an S-duct generated secondary flows in the form of two CRV pairs downstream of the inner bends, that persisted to the AIP. This hypothesis proposes that an S-duct is similar to flow through a pipe where CRV are found downstream of any bend or elbow. Rowe's work in 1970 revealed the presence of these CRV, shown in Fig. 3.4 [17].

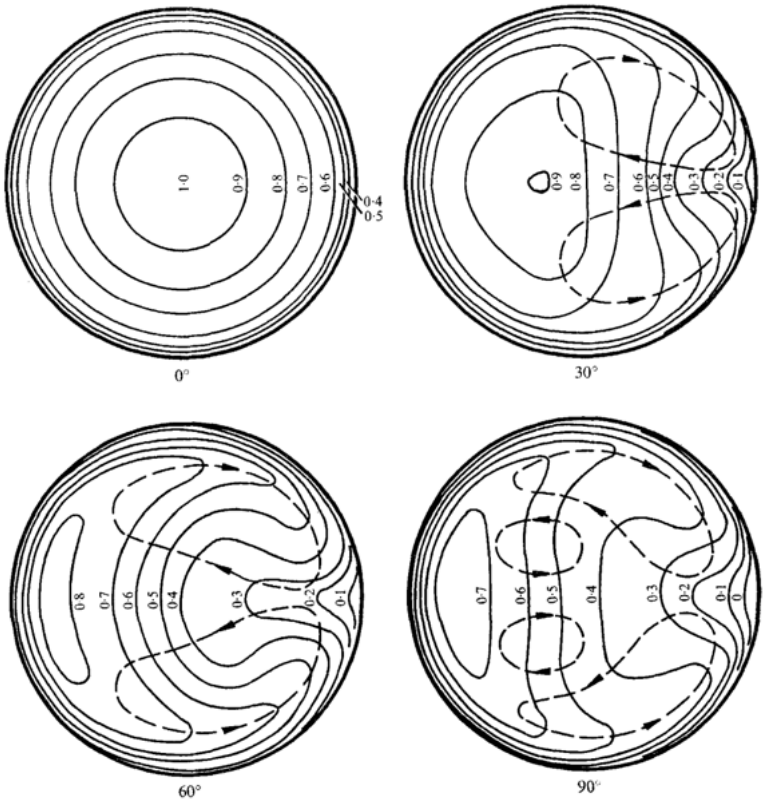

Figure 3.4: AIP showing the CRV for varying degrees of pipe bend [17]

The presence of CRV pairs were similarly found in computational work by Nguyen in 2013 when modeling an S-duct at an inlet Mach number of 0.6 [64]. Nguyen noted that a CRV pair appeared along the surface at the first bend of the duct. A depiction of the CRV is shown in Fig. 3.5, modified from [18]. The air is entering the duct at the left, and secondary flows start developing downstream of the first inner radius, annotated in Fig. 3.5. Then, another set of CRV develop after the second inner radius. As the vortices travel axially, they expand in diameter while dissipating energy. The second-bend CRV are smaller at the AIP since they develop over a shorter stream-wise distance.

The vortices generated at the first-bend reduce the amount of axial flow in the lower region of the duct shown here. Therefore there is a tendency by the separated flow to cause the bulk of the flow to deviate slightly, radially inwards, as the second bend's secondary flows develop further. This hypothesis shows two sets of CRV that develop upstream of the AIP, emanating from the second and first bend inner radii respectively.

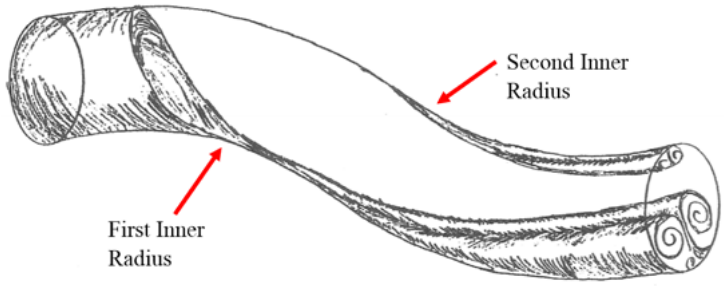

Figure 3.5: S-duct secondary flow, adapted from [18]

The CRV were hypothesized to originate from a separation region in the duct downstream of the inner radius bends. Adding passive or active flow control has been shown to mitigate and sometimes eliminate separated regions.

Gorton *et al.* [65] and Berrier *et al.* [66, 67] in 2004 and 2005 respectively, continued work with BLI S-ducts. Gorton and her team implemented active flow control at $Re_D = 5.3 \times 10^5$. They noted that the active flow control in pulses can reduce total pressure distortion from 29% to 5%. Berrier *et al.* investigated a range of inlet Mach numbers from 0.25 to 0.83 and a range of boundary layer size. They noted that allowing the S-ducts to ingest boundary layer fluid can reduce the size, and therefore weight, of the inlet [66]. The S-duct can be smaller when the offset between inlet and AIP is decreased, and when the inlet is mounted closer to the surface of the aircraft

a larger boundary layer is ingested. Their analysis of experimental and computational work showed that the non-uniform flow of ingested boundary layer leads to increasing chances of separation. Their experiments on four different Boeing-unique designs considered Mach numbers in the range of 0.1 to 0.9, and boundary layer thicknesses of 25% to 30% of the inlet height, for the rectangular S-duct. This is significant as it is some of the only work done at transonic Mach numbers. Their computational studies demonstrated that the performance of the inlet was not only a function of boundary layer size but also of boundary layer distortion and degradation [66]. In addition, they noted an increasing the amount of boundary layer ingested caused distorted conditions at the AIP, where as changing the Mach number had small effects on distortion but significantly contributed to the total pressure recovery.

As S-duct research progressed, passive and active flow control was implemented increasingly. Allan *et al.* continued experimental BLI in S-ducts in 2008 [68]. Allan *et al.* successfully implemented an optimization for VG placement to reduce distortion. The same team later implemented active and passive flow control [68, 69]. They saw positive results with VG and VG jet hybrids. The presence of secondary flow, losses and distortion at the AIP is indisputable and is a recurring theme in literature. BLI and ice buildup increase the chances of distortion and loss in the S-duct. According to Jin *et al.*, ice buildup on the cowl was investigated, restricting airflow and causes it to enter non-uniformly [70]. Ferrar *et al.* looked into passive flow control on BLI S-ducts [71] and Parham *et al.* implemented VG on BLI inlets [27]. Both passive flow control methods helped to reduce AIP distortion. Papadopoulos *et al.* [72], and Georgiadis and Yoder [73] found that the intensity of separation increases when shocks are present. Both ice buildup and shocks increase the likelihood of flow separating in the S-duct and increase the chances of

larger separation regions. The various poor conditions in an S-duct are acknowledged however, not investigated in the current research. Therefore any improvements would need to be further investigated before implementation.

VG and active flow control jets were implemented by Vaccaro *et al.* in 2015 [28]. The active flow control was more successful than the VG, however the VG still performed better over the baseline S-duct. Shortly thereafter, in 2017 to 2020, Gil-Prieto *et al.* [74, 75], MacManus *et al.* [76] and Tanguy *et al.* [15] computationally modeled S-duct distortion over a range of Mach numbers with and without the implementation of VG. Gil-Prieto and his team focused on visualizing the flow using PIV to investigate the main loss regions during separated flow, at the inner radii of the S-ducts. Tanguy and his team implemented VG and visualized the flow with PIV, their results showed the VG could reduce swirl and distortion. The main focus of their work was the contribution of VG to the unsteady flow conditions.

In 2018, Aref *et al.* continued work on VG in S-ducts at a range of Mach numbers 0.2 to 0.8. Optimization in S-duct geometry introduced by Ambros in 2018 reduced pressure loss and visualized numerically the stream-wise vortices at Mach 0.65 [77]. During this time Gil-Prieto *et al.* numerically determined the S-duct swirl metric coefficients using Delayed Detached Eddy Simulation (DDES), finding comparable results to the experimental work [78].

In the past, beginning from the fundamentals of Dean flow in 1927, there have been improvements in flow in integrated propulsion systems. However, the separation and distortion remain a problem that needs to be addressed. The work with implementing flow control over a range of Mach numbers is important in developing an S-duct that can deliver uniform air to the compressor face. Gaps in research have been revealed at $Ma \geq 0.8$ where transonic flow increases the likelihood of separation and distortion at the AIP. Work has

begun at RMC in addressing this area of research.

3.3.1 Previous S-Duct Research at The Royal Military College

The work specifically conducted at RMC was isolated since its relevance to the current work is much greater. The same baseline S-duct was used for the majority of this work. S-duct work at the RMC began in 2015 looking at the performance of an S-duct at an inlet Mach of 0.8 [79].

Work was performed by Asghar *et al.* to determine the influence of S-duct offset-to-length ratio and the aspect ratio of rectangular inlets [79, 80]. The S-duct tested had a diffusion ratio of 1.57 which is representative of S-ducts in the transonic flight regime. Static pressure was experimentally measured on the meridian in the S-bend axis of curvature, and total and static pressure was surveyed at the AIP. The exit static pressure recovery was found to be higher for reduced offset ratios, suggesting S-duct designs approaching a straight diffuser reduced distortion and separation. A computational study was performed on the same ducts and showed a similar trend, however the distortion and total pressure coefficients deviated from the experimental results. For that study, only total pressure at the AIP was measured, and no radial or circumferential velocity components.

Work in 2015 parameterized an S-duct geometry to more easily compare between designs. Key dimensions such as aspect ratio and area ratios were non-dimensionalized by the AIP diameter [81]. This was continued in 2017, examining the effects of offset-to-length ratio and inlet aspect ratio on the flow quality coefficients. In 2018, passive flow control in the form of tubercles was added to the S-ducts and improvement in the AIP flow quality metrics

was noted [82, 20]. Hickling *et al.* [43], Schneider [44], and Hancock [83] numerically modeled the passive flow control between 2019 and 2020. This was compared in 2020 to the experimental work performed by the author of this thesis and her team [5]. It was noted that the various turbulence models were not able to capture accurately the separation region. Consequently, the AIP flow quality metrics differed from the experimental work.

3.4 Computational Fluid Dynamics

The literature review to this point has focused on the modeling of secondary flows, specifically stream-wise vortices and separation, since these both lead to distortion at the AIP. Turbulent flow in pipes has been studied numerically by other researchers as early as McConalogue and Srivasava in 1968 [84]. This work was a large step towards filling a gap in knowledge on secondary flows through incorporating Dean's mathematical work in 1927 [22]. The research continued into turbulent pipe flow by Rowe in 1970 [17]. For the high-speed number flow in S-duct both compressible and separated flow are in play. In 1983 Vakili *et al.* built a Reynolds-Averaged Navier-Stokes (RANS) solver to aid in solving the compressible flow in S-ducts [45]. Their predictions underestimated the pressure distortion because of the simplifications in the model. Similarly, in 1992, Harloff *et al.* built an in-house RANS solver, specifically to predict three-dimensional flow in a non-diffusing S-duct [50]. The new numerical model improved the comparison of total pressure to the experimental work and they were also able to predict the presence of two CRV. Using other techniques, Anderson *et al.* compared three-dimensional reduced Navier-Stokes (RNS) and implicit full Navier-Stokes (FNS) analysis in diffusing S-duct flow [54]. Again, progress on the modeling allowed them

to better predict the behaviour of three-dimensional flows and separation, but they were still unable to match experimental data.

It took until 1997 for Hellsten to make improvements to Menter's $k - \omega$ model, a type of RANS model, making it more rotationally invariant: not dependent on the angular velocity components and can be used with rotating reference frames [85]. Hellsten was able to accomplish this by adding onto a blending function known as the Shear Stress Transport (SST) function. This uses the proximity to the wall to blend the $k - \omega$ and $k - \epsilon$ models. Near a no-slip condition wall, the $k - \omega$ model predicts flow better since it is able to model viscous boundary layers better. In the free-stream, $k - \epsilon$ is used to reduce the computational cost and it predicts turbulence dissipation better than $k - \omega$. The $k - \epsilon$ and $k - \omega$ SST models were compared fir diffuser flow separation in 1999 by Apsley and Leschziner [86]. They evaluated the performance of turbulence models in a diffuser experiencing separated flow to determine which model was best at predicting separation. Their $k - \epsilon$ model failed to predict early separation where as the $k - \omega$ model captured the separation but shows weak re-circulation and therefore losses. In their results, the $k-\omega$ SST model separated early but did not match the experimental work at the outlet. Apsley and Leschziner concluded that the best model for their application was the $k - \omega$ SST model as in comparison to the $k - \epsilon$ it better predicted the flow phenomena [86].

Once the turbulence models were created to work better with separated and compressible flow, research turned to passive and active flow control modeling. In 2001, May computationally and experimentally modeled VG on an S-duct inlet at Mach 0.6 [87]. Their Navier-Stokes model was less computationally heavy and required a vortex circulation coefficient from the simplified equations, which if predicted properly, could better match experimental work.

Beale *et al.* looked into S-duct distortion comparison in numerical and experimental work, trying to determine the turbulence model that could properly predict the separation point and the extent of the separation region [88]. Using their own proprietary models, they found it difficult to match the distortion coefficients and recommended making a swirl generator to match the experimental findings. In 2002, Allan *et al.* implemented VG vanes and jets onto a flat plate, modeled it using Spalart-Allmaras (SA) and compared the results to $k-\omega$ SST [26]. The CFD and experimental work agreed well except for the vorticity in close proximity to the VG vanes. The predictions from the SST turbulence model matched the test daa better than those of the SA model. Menzies *et al.* modeled S-ducts using $k-\omega$ SST and Euler models [89]. While the Euler model is significantly less computationally intensive, the $k-\omega$ SST model was able to predict the flow at the AIP better when compared to the experimental work they performed. In 2003, Brear *et al.* used the $k-\omega$ SST model to predict successfully flow separation in an S-duct at an inlet Mach number of 0.8 [14]. Brear and his team examined that the distortion can significantly increase as Mach number increases, and the boundary layer grows and separates. They noted a pair of CRV downstream the first bend in the S-duct after a separation region. Brear *et al.* observed that the separation region contributes significantly to the unsteady conditions at the exit.

Berrier *et al.* in 2004 and 2005 focused on BLI inlets at a range of Mach numbers, using the NASA-developed RANS solver based on the $k-\omega$ SST turbulence model [66, 67]. They found that increasing the BLI reinforced observations of increased distortion in the S-duct, led to a higher likelihood of separation and poor flow metrics at the AIP. The computational study was able to capture the pressure recovery and distortion trends in their application. Predicting the separation points accurately has not been achieved in S-ducts.

In 2007, Sasha *et al.* focused specifically on the transitional flow in low Mach number S-ducts, $Ma = 0.17$ [90]. Beginning to break down the problem, they compared the $k - \epsilon$ and re-normalized $k - \epsilon$ and found the latter to be an improvement in predicting transition.

Allan *et al.* used passive flow control on a BLI S-duct in 2008 at Mach 0.85 and found the $k - \omega$ SST was able to predict the development of flow through the pipe, however the distortion coefficients did not match experimental work [68].

In 2013, Nguyen was able to model S-duct secondary flow using a $k - \omega$ SST for turbulence [64]. They found a vortex pair appearing at the first inner radius, starting at the corners of the rectangular inlet. These secondary flows were modeled by Harouni using a SA turbulence model [10]; Brear *et al.* using the NASA CNS program [14, 67]; Hickling using a SST and $k - \epsilon$ models [42] and others, as discussed later in this section [91, 85, 89, 90, 54]. The CRV generated in S-duct flow was noted by many studies experimentally and computationally. Overall the SST, $k - \epsilon$ and DDES models were able to predict AIP conditions similar to the experimental work. The SST and $k - \epsilon$ models are not able to properly predict the separation point but model the formation and dissipation of kinetic energy well for this application. The DDES model would better predict three-dimensional flows, however is more computationally heavy.

Other difficult-to-model flows include boundary layers, shock waves, and 3D rotational flow. In 2013, Georgiadis and Yoder used the $k - \omega$ SST model to predict separation for shock boundary layer interaction [73]. They were able to modify the proportionality constant to better predict the separation in a flow with shock waves. Gerolymos and Vallet used the $k - \epsilon$ model to try to predict 3D S-duct flow [91]. They were unable to predict satisfactorily all

their test results, but there is the potential to predict 3D flows with separation. Since S-ducts can have compressible flow and separated flow, using similar turbulence modeling techniques described here can be beneficial. Gil-Prieto *et al.* in 2016 used DDES to predict the S-duct flow, as it is beneficial to predict the 3D rotational flow [92]. They recommended that passive and active flow control would help with the unsteady osculations and vortices forming at the bends. In 2015, Asghar *et al.* used the $k-\omega$ SST model to predict the distortion of an S-duct at Mach 0.8 [81]. While the AIP trends in total pressure were comparable to the experimental data, the coefficients of total pressure and distortion differed. MacManus *et al.* varied the inlet Mach number and modeled an S-duct using DDES [76]. They noted unsteady flow and the strong presence of distortion at the AIP. The unsteady swirl peaked at twice the time-averaged results, which are typically presented. Unsteady analysis is not included in this work as the experimental results are assumed to be steady.

Passive flow control have been implemented in S-ducts to reduce the separations at inner radii. In 2018, Aref *et al.* implement VG on S-ducts over a range of Mach numbers, 0.2 to 0.8, and evaluated it using an internally built RANS model [93]. They noted that the VG decreased flow distortion by 79% but also decreased pressure recovery.

Improvements can be made through matching the experimental work more closely by adjusting or carefully selecting the turbulence model. Hickling recommended, for the S-ducts used in this experimentation, to continue work using DDES [42, 94]. Hickling *et al.* found their CFD simulation of S-ducts matched the total pressure coefficient closely but did a poor job predicting the other distortion and swirl coefficients [43]. In 2019, Schneider compared the S-duct experimental results using a RANS and DDES model [44]. The DDES

model was not completely converged and took 45 CPU days to run while the RANS only took 5 CPU days. With this significant increase in computational cost, the not converged DDES model does not show comparable C_p of the duct to the experimental work. DDES is also known to predict poorly, total pressure distortion, while predicted distortion flow quality coefficients were up to 60% different, as discussed by Schneider in [44]. The computation took 45 CPU days to solve and was not fully converged, leading to the large discrepancy in the coefficients. The S-duct results were corroborated by numerical research by Hancock in 2020 [83]. They used a RANS k-ϵ model at an inlet Mach number of 0.8. The DDES is theorized to predict better the S-duct results by using Large Eddy Simulation (LES) in the bulk flow and RANS near the walls of the duct. The increase in computational cost was too significant, therefore the RANS k-ε model is chosen for this analysis. Being able to model accurately the S-duct AIP conditions would allow the design of the S-duct to be completed quicker, by using a CFD optimization to find a final design. The current gap in the research is lack of set up to design an S-duct using 3D RANS modeling before experimentally testing.

This review has presented the relevant published research on flow in S-ducts, reaching from the fundamentals of Dean flow in 1927. Through early experiments and numerical predictions on flow distortion and flow control there have been improvements in the understanding of flow in integrated propulsion systems however, separation and distortion remain a problem that needs to be addressed. Implementing flow control over a wide range of inlet Mach numbers is important in developing an S-duct that can deliver air uniformly to the compressor face. Gaps in research have been revealed at $Ma \geq 0.8$ where transonic flow increases the likelihood of separation and distortion at the AIP. Research at RMC and elsewhere has advanced the understanding of passive

flow control and tubercles in particular, addressing this important area of research. Present work is a continuation on the previous flow control designs to investigate total pressure and distortion improvements in AIP conditions.

4 Experimental Method

This Chapter reviews the facilities, instrumentation and procedure used in the experimental work.

4.1 Test Facilities

Driven by vacuum, the wind-tunnel used in this experimental work draws air through the bellmouth inlet. Air is evacuated from three tanks, sealed from the lab by a gasket isolating the tanks from the test section. Figure 4.1 shows the layout of the test configuration. A detailed arrangement of the test section is displayed in Fig. 4.2.

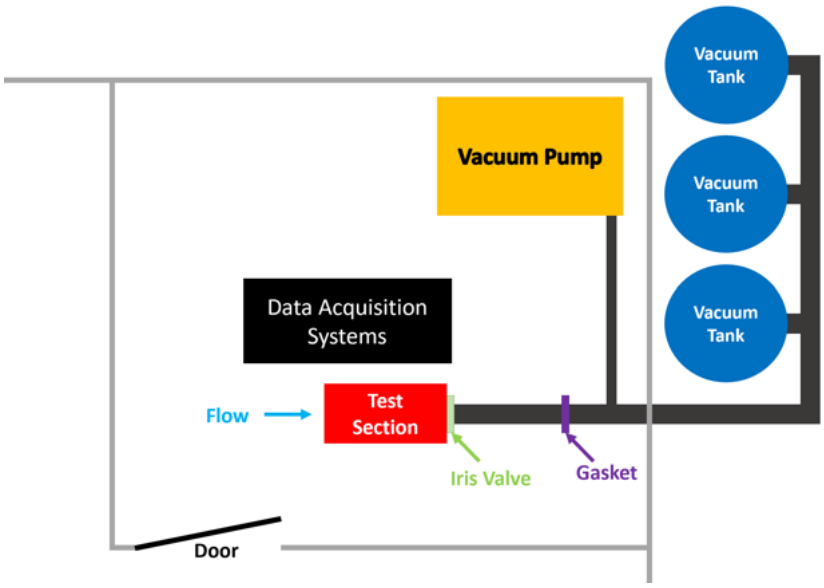

Figure 4.1: Lab room configuration depicting test section, tanks, vacuum and DAQ

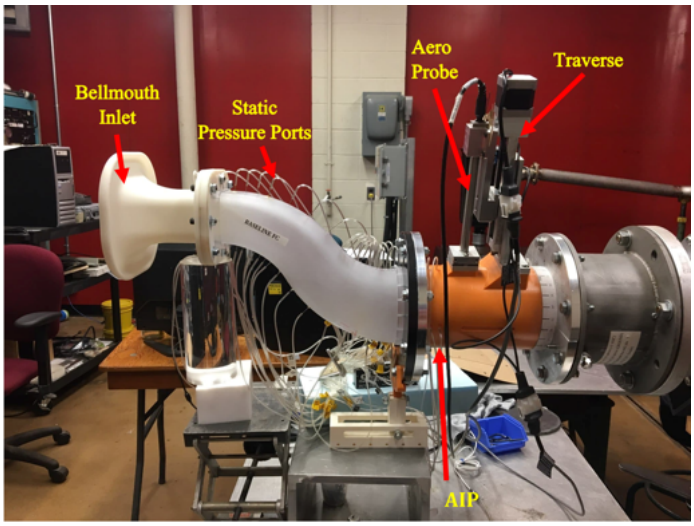

Figure 4.2: Test section

The test section and the duct connecting the wind tunnel to the vacuum

pump and test section are all supported to reduce vibration in the test section. Once a near vacuum is reached in the tanks, the thin gasket is punctured by an actuation mechanism. Air is immediately drawn through the test section, providing over 3 seconds of steady-state flow for the set Mach number of 0.8. The run duration can be longer or shorter depending on desired Mach number. The Mach number is set just downstream the test section and instrumentation, by an iris valve shown in Fig. 4.3. The iris valve can be opened or closed to adjust the throat area at this point, changing the mass flow rate through the test section until it ceases to be a choke point.

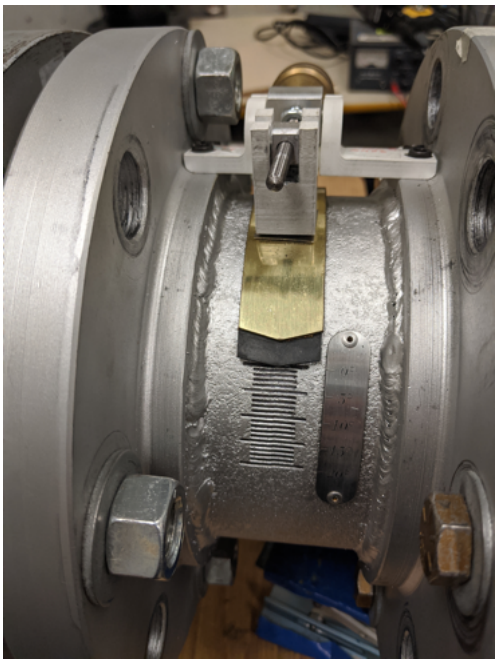

Figure 4.3: Iris valve used to set Mach number

The Mach number was set by running the wind tunnel and recording the conditions at the inlet, then adjusting the iris valve accordingly. The $\mu - DAQ$ was configured to measure the velocity at the first static port on the bellmouth to determine the inlet Mach number. This process was repeated until S-duct inlet Mach number was 0.8.

4.2 Test Section

The test section consists of the bellmouth intake, S-duct, and straight duct for instrumentation at the exit. Figure 4.2 depicts the S-duct test section downstream of a bell-mouth at the inlet that provides smooth, uniform flow to the S-duct and to the instrumentation at the AIP. In practice, the engine face is located at the AIP with a small section of straight duct connecting the inlet to the engine. Two key instruments were used, the μ-DAQ used to measure surface static pressure along the bellmouth and S-duct, and a 5-hole *Aeroprobe* at the AIP.

Along the duct there are pressure taps lined with small metal tubes that jut out connected to flexible tubing. These static ports were included in the printing of the model to ensure they are uniform, perpendicular to the surface, and sealed. The plastic tubing connects to a small manifold that is attached to the μ-DAQ data acquisition system.

The *AeroProbe*, on the right of Fig. 4.2, is attached to a linear traverse that moves the probe tip from the wall of the duct to the centre-line. The angle of the duct is set by rotating the straight tube, using a digital inclinometer, for a full 360° scan at 30° increments. The total and static pressures were measured using the *AeroProbe* to determine the angles and velocities with respect to each axis. Figure 4.4 is provided from the *AeroProbe* manual.

There are two different configurations for their 5-hole probe, for the present tests the one with a 90° bend at the tip, on the left of Fig. 4.4, will be used in the experimentation.

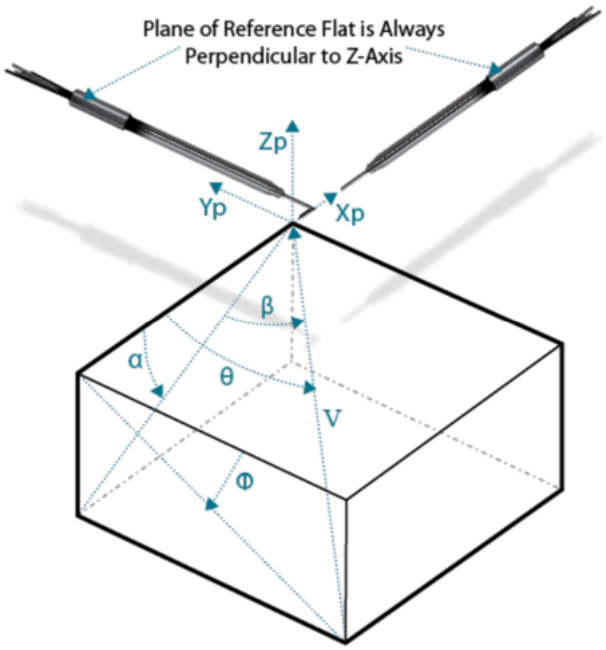

Figure 4.4: *AeroProbe* orientation options [19]

The *AeroProbe* measures pressure out of five different holes spaced around the tip. The pressure measurements are then converted through the *AeroProbe* data acquisition system into velocities in the x, y, and z directions and angles respective to each axis. The *AeroProbe* is calibrated from Mach 0.5 to 1.5, well encompassing the range of speeds seen in this application. The probe is attached to a linear traverse that moves the probe tip from the wall to the centre-line of the instrumentation duct. The instrumentation duct is rotated at 30° for the entire AIP. The probe collects data at 10 kHz sampling time

and travels at a speed of 25.4 $\frac{\text{mm}}{\text{s}}$ (1 $\frac{\text{in}}{\text{s}}$), this speed is less than 1% of the free-stream, contributing just 0.05% change in the angle of attack. The data collection is continuous from the wall of the S-duct to the center-line for each angle measured. It is considered negligible and is well within the measurement uncertainty. The *AeroProbe* was suitable for characterizing the tubercle-scale flow phenomena with a maximum diameter to tubercle amplitude ratio of 0.66.

4.2.1 S-Duct Test Article

The baseline S-duct does not have any flow control implemented. The flow control ducts were designed such that the boundary layer is a fraction of the tubercle height which ensures the high-momentum free-stream flow mixes into the boundary layer. The tubercle shapes from previous work conducted by Asghar *et al.* are used in this project [20, 82]. Figure 4.6 and Table 4.1 show the three previous tubercle designs, with diameter D being at the AIP. The tubercles are located at both inner radii as depicted in Fig. 4.5. The tubercle geometry was modified to fit the inner radii of the S-duct with a circular cross section. The cross-sectional flow area was maintained constant compared to the baseline when implementing tubercles as to not create a constriction.

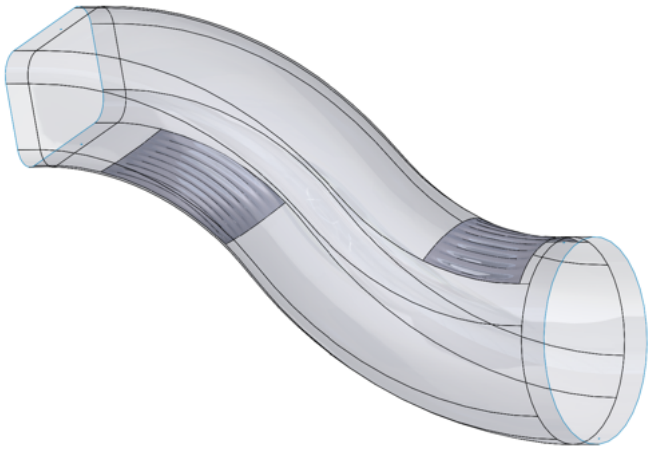

Figure 4.5: Tubercle locations in S-duct

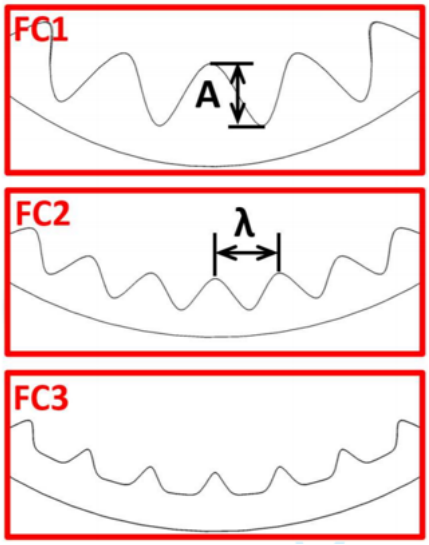

Figure 4.6: S-duct tubercle shapes tested by Asghar *et al.* [20]

The previous research was used as a baseline for the present experiment to gather more data and modify the design. FC2 showed improvement compared

to FC1, as is discussed in Section 3.3.1, which led to the design of FC3. FC3 is based on the amplitude and wavelength of FC2 with an innovation: an asymmetric configuration consisting of a reduced valley amplitude and increased peak amplitude. It was hypothesized that the low-momentum boundary layer fluid was collected in the troughs leading to the design of reduced trough depth in FC3. In the previous work the baseline and FC3 ducts have been tested without measuring static pressure and respective flow angles at the AIP. In the current work the baseline, FC3 and new design of FC4, in Fig. 4.7, are tested and both total and static pressure and flow angles are measured at the AIP.

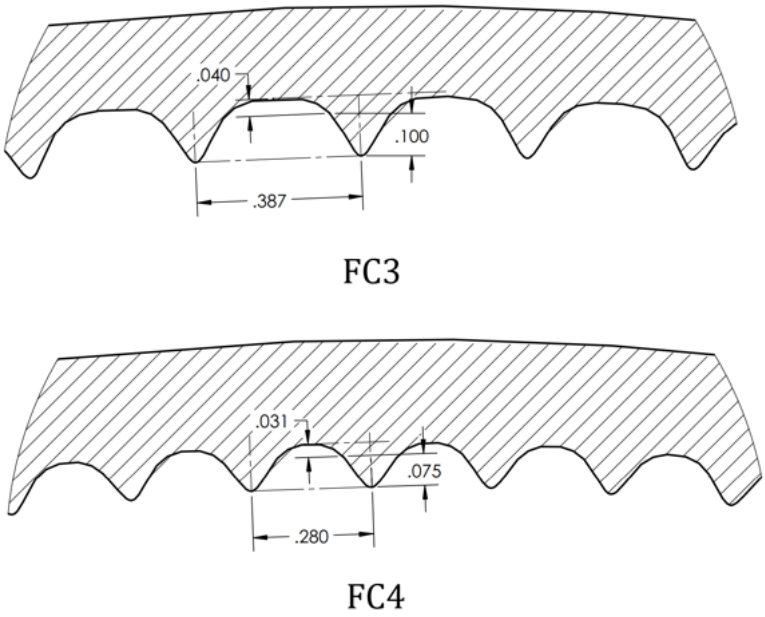

Figure 4.7: FC3 and FC4 tubercle shapes

Table 4.1: Flow Control Sizes

Parameter	FC1	FC2	FC3	FC4
$\frac{A}{D}$	0.0513	0.0250	0.0175	0.0133
$\frac{\lambda}{D}$	0.1310	0.0968	0.0968	0.0700

These two tubercle geometries will be investigated in this project alongside the baseline duct to compare to the previous work and to determine their influence on flow quality at the AIP.

4.2.2 Static Pressure Measurement

To measure the performance of the S-duct, total and static pressure measurements are taken at the inlet and AIP, and static pressure is taken along the 0° and 180° meridians of the S-duct, along the surface with the second and first inner radii respectively, at the same locations as previous work. The total inlet pressure is equal to the atmospheric static conditions and are measured in the room. Static pressure is measured at the inlet as well as along the length of the duct, at small holes in the duct wall, connected through *Tygon* tubing to a μ-DAQ unit. The μ-DAQ unit collects data at 2 kHz with an accuracy of $\pm 0.25\%$ of the 15 psi full scale range (± 0.375 psi) [95]. The static pressure holes are shown in Fig. 4.8 along the baseline S-duct. The flow control ducts use the same axial locations for static ports and the tubercle peak is instrumented. The measurement device has 32 channels and there are between 18 and 20 ports on the 0° and 180° surfaces, therefore two tests are needed for a full static pressure survey, one with each meridian. Evaluating the static pressure coefficient along the duct shows the regions of detached flow usually

at an inflection point and often by sustained constant $C_{p,x}$ when area is not constant. Note that Fig. 4.8 is inverted compared to the experimental setup and the AIP is located at $x = 12.729\,\text{in}$.

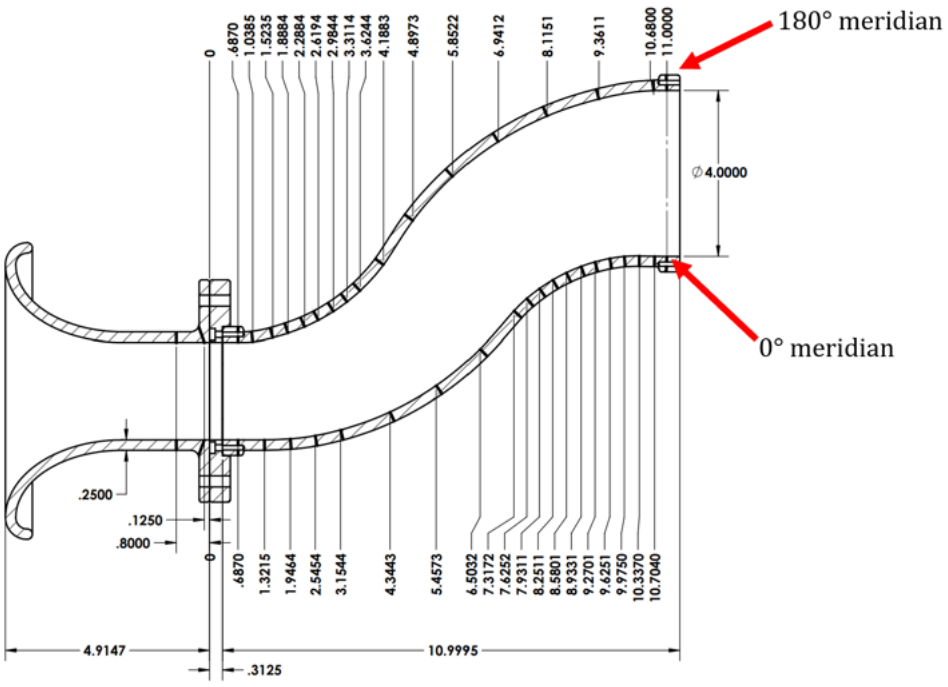

Figure 4.8: Static pressure ports along the baseline S-duct (all dimensions are in inches)

To set up the recording software, the μ-DAQ unit is activated and the software opened. The software must be organized for the specific system and measurement, with 32 active channels. It is properly zeroed before each run since the pressure sensors drift over time. Before any experiment is run, the recording software is calibrated, then initialized when the vacuum tanks have reached -20 mmHg. This is done to assure that data can still be recorded if the gasket ruptures prematurely. Once the test is run, the data is zeroed in

MatLab for any offset that may have emerged during the run. Using these values the Mach number can then be determined from the first static pressure port in the bellmouth.

4.2.3 Atmospheric Condition Measurement

The atmospheric conditions in the lab were taken from a thermometer and barometer. These measurements were recorded at the beginning of the experiment and at various points throughout the testing to capture any minor fluctuations. These measurements were used for the static room conditions, which is translated to total conditions for the test section inlet.

4.2.4 *AeroProbe* Sweep Traverse

The *AeroProbe* was used to sweep the AIP by sliding along a linear traverse. The total and static conditions were measured by this instrument and the velocity direction was determined using the *AeroProbe* software. Before the tests are run, the *AeroProbe* was calibrated and the traverse was set to a position against the wall of the instrumentation duct. It was set up to ensure the probe would align directly with the centre of the duct. This was done by traversing the probe to the center location and modifying the angle and height to match a cross hair wire that was mounted into the instrumentation duct. The probe was triggered automatically when a drop in pressure occurred, detected by the $\mu - DAQ$ system at the inlet. The program would move the linear traverse from the wall to the center of the duct during one steady state run while recording data from the *AeroProbe*. The *AeroProbe* was then tested in a straight duct at a Mach number of 0.8 to see if there was any distortion in the flow and the results were unremarkable. The measurements taken for

the S-ducts were implemented in the various flow quality metrics described in Section 3.3.1.

4.3 Data Processing

The μ-DAQ unit measurements are output as a pressure that can be directly used to calculate the coefficient of static pressure. The $\mu - DAQ$ measures 500 to 600 data points over the 3-seconds of steady-state run that are averaged for use in the flow quality equations. The *AeroProbe* data must be processed through the custom software, *AeroFlow2*, to output the pressure, velocity and respective angles. Before processing, they are smoothed using a Savitzky-Golay filter [96]. The filter uses a process referred to as convolution, matching adjacent data points to form a polynomial. This is done to reduce noise in the data prior to processing. The velocity components and angles are then used in a *MatLab* program to determine the flow quality metrics presented in Section 4.4.

4.4 Flow Quality Coefficients and Metrics

Figure 4.9, shows the baseline duct, the rectangular inlet is on the lower left and the air diffuses to a circular exit at the right. This duct has been used in the previous RMC work and was devised with a typical offset, diffusion, length-to-offset ratio and entrance aspect ratio that is commonly seen in aircraft, shown in Table 4.2. A non-circular inlet is typical of S-ducts when implemented on air vehicles to conform with the fuselage. Typical shapes include: oval, rectangular, D-shaped and trapezoid. The selected rectangle aspect ratio is representative of the non-circular inlets as determined by As-

ghar *et al.* [79]. It is designed for an inlet Mach number of 0.8, so diffusion is needed before air reaches the engine.

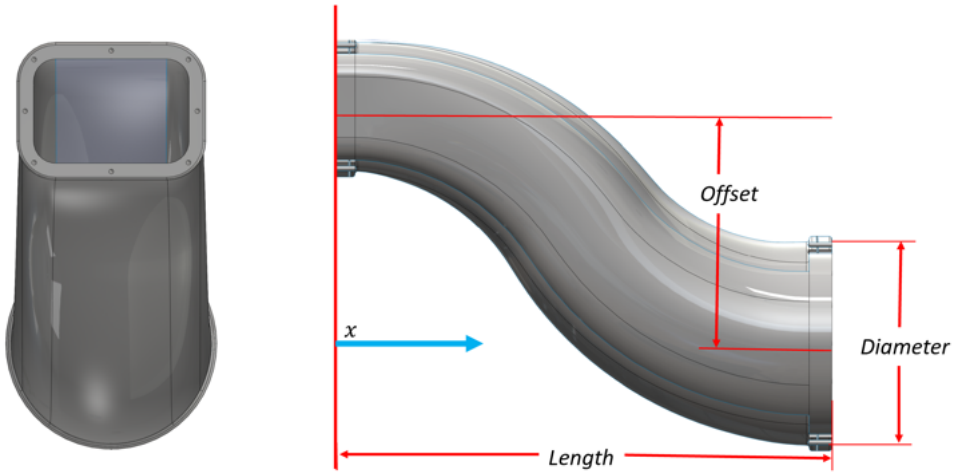

Figure 4.9: Baseline S-duct geometry front and side view

Table 4.2: Baseline S-Duct Geometry Parameters

Parameter	Value
Aspect Ratio	1.57
Offset-to-diameter ratio	1.30
Length-to-diameter ratio	2.70
Offset-to-length ratio	0.37

In the present S-duct experiments, the tubercles were situated at the areas of separation identified by measuring stream-wise static pressure along the surface of the baseline duct. To situate passive flow control devices, the point of separation was determined from baseline duct measurements and the tubercles were placed in the region of separation, starting upstream to induce CRV

aimed at mitigating or eliminating the separation region. The two regions where tubercles are implemented on the inner radii are shown in Fig. 4.10, reiterated from Section 1.1. Here the static ports are also on the inner radii with higher concentrations to detect the regions of separation.

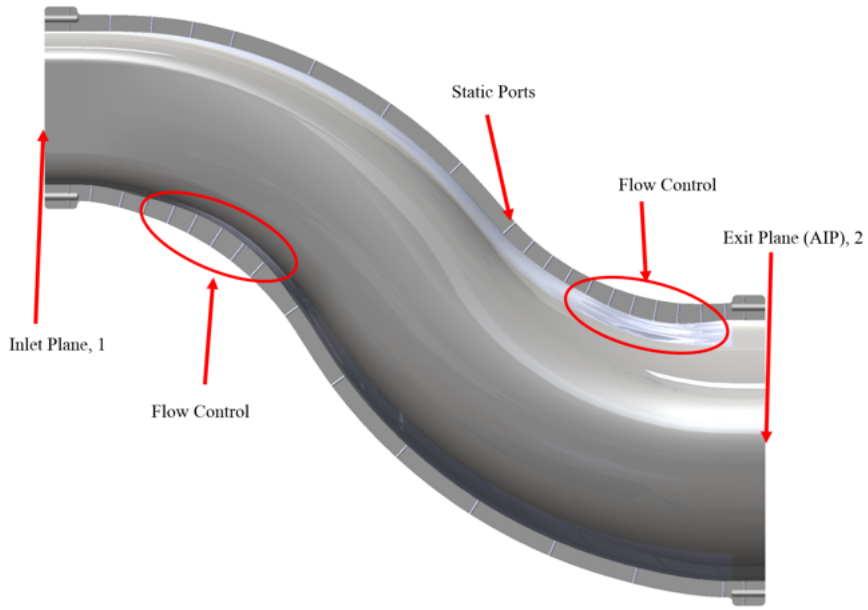

Figure 4.10: S-duct with details showing flow control regions

4.4.1 Coefficient of Static Pressure

The coefficient of static pressure ($C_{p,x}$) depicts how the flow is changing in velocity along the length of the duct as well as if there are any regions of separation. In regions of separation, the flow can be stagnant or recirculating. This is usually evident by a region of uniform static pressure. Equation 4.1 defines the coefficient of static pressure based on the inlet total ($p_{0,1}$) and static pressures ($p_{s,1}$), and the static surface pressure at a known axial location, x,

down the duct, $p_{s,x}$. The inlet static pressure is found using the first 0° meridian static port.

$$C_{p,x} = \frac{p_{s,x} - p_{s,1}}{p_{0,1} - p_{s,1}} \tag{4.1}$$

4.4.2 Total Pressure Ratio

The area averaged total pressure ratio ($\bar{\pi}$) throughout the duct is calculated through taking the average at the inlet and exit total pressures, as shown in Equation 4.2. This is the first of four coefficients that depicts the degree of total pressure loss at the AIP. This equation shows the duct's ability to diffuse the air efficiently. Having a high total pressure coefficient reflects a S-duct's ability to compress the air before it reaches the engine, leaving less work for the compressor to do. If an inlet is able to deliver a high total pressure coefficient, then there are not many losses over the length of the duct. In an ideal S-duct, $\bar{\pi}$ would be unity. Furthermore, the goal is to have uniform high pressure across the compressor face. Equation 4.2 uses $\overline{p_{0,1}}$ and $\overline{p_{0,2}}$, the area averaged total pressures for the inlet and exit (AIP) respectively.

$$\bar{\pi} = \frac{\overline{p_{0,2}}}{\overline{p_{0,1}}} \tag{4.2}$$

4.4.3 Circumferential Distortion Coefficient

The second coefficient that characterizes total pressure loss is the circumferential distortion coefficient ($DC(60)$) depicts the 60° sector (j) at the AIP with the largest variation in total pressure. Equation 4.3 is used to determine the distortion coefficient based on a 60° sector at the AIP. This was developed

by SAE [56]. The 60° sector is evaluated at 30° increments around the AIP, giving 12 possible sectors. Then, once calculated for each section, the distortion coefficient is concluded to be that of the sector with the greatest total pressure drop, corresponding with the most distorted sector.

$$DC(60) = \max\left(\left|_{j=1}^{12} \frac{\overline{p}_{0,2} - \overline{p}_{0,j}}{\overline{p}_{0,2} - \overline{p}_{s,2}}\right.\right) \tag{4.3}$$

4.4.4 Radial Distortion Coefficient

The radial distortion coefficient ($DRPR_{\max}$) examines the pressure for rings of equal area at the AIP, as illustrated in Fig. 4.11. This is the third of the four total pressure loss coefficients. It is based on the difference between the AIP averaged total pressure and the averaged total pressure for a given ring. The maximum difference amongst the five rings is defined as the radial distortion coefficient $DPRP_{\max}$ as shown in Equation 4.4 developed by SAE [56]. This equation uses average total pressure at area-averaged rings and compares it at around the AIP, where i is one of 5 annulus locations, averaged around the AIP.

$$DPRP_{\max} = \left(\frac{\overline{p}_{0,2} - \overline{p}_{0,2,i}}{\overline{p}_{0,2}}\right)_{\max} \tag{4.4}$$

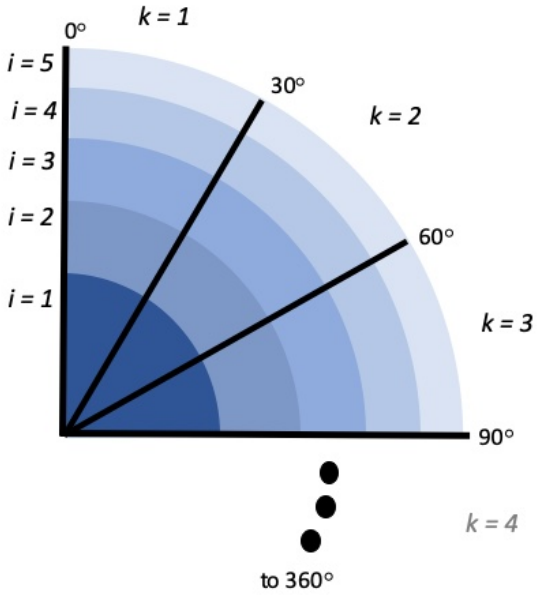

Figure 4.11: Sector and radial identification for distortion coefficient determination at the AIP [5]

4.4.5 Angular Distortion Coefficient

The angular distortion coefficient ($DPCP_{\text{ave}}$) uses each point i, k shown in Fig. 4.11, and area averages it based on the comparison to the average pressure of the i^{th} ring. This is the final total pressure based distortion coefficient. Equation 4.5, developed by SAE [56], is used to calculate the this coefficient using the relation between the total pressure at a i, k, and the average pressure in its respective ring. If some pressure i, k is greater than, or equal, to the average, then the term in the brackets is set to unity. If it is less than the average, then the value inside the brackets is reduced. This equation is applied

at 12 different angles, denoted by k, and 5 different radius locations, denoted by i, Fig. 4.11.

$$DPCP_{\text{ave}} = \frac{1}{5}\sum_{i=1}^{5}\left(1 - \frac{\sum_{k=1}^{12}\begin{cases}\frac{\overline{p}_{0,2,i,k}}{\overline{p}_{0,2,i}} & \overline{p}_{0,2,i,k} < \overline{p}_{0,2,i} \\ 0 & \overline{p}_{0,2,i,k} \geq \overline{p}_{0,2,i}\end{cases}}{\sum_{k=1}^{12}\begin{cases}1 & \overline{p}_{0,2,i,k} < \overline{p}_{0,2,i} \\ 0 & \overline{p}_{0,2,i,k} \geq \overline{p}_{0,2,i}\end{cases}}\right) \tag{4.5}$$

4.4.6 Flow Angle

The Swirl Index (SI) depicts the magnitude of rotational flow angle, area averaged at the AIP. The goal for an inlet design is to reduce the amount of swirl in the inlet, so that the engine and specifically the compressor, receives uniform axial flow. Equation 4.7 is used to calculate the swirl intensity (SI) based on methods from the SAE report [56] and conventions described by Gil-Prieto *et al.* [78, 97]. The swirl intensity describes the magnitude of swirl at the AIP through the magnitude of swirl angle, ($SS^{+}_{i,k}\theta^{+}_{i,k}$,$|SS^{-}_{i,k}\theta^{-}_{i,k}|$). Where $\theta_{i,k}$ are the angular extent of swirl and $SS_{i,k}$ is the mean swirl angle for the region. The mean swirl angle, α, is calculated in this work from Equation 4.6 is the angle between the local velocity discounting any radial components and the axial direction. This helps show the magnitude of vorticity at the AIP induced by secondary flow. The angular velocity, v_θ, shown in Fig. 4.12, is tangential to any radial and the axial velocity, v_x, is into the page.

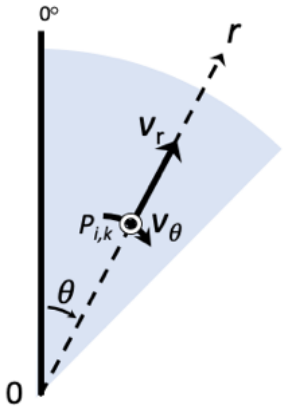

Figure 4.12: Section of the S-duct AIP showing radial and circumferential components [5]

$$\alpha = \text{atan}\left(\frac{v_\theta}{v_x}\right) \tag{4.6}$$

$$SI(i) = \frac{\sum_{k=1}^{m} SS_{i,k}^{+}\theta_{i,k}^{+} + \sum_{k=1}^{m} |SS_{i,k}^{-}\theta_{i,k}^{-}|}{360} \tag{4.7}$$

For the current work there are five i rings however, in the swirl metrics only one value was calculated. The area average was taken for all the sectors, simplifying Equation 4.7 to Eqn. 4.8.

$$SI = \overline{|\alpha|} \tag{4.8}$$

The swirl index at the AIP could not previously be determined because the instrument used was a 5-hole rake probe that only measured axial flow [20]. The *Aero-Probe* is a 5-hole probe that can measure flow angle as well as the speed along each axis.

4.4.7 Swirl Directivity

The Swirl Directivity (SD) reveals the presence of bulk swirl, based on Eqn. 4.9 described by Gil-Prieto *et al.* [78]. If SD is positive, it indicates bulk swirl in the clockwise direction; if SD is negative, bulk swirl is counter-clockwise. If SD is zero, there is no bulk swirl, calculated looking downstream.

$$SD(i) = \frac{\sum_{k=1}^{m} SS_{i,k}^{+}\theta_{i,k}^{+} + \sum_{k=1}^{m} SS_{i,k}^{-}\theta_{i,k}^{-}}{\sum_{k=1}^{m} SS_{i,k}^{+}\theta_{i,k}^{+} + \sum_{k=1}^{m} |SS_{i,k}^{-}|\theta_{i,k}^{-}} \tag{4.9}$$

For the current work there are five i rings however, in the swirl metrics only one value was calculated. The average was taken for all the sectors, simplifying Equation 4.9 to Eqn. 4.10.

$$SD = \frac{\overline{\alpha}}{\overline{|\alpha|}} \tag{4.10}$$

4.4.8 Swirl Pair Coefficient

The Swirl Pair coefficient (SP) evaluates the number of pairs of CRV present at the AIP, based on Eqn. 4.11 described by Gil-Prieto *et al.* [78]. For example if SP is equal to 2, there are two pairs of CRV.

$$SP(i) = \frac{\sum_{k=1}^{m} SS_{i,k}^{+}\theta_{i,k}^{+} + \sum_{k=1}^{m} |SS_{i,k}^{-}|\theta_{i,k}^{-}}{2 \times \max\left[\sum_{k=1}^{m} SS_{i,k}^{+}\theta_{i,k}^{+}, \sum_{k=1}^{m} |SS_{i,k}^{-}|\theta_{i,k}^{-}\right]_{k=1\ldots m}} \tag{4.11}$$

Similarly to the other flow control metrics, only one value for SP is determined and therefore Equation 4.11 can be simplified to Eqn. 4.12.

$$SP = \frac{\overline{|\alpha|}}{2 \times \max\left[|\overline{\alpha^-}|, |\overline{\alpha^+}|\right]} \tag{4.12}$$

4.5 Test Matrix

The surface scans were performed for all test S-ducts at the 0° and 180° meridians. The AIP was traversed for each angle shown as the test plan for each duct:

- Surface static pressure scan: at 0° and 180° meridians.
- AIP measurements of static and total pressure, and $x-$, $y-$, and $z-$ velocities: continuously measured radial every 30° from 0° to 330°.

5 Computational Method

The computational work was done in two parts. The first part was an automated program that defines tubercle geometry through three parameters: the positive amplitude radially inward, the negative amplitude radially outward, and the wavelength. The second part was performing the CFD set up on the baseline S-duct to ensure the automation correctly prepared the input files for *ANSYS Fluent*. The end result of this work is to create an automation program to implement tubercle geometry based on three parameters that outputs a mesh. It has been structured to be compatible with optimization of tubercle geometry in S-ducts.

5.1 Automation Procedure

Three programs were used in sequence, *SolidWorks*, *Pointwise* and *ANSYS Fluent* connected with the automation procedure, done in *Python*. The initial geometry and tubercle profile, created in *Python*, was then exported to *SolidWorks* to create the new duct surface. The *SolidWorks* surface was exported to *Pointwise* to be meshed, then to *ANSYS Fluent* for solving. The *SolidWorks* program took a comma separated values (csv) file of points at the defining plane along the tubercle profile and created a curve. The process of

this automation is laid out in Fig. 5.1.

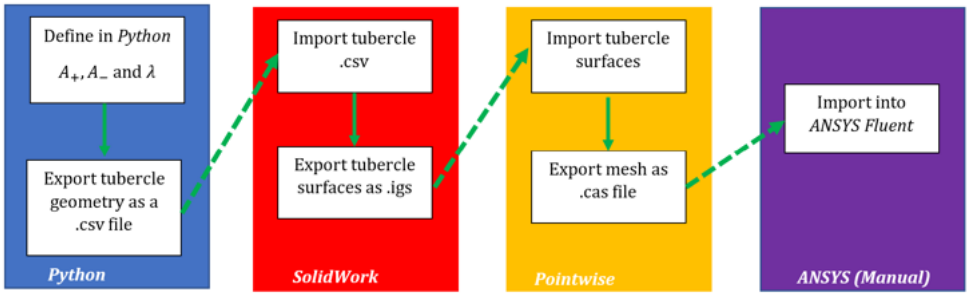

Figure 5.1: Automation process used to create the input mesh file for *ANSYS Fluent*

The overall automation of running programs was done using *Python 3.8*. The first step, profile script, took a csv input of the three design parameters and then it output a tubercle profile to match the S-duct, as described in Section 5.1.1. The automation program then opened *SolidWorks* and imported, lofted and exported surfaces using a visual basics application (VBA) macro, see Section 5.1.2. The output surface was imported into *Pointwise* with the automation script. The automation script began the *Pointwise* Glyph Script to open the baseline S-duct mesh, overlay the tubercle surfaces and re-mesh, as detailed in Section 5.1.3.

5.1.1 Profile Script

The initial stage of the automation is creating the tubercle profile using *Python 3.8* with the three design parameters presented in Fig. 5.2 as inputs. The parameterization was set up to be able to take the previous design inputs to recreate the FC ducts.

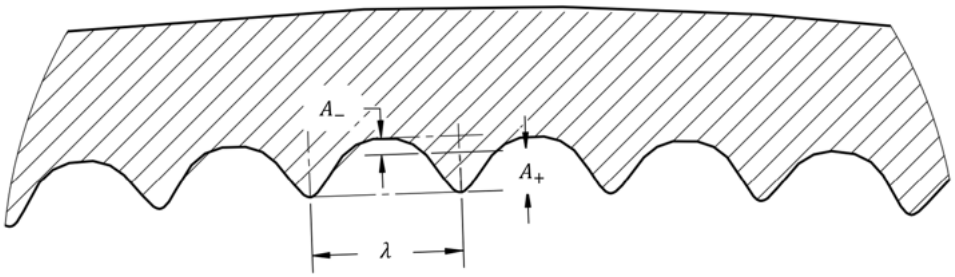

Figure 5.2: Tubercle design parameters

The profile script code takes the three key design parameters through a csv file to allow for multiple geometries to be created simultaneously. There is a set location for the 2D tubercle profiles at the first and second inner radii of the S-duct. The tubercle profile is generated through a four point profile and a spline is applied to the points to get a continuous profile. It adjusts the curvature of the profile to fit the baseline duct and ensures the flow area at the tubercle locations is not changed. A continuous transition is assured between the remainder of surface in the duct when the spline is created for smooth transition from tubercles to duct, which will be described presently. The final profile for each tubercle location is exported as a csv file to be used in the surface development.

5.1.2 Surface Development

The surface development was done through the VBA based macro program included in *SolidWorks 2019*. The easiest method to develop a *SolidWorks* macro is done using the record and playback function however, this records mouse movement and does not work when the tubercle profile is modified. The restrictions in this ability are that as one file is imported, it is given a set of names and then calls on those names for other actions. The names

change for each imported file and needed to be overwritten for this macro to work continuously. The other obstacle faced when implementing the macro was that for some actions in *SolidWorks 2019* the macro only records mouse movement and does not record it with relation to the part. Therefore if the view is changed to another orientation or magnification, this option will fail. The problems in using *SolidWorks 2019* macro were difficult to overcome because of the limited documentation and small user base. For these reasons it is likely that the macro is version-dependent and will not operate consistently unless *SolidWorks 2019* is used. *SolidWorks* was implemented for the developing of surfaces since it was used in the previous iterations of the S-duct design, and consistency between iterations was a requirement for developing the automation tool.

The csv profile is then imported into *SolidWorks 2019* to the appropriate plane, where the tubercle geometry is located. Both inner radii have three planes to make the tubercle surface, shown for understanding in Fig. 5.3.

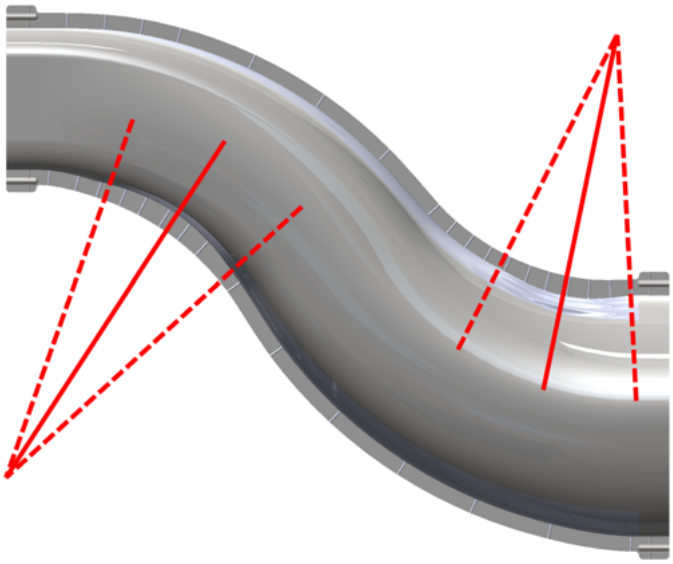

Figure 5.3: Baseline S-duct surface loft

The two outer planes ensure the geometry smoothly joins the baseline S-duct profile, shown as dashed lines. The middle plane receives the imported csv profile, displayed as a solid line. All designs have the same three tubercle planes which ensure that, when creating the mesh, there is a consistent surface size to transfer points to. Using the automation script, the baseline duct inner lofted surface is imported, shown in Fig. 5.4, inverted for clarity.

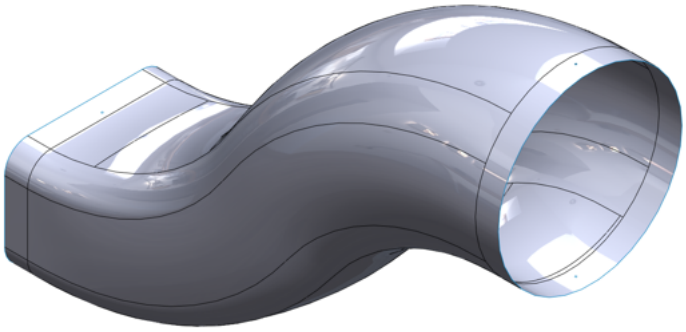

Figure 5.4: Baseline S-duct surface loft

Once the profiles are in place, the surface is lofted again, Fig. 5.5 shows the two tubercle surfaces in the same orientation as Fig. 5.4. The two tubercle surfaces are the only surfaces needed for the next step and they are exported as an initial graphics exchange specification (igs) file.

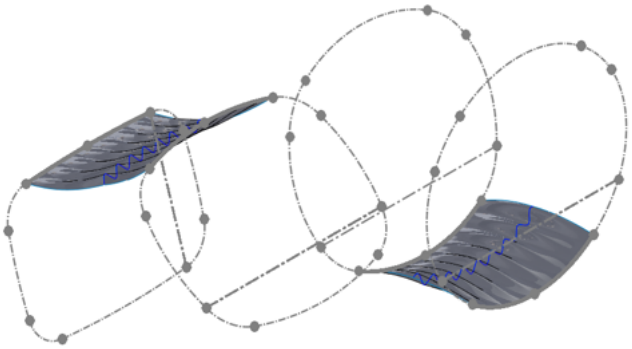

Figure 5.5: Tubercle lofted surface of the FC4 duct

5.1.3 Automated Meshing

Pointwise version 18.4 is used to create the automated mesh with the embedded Glyph script system. The baseline duct is meshed manually, discussed in detail in Section 5.2. The initial step in the Glyph script is to import the manually-meshed baseline S-duct *PointWise* mesh file, Fig. 5.6. Note that the axes in Fig. 5.6 are not consistent with experimental work. The exit of the duct is extended past the AIP using a straight duct such that the boundary conditions are not at the plane of interest. The length of this section is based on previous work.

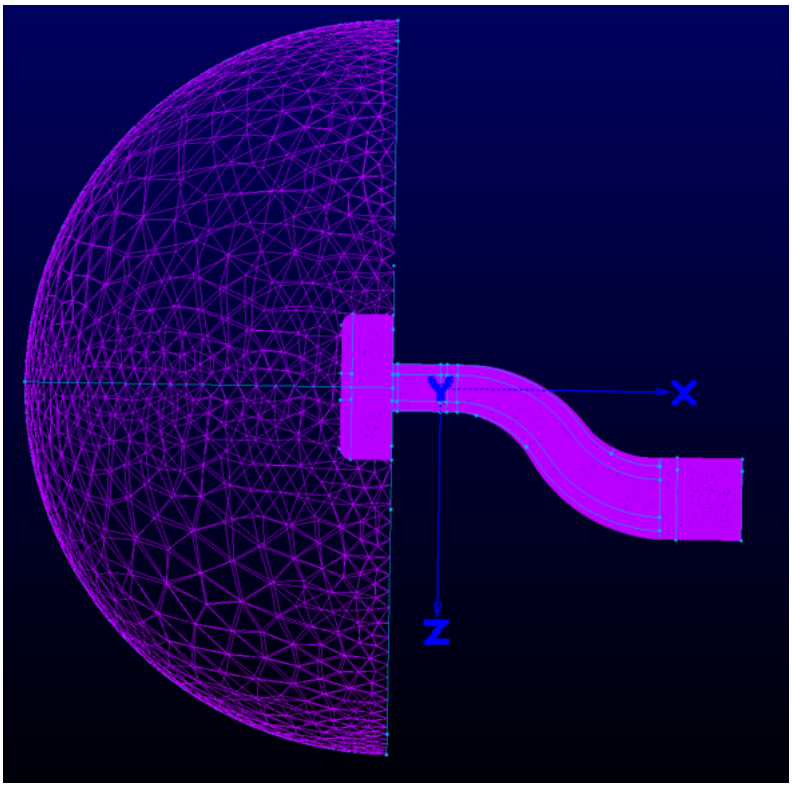

Figure 5.6: Baseline S-duct, inlet and outlet mesh

Then the exported tubercle surfaces are imported as a database using a *Pointwise* Glyph script, then scaled and translated to match the orientation of the baseline duct. The existing mesh is then overlaid onto the tubercle database, translating the surface points in this region to the tubercle surface. Then the entire duct is initialized for the new geometry and exported to *ANSYS Fluent* using the boundary conditions discussed presently. The baseline duct has a 17×10^6 cell unstructured mesh with refinement along the walls and higher refinement at the tubercle patches, ensuring a $y+$ less than unity. An area-average $y+$ of 0.28 was obtained in *Fluent*. An unstructured mesh was chosen in the free-stream with a structured boundary layer to improve the numerical prediction of complicated boundary layer flow and separation while allowing the remainder of the duct to be meshed easily for varrying tubercle geometries. The final mesh is exported as a case file (cas) for *ANSYS Fluent*.

5.1.4 ANSYS Fluent

This section discusses the set up of the *ANSYS Fluent* file for the baseline S-duct. Initially, the exported cas file from *Pointwise* was imported. The configuration of the *ANSYS Fluent* file was done to aid in modeling a compressible flow solution. The solver was set to *density-based* using a steady calculation. A *density-based* solver was used since it was initially designed for high-speed compressible flows, while the *pressure-based* solver is used for incompressible flow. A *time-steady* calculation was used to represent best the averaged experimental results at the AIP and reduces computational effort.

The turbulence modeling was done using the $k-\omega$ *SST* model with *compressibility effects*. A full turbulence model was used as the boundary layer in the S-duct transitions early in the duct. *ANSYS Fluent* uses the Wilcox $k-\omega$

model [98]. Wilcox looked into low Reynolds number modeling restrictions that were not needed in this study. Chapter 3 reviewed the previous work on CFD, here it is reiterated for relevance to the turbulence model choice. Hickling chose *realizable* $k-\epsilon$ to model S-ducts, and noted limitations in predicting distortion characteristics because of the models inability to model unsteady flow in separated regions [42]. The $k-\omega$ *SST* model shows excessive losses in some cases, but is better at predicting separation. Since the previous work done with $k-\epsilon$ under-predicted the size of the separation region, the $k-\omega$ *SST* model was chosen for the present work.

Other work by Gil-Prieto and his team used the DDES model which best predicts the highly unsteady flow [92]. The improvement was attempted by Hancock and Schneider however, after over 45 days of computing the solution had not converged [44]. The DDES model was not used in this work because of the high computational cost. For this project, since modeling the distortion was a high priority, the $k-\omega$ SST model was chosen. The energy equations were calculated for the model, meaning it calculates separately the temperature in the model, which is required for compressible flows.

Since the experimental results revealed asymmetric pressures and velocities at the AIP, the full duct was modeled in CFD without a symmetry plane. This is an extremely rare approach for numerical studies, most of the CFD work performed on ducts are assumed to be symmetric. The three boundary conditions are at the inlet, along the S-duct, and at the outlet. Figure 5.7 shows these boundary locations. Note that the axes in Fig. 5.7 are not consistent with experimental work.

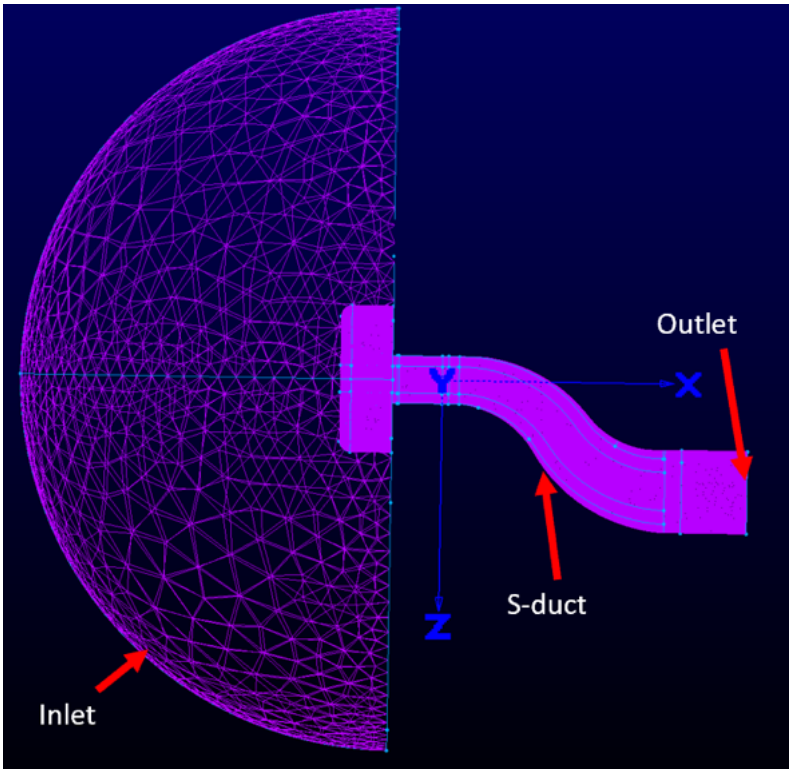

Figure 5.7: Baseline S-duct surface mesh with boundary conditions

The S-duct and bellmouth were set to an adiabatic, *non-slip wall* with standard roughness. The inlet is set as a *pressure-inlet* boundary set to a total pressure of 100 kPa, to reproduce the conditions seen in the experiments. The outlet was set at a total pressure of 63.5 kPa to achieve *Ma* 0.8 at the inlet of the S-duct. In the absence of any turbulence information, both the inlet and outlet were set to have a turbulent intensity of 0.1% and a viscosity ratio of 2.5. The low turbulent intensity was estimated from the stagnant room conditions in the experimental set up. To determine the outlet pressure, an initial guess of 65 kPa was used, then manual iterations were done once the solution had converged to reach the desired inlet Mach number.

The method used to calculate was the implicit formulation with second-order equations for flow, and first-order upwind equation for kinetic energy and dissipation rate. The mesh was initialized using the standard method based on the inlet parameters. The process was continued using the built-in multi-grid *fmg initialization*. This uses inviscid Euler equations and first-order discretization to obtain the approximate solution, leading to a faster convergence. To aid in quick convergence, the Courrant number was initially left at 5 then adjusted to 15 after a minimum of 1000 iterations and steady residuals.

5.2 Mesh Generation

Pointwise V18.4 was used to create an unstructured mesh with over 17×10^6 cells. In previous work, around 8 million cells were used for half an S-duct, the same structure was kept however, the full S-duct is now modeled. Refinement, in the form of *TRex* mesh, was applied to all walls. This generates small mesh cells along the walls and slowly transitions them to the free-stream mesh size, displayed at the AIP in Fig. 5.8. The steady transition is done using anisotropic tetrahedral elements. The *TRex* elements were set with a maximum number of layers of 25 and a growth rate of 1.3.

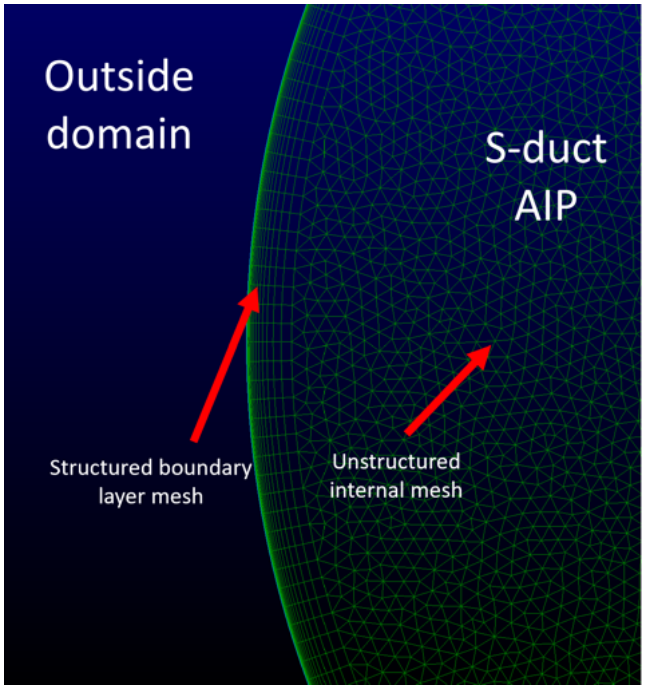

Figure 5.8: AIP of the baseline S-duct showing boundary layer mesh elements

A grid independence study was preformed on the half-S-duct studies by Hickling, Hancock and others [42, 43, 83, 99]. In their studies, a half duct with 8×10^6 to 10×10^6 cells were used with similar wall cell structures. Therefore, in the present work, the 17×10^6 cell full duct model was considered mesh independent.

It is noted that while the FC4 duct was not numerically tested, a converged simulation has been run proving that implementing tubercles does not distort the mesh. The proof of concept was done at a lower inlet Mach number and it was not iterated to set the proper Mach, therefore the results are not presented.

5.3 Convergence Criteria

To ensure each CFD run was converged, two conditions were verified. The first was ensuring the residuals were stabilized, so the absolute magnitude of results did not vary for a minimum of 1000 iterations. The scaled residuals of velocity in the $x-$, $y-$, and $z-$directions; continuity, k and ω were reduced around two orders of magnitude, all falling below 10^{-2}, however energy was slightly greater than 10^{-2}. The second important convergence condition was that the Mach number at the inlet plane was 0.8 and stable for a minimum of 1000 iterations. This ensured that the velocity in the duct would match that of the experimental work.

6 Experimental Results and Discussion

This section will discuss the surface pressure along the duct, AIP conditions and flow quality coefficients for the baseline, FC3 and FC4 ducts. This is complemented by the following chapter, the numerical result. First however, the validity of the results will be discussed by comparing the surface pressure measurements to those previously measured with the new *AeroProbe* and wind tunnel at RMC. All polar plots and coefficients are oriented looking downstream in the S-duct.

6.1 Static Pressure Coefficient

The surface pressure coefficients (C_p) are calculated using methods described in Section 4.4.1. The experimental results were evaluated to reveal any areas of separation within the duct. Uncertainty in C_p was calculated to be on the order of magnitude of 10^{-4} and is considered negligible, this is explained in Appendix A.

6.1.1 Comparison to Previous Experimental Work

The previous experimental work was completed by Asghar *et al.* in 2018 [20]. The new and old tests on the baseline duct results are shown in Fig. 6.2. Figure 6.1 is repeated here for clarity and interpretation of the C_p plots. Note that Fig. 6.1 is inverted compared to the experimental setup and the AIP is located at $x = 12.729\,\text{in}$.

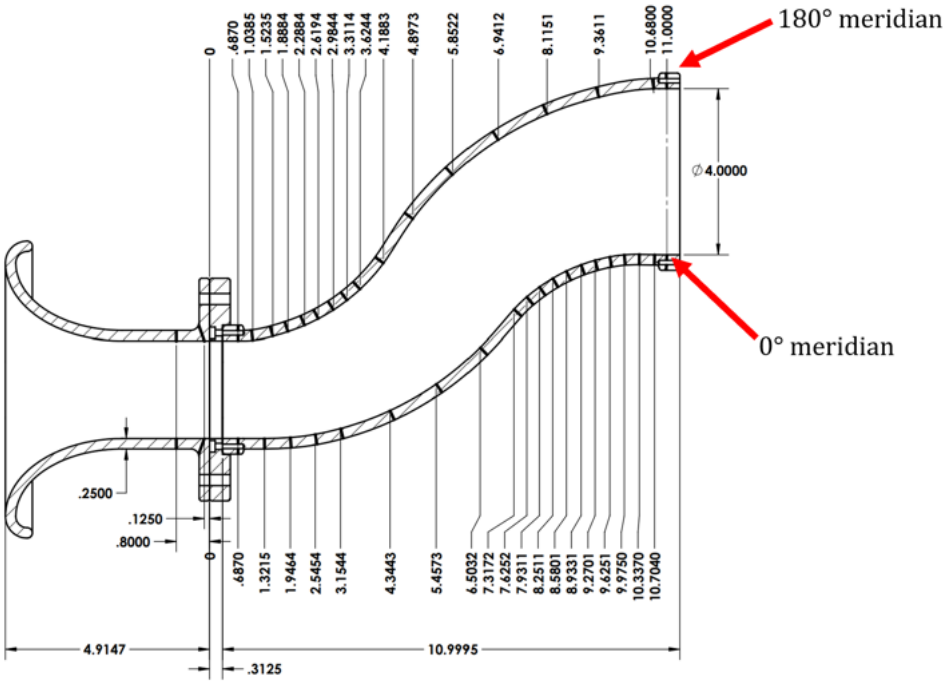

Figure 6.1: Static pressure ports along the baseline S-duct (all dimensions are in inches)

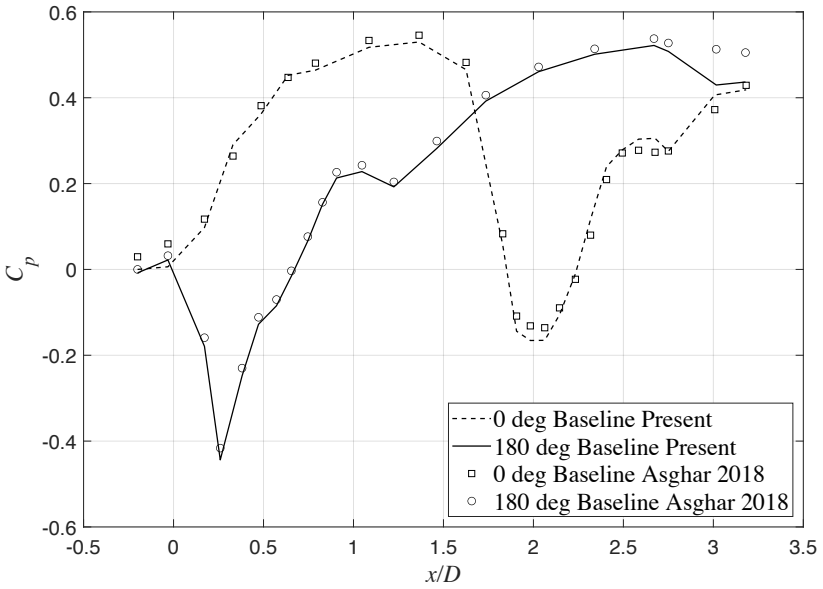

Figure 6.2: Comparison of pressure coefficient for baseline duct, Asghar 2018 [20]

The points along the duct follow the previously measured data closely, but the last two points on the 180° meridian differ. This is because the last two measurements falling in the new measurement duct. Limited access prevented the alignment between the S-duct and measurement duct to be verified in this set up compared to Asghar and his teams set up, some misalignment may have occurred causing a small region of separation after the AIP, behind the probe tip [20]. Figure 6.3 shows the comparison between the FC3 duct with the old and new measurement equipment.

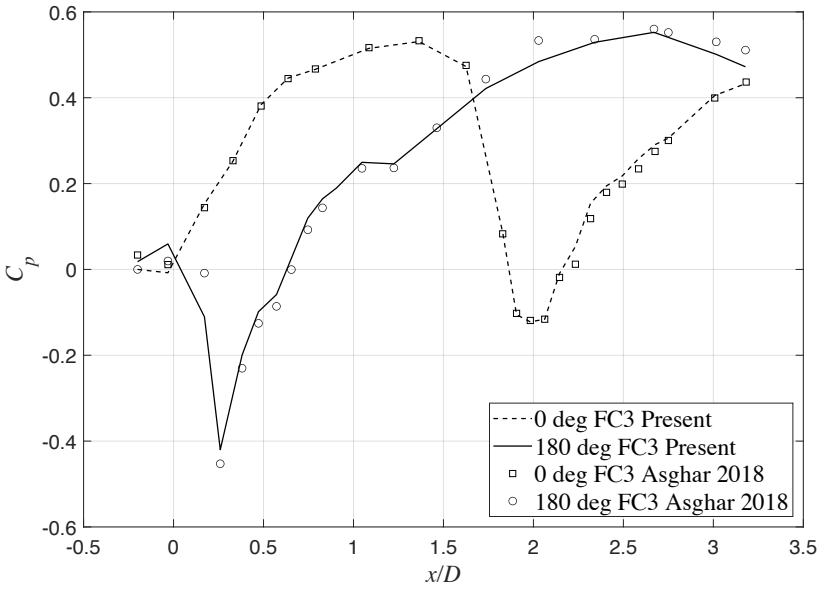

Figure 6.3: Static pressure at 0° and 180° meridian for FC3 duct, Asghar 2018 [20]

Similarly to the baseline duct, the current experimental work matches the 2018 work performed by Asghar *et al.* [20]. The two methods of validation prove that the same S-ducts will deliver very comparable results while using the new equipment.

6.1.2 Current Experimental Work

This section compares the current work to previous work by Asghar *et al.* in 2018 between the baseline and flow control ducts [20]. Figure 6.4 presents the FC3 results, the last successful FC design, to later be compared with the new FC4 design.

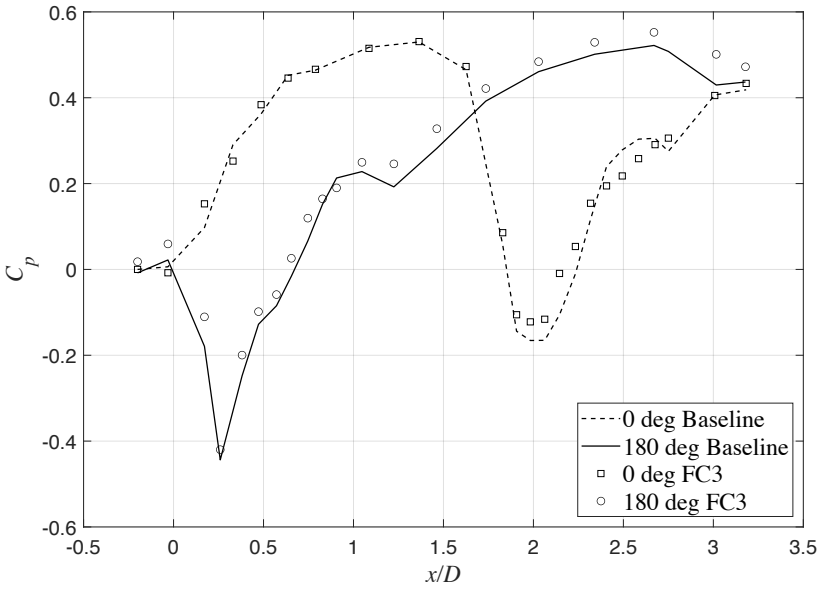

Figure 6.4: FC3 and baseline duct static pressure coefficient

Before the regions of separation, there are minimal differences in the two S-ducts. As the first inner radius, 180° and $x/D = 0.9$ and $x/D = 1.1$, the data shows a region of separation in both the baseline and FC3 duct, respectively. The separation is visualized by an approximately constant value of static pressure coefficient or a change in C_p trend without the presence of an inner or outer bend. At the second inner radius, at 0° and $x/D = 2.5$, the baseline duct separates while the FC3 duct is able to almost entirely remove the separation. The clear separation in the baseline duct is reduced with a subtle inflection of C_p in the flow control duct, FC3. Figure 6.5 shows the flow control comparison for the FC4 duct.

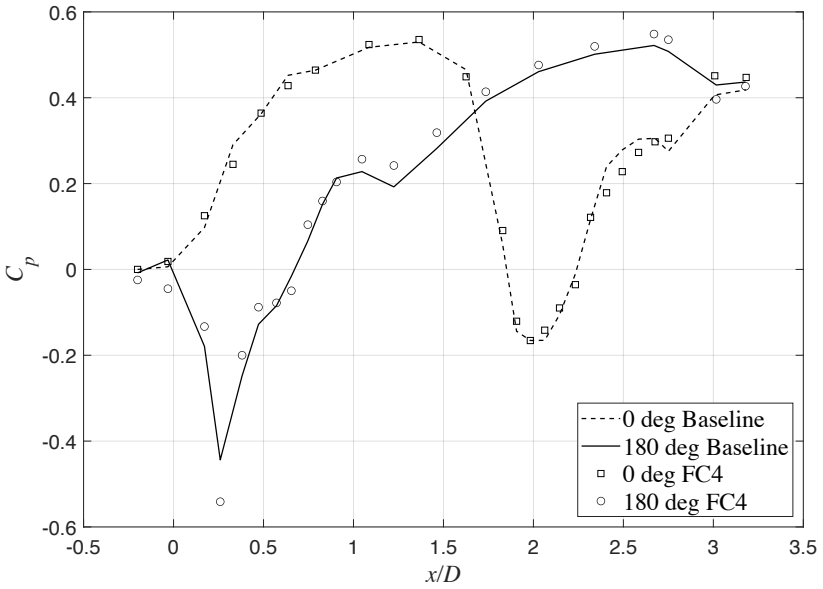

Figure 6.5: FC4 and baseline duct static pressure coefficient

Similar trends are seen in the comparison of FC4 to the baseline duct. The FC4 duct is also able to remove separation at the 180° and $x/D = 2.5$ region. These results demonstrate that both flow control ducts promise the abilities to reduce the severity of secondary flow and subsequent distortion at the AIP.

6.2 Total Pressure Ratio

The total pressure at the AIP is presented using a contour plot for each duct. The methods described in Chapter 4 were employed to measure the static and total pressure at the AIP to determine the total pressure ratio. The baseline duct total pressure ratio is shown in Fig. 6.7, where 180° is downstream of the first inner radius and 0° is downstream of the second inner radius. The second inner radius is closer to the AIP and therefore its influence on the

flow does not have time to dissipate, leaving a more concentrated region of pressure deficit. Figure 6.6 is presented once for understanding of the contour plot orientation.

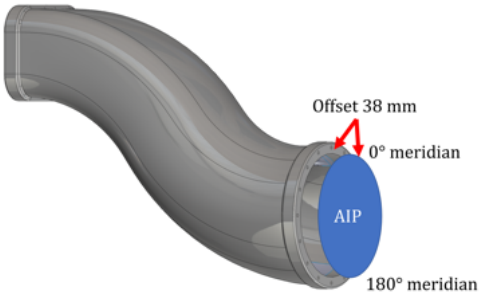

Figure 6.6: 3-dimensional view showing the AIP orientation on the S-duct

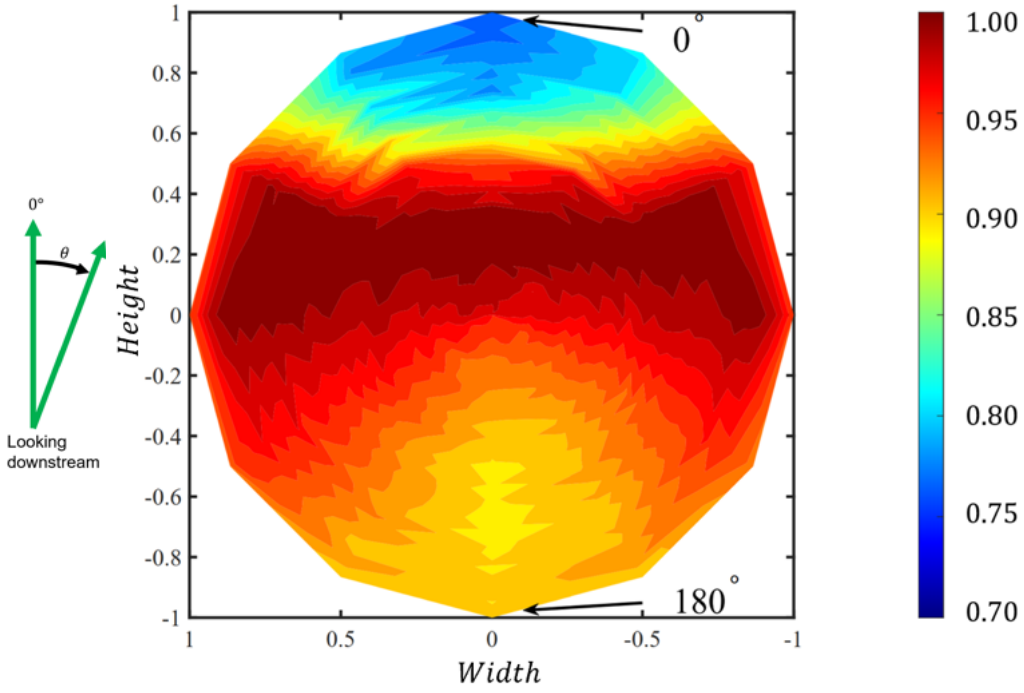

Figure 6.7: Total pressure ratio at the AIP for the baseline duct

The region of the duct, $height = 0$ to $height = 0.5$, has a total pressure ratio of around unity, meaning this area of the AIP achieves full pressure recovery. Along the walls there is reduced pressure from the boundary layer that is forming along the duct. Total pressure deficits near the 0° and 180° wall-regions bear evidence that there are areas of separation along the duct, as seen in the static pressure coefficient plots, when the flow fails to remain attached to the inner radii of the bends. The 180° region shows a total pressure ratio around 0.9, significantly higher than the 0.75 at the 0° locality. This is due to the first inner radius, at the 180° mark, having a longer axial distance and therefore more time for the low energy flow to diffuse into the free-stream. The second inner radius, at the 0° region, has a shorter axial distance to the AIP and the free-stream flow near this region is less affected. The low energy flow is concentrated closer to that wall. It is important to note that the AIP is located where the compressor face would be so total pressure distortion adversely affects the compressor performance and increases cyclic loading. The total pressure ratio, generating force on the compressor blades, spans from unity to 0.7 to almost unity and back down to 0.9 over only a single revolution. Similar trends are found in the flow control ducts. Figure 6.8 and 6.9 show the total pressure ratio for the FC3 and FC4 ducts respectively.

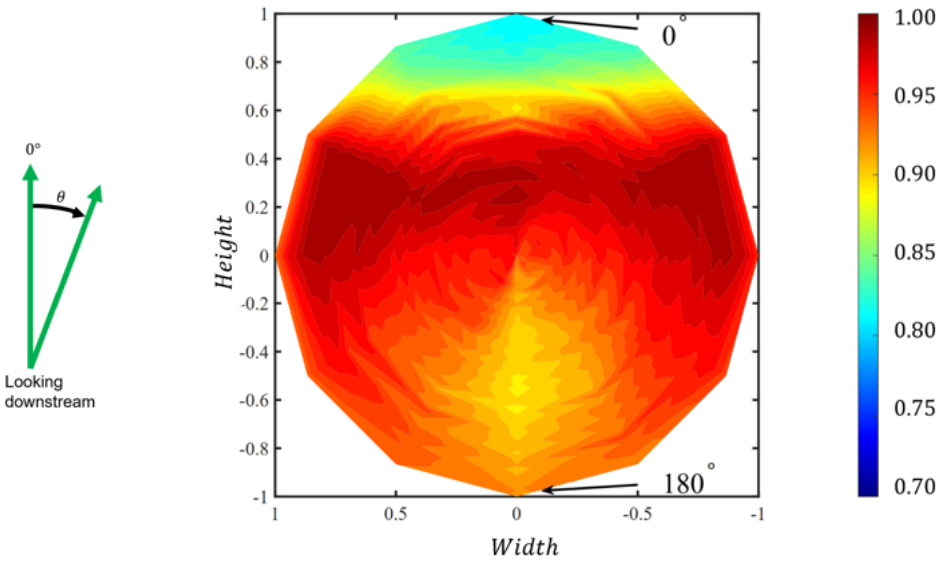

Figure 6.8: Total pressure ratio at the AIP for the FC3 duct

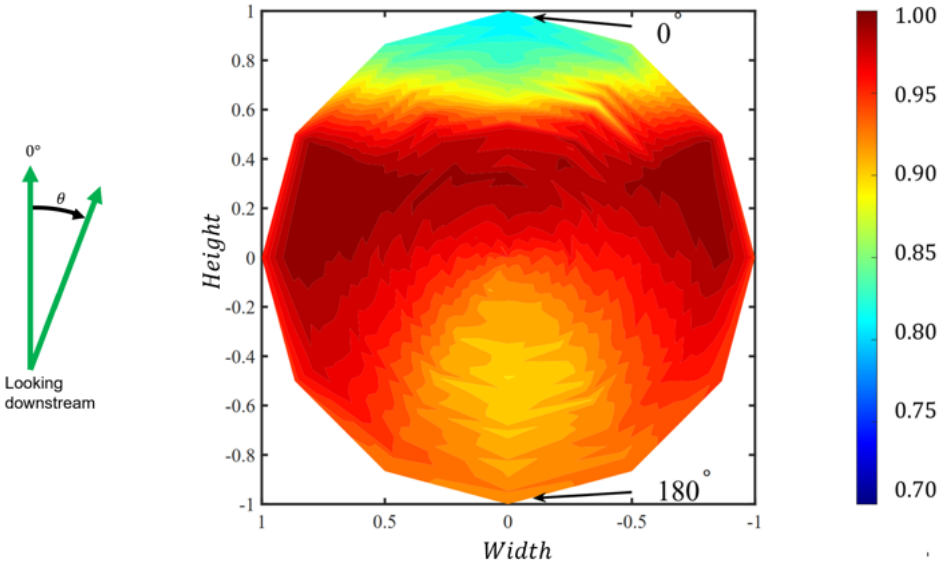

Figure 6.9: Total pressure ratio at the AIP for the FC4 duct

Note the general trends of low pressure near the 0° and 180° portions of the ducts, as previously seen in the baseline duct. The FC ducts have higher total pressure ratio at the AIP near the 0° and 180° localities. The 0° area of the FC4 duct shows similar results to FC3, this is consistent with the static C_p plots in Fig. 6.4 as the similarity in the second region of separation. Note that the low total pressure recovery the 180° portion is higher than that for the FC3 plot. Difference plots between the baseline duct and flow control are useful showing the comparison between ducts.

6.2.1 Comparison in Total Pressure

The total pressure in each duct is more easily compared by taking the difference between the flow control ducts and baseline S-duct. Figure 6.10 shows the total pressure difference between the baseline and FC3 duct. The positive values reveal a higher total pressure in the FC3 and negative values show higher total pressure in the baseline duct.

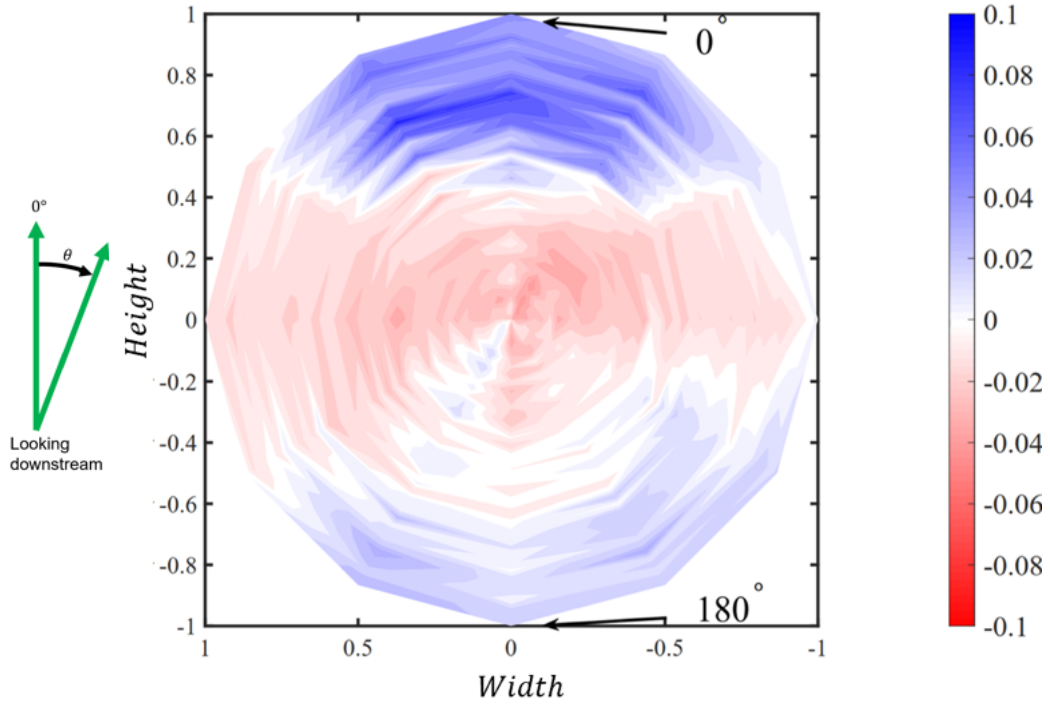

Figure 6.10: AIP total pressure ratio: FC3 minus baseline

Figure 6.10, with its blue dominance in colour, shows that on average the flow control duct has a higher total pressure recovery than the baseline S-duct. The bulk of the flow, at the centre of the duct, is at a slightly lower total pressure in FC3, $\Delta\pi \approx -0.2$. However there are greater improvements near the 0° and 180° portions of the duct. If there are regions of separation, it blocks the flow in the duct causing more of the fluid to accelerates towards the center region presenting as a higher total pressure. Removing or reducing this blockage will enhance mixing of the core flow with the loss region. This justifies the implementation of flow control since it has the ability to improve AIP conditions. Figure 6.11 shows the total pressure comparison, with an even more compelling indication of improved total pressure recovery in the

flow control duct FC4.

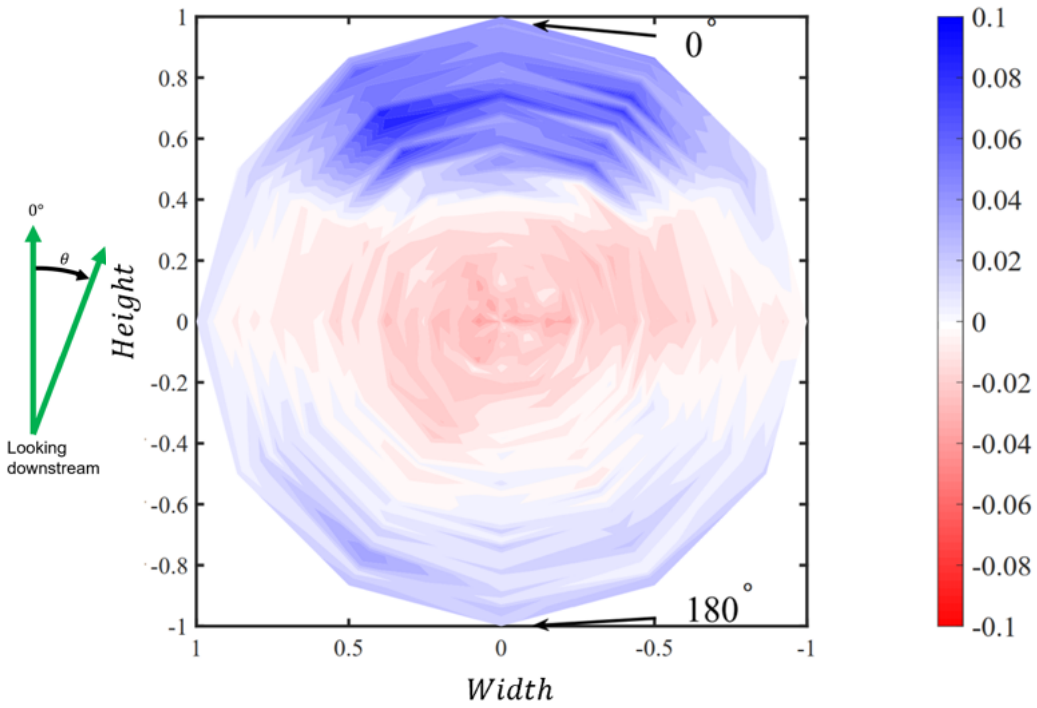

Figure 6.11: AIP total pressure ratio: FC4 minus baseline

Here the flow control has a generally higher total pressure recovery when compared to the baseline S-duct. There is general improvements compared to the baseline duct with higher pressure recovery at the 0° and 180° areas. The evidence of separation seen in the C_p plots is reduced with implementation of FC4, decreasing the losses in the duct. FC3 and FC4 total pressure ratios are compared in Fig. 6.12. Here, a positive value is when the total pressure of FC4 is relatively higher than that of FC3, and a negative value indicates that FC3 produced a higher total pressure recovery.

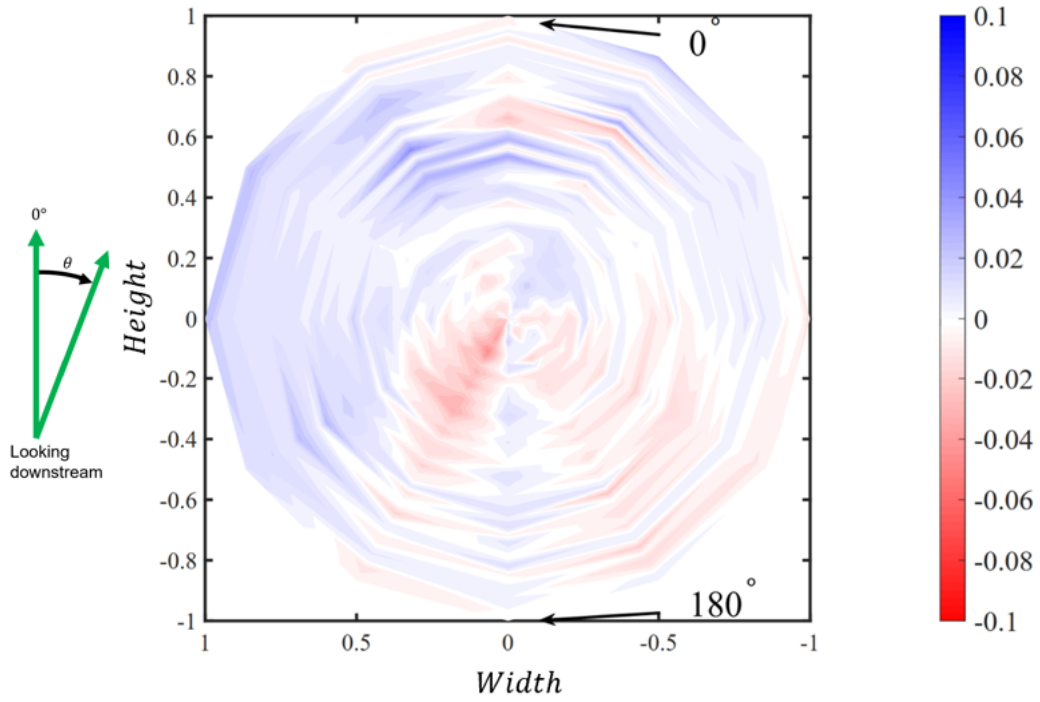

Figure 6.12: AIP total pressure ratio: FC4 minus FC3

In this figure, there is a smaller difference between the two ducts, with slight improvement with FC4, greater than the uncertainty in measurements of 0.0001. The comparison to the baseline revealed a higher pressure for the flow control ducts at both the 0° and 180° areas of the AIP. The comparison between the two flow control ducts themselves shows some difference without a notable trend. This is consistent with their near-identical average total pressure ratios. The AIP area averaged total pressure ratios are shown in Table 6.1. All presented and discussed uncertainty is calculated in Appendix A.

Table 6.1: Average total pressure ratio at the AIP

	$\bar{\pi}$			Uncertainty	
	Value	Δ	Improvement	$\pm$	%
Baseline	0.9340	–	–	0.0001	0.01%
FC3	0.9432	0.0092	✓	0.0001	0.01%
FC4	0.9470	0.0130	✓	0.0001	0.01%

Overall the improvements in total pressure recovery can be seen across the AIP when tubercles are implemented at the inner radii. The FC ducts' ability to reduce separation downstream of the inner radii increases total pressure at both areas of the duct where loss cores had been experienced in the baseline duct. The improvement between FC4 and FC3 is also validated by the total pressure ratios. The new FC4 design is better at diffusing and redirecting inlet air to the engine face, while maintaining the total pressure of the flow.

6.3 Distortion Coefficient

The distortion coefficient compares the worst 60° sector of the AIP for each duct. Since the measurements were performed over 30° sectors, the 60° sector can be rotated at 30° increments using methods described in Chapter 4, Table 6.2 lists the calculate $DC(60)$ coefficients for the three tested ducts.

Table 6.2: Distortion coefficient

	$DC(60)$			Uncertainty	
	Value	Δ	Improvement	$\pm$	%
Baseline	0.4774	–	–	0.0001	0.03%
FC3	0.3516	0.1258	✓	0.0001	0.04%
FC4	0.3736	-0.1038	✓	0.0001	0.04%

The three coefficients calculated occurred at between 300° to 360°, measured clockwise from the 0° position at the top, at the AIP. Both FC ducts

show improvement over the baseline duct, however the FC3 duct has decreased the $DC(60)$ coefficient more. This coefficient is based on the pressure contours in Figs. 6.7, 6.8 and 6.9 for the distortion at 300° to 360° is where the total pressure recovery ranges from 0.75 to unity. This corroborates the placement of the worse 60° sector for all S-ducts rested since the pressure varies most significantly in this section.

6.4 Radial Distortion Coefficient

The radial distortion coefficient uses five annulus, recall that they are equal area as described in detail in Chapter 4, and locates the most distorted annulus. Table 6.3 shows the results for the three experimentally tested ducts.

Table 6.3: Radial distortion

	$DPRP_{\max}$			Uncertainty	
	Value	Δ	Improvement	±	%
Baseline	0.0374	–	–	0.0003	0.75%
FC3	0.0272	-0.0102	✓	0.0003	1.03%
FC4	0.0261	-0.0113	✓	0.0003	1.07%

All the radial distortion maximum sectors are in the outermost annulus, again validated by the range of pressures along this area apparent in Figs. 6.7, 6.8 and 6.9. The implementation of tubercles decreases the radial distortion coefficient since the low pressure regions in the baseline duct are reduced in extent and magnitude for both flow control models. The most uniform average total pressure in these regions is in FC4, which is validated the data in Table 6.3.

6.5 Angular Distortion Coefficient

The angular distortion coefficient takes an area-average of the distortion in each equal area annulus and compares each point to its respective ring. It takes into account the points below the average, helping to depict the range of distortion at the AIP. Table 6.4 displays the angular distortion coefficients for the three tested ducts. The implementation of flow control lowered the average angular distortion, with additional improvement seen in FC4.

Table 6.4: Angular distortion

	$DPCP_{\text{ave}}$			Uncertainty	
	Value	Δ	Improvement	$\pm$	%
Baseline	0.0560	–	–	0.0001	0.18%
FC3	0.0460	-0.0100	✓	0.0001	0.20%
FC4	0.0449	-0.0111	✓	0.0001	0.22%

6.6 Swirl Angle

The swirl angle is evaluated at each point on the AIP, using methods described in Chapter 4, and is plotted for each duct for comparison. Positive swirl is in the clockwise direction and negative swirl is in the counter-clockwise direction when looking downstream. Figure 6.13 shows the swirl angle for the baseline S-duct where there is, on average, a negative bulk swirl.

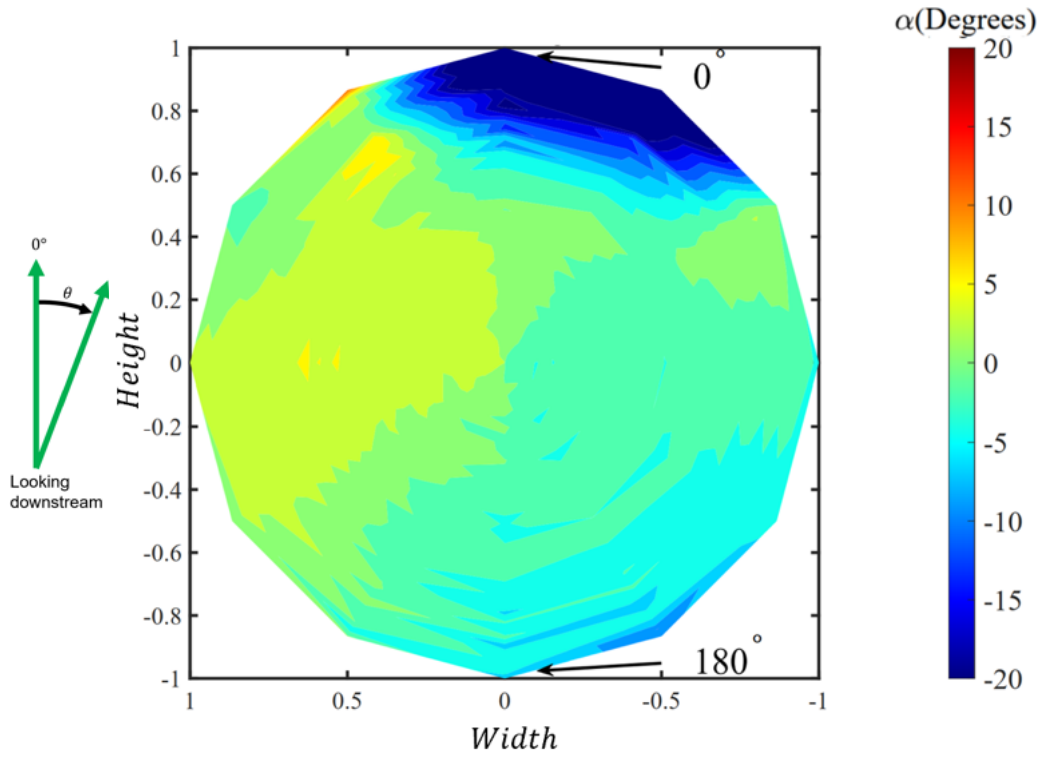

Figure 6.13: Swirl angle at the AIP for the baseline S-duct

The negative bulk swirl is seen through the higher negative angle values and the rotation of symmetry in the negative direction. The test section geometry is symmetric along the 0° to 180° line. Therefore a negative bulk rotation in the α trend plotted at the AIP rotates the symmetry line to the 330° to 150° line. There are two apparent CRV and Fig. 6.14 labels the four regions of interest for discussion.

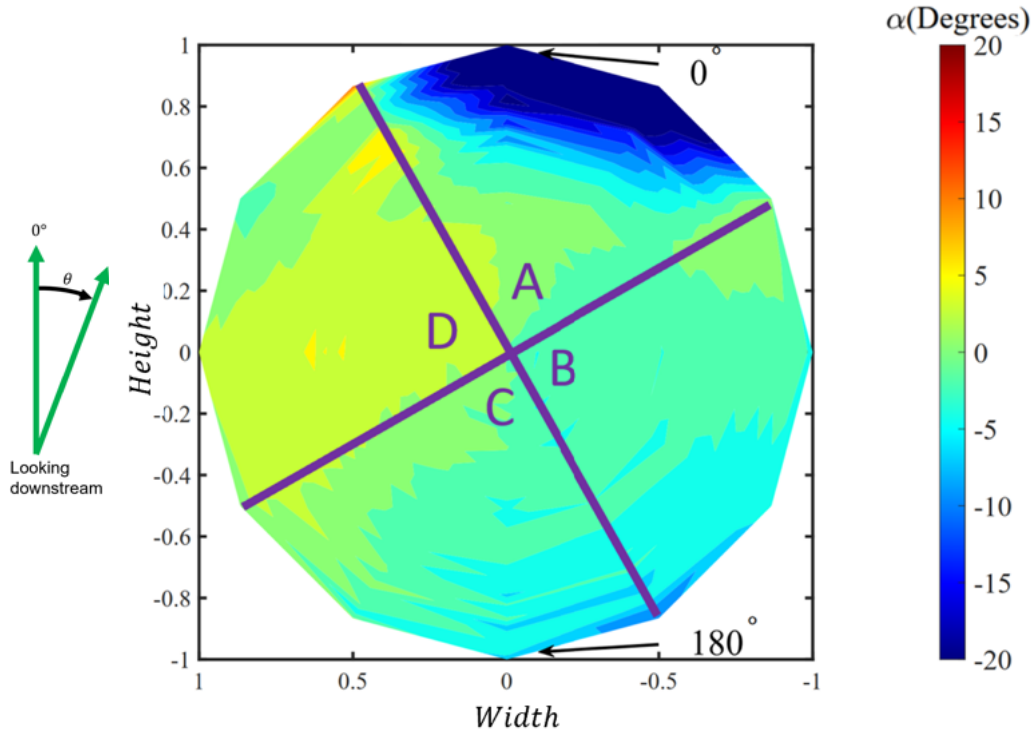

Figure 6.14: Swirl angle at the AIP for the baseline S-duct with annotations

Each sector has a bulk rotation different to its neighbouring quadrant. Sector A and D show the stronger CRV pair generated from the second inner radius, A being negative rotation and D positive. The second CRV pair is in Sectors B and C, with B holding the positive vortex and C the negative. Since this CRV pair evolves from the first inner radius, it has had more time and space to dissipate before reaching the AIP. The positive section in Sector B is noticeable at the top corner of this segment. The negative rotation in Sector C is more prevalent in the bottom right corner, even into Sector B a little. There is a longer axial distance for the first two vortices, in Sectors B and C, to travel, therefore they have been affected by the bulk swirl, presented shortly, to a larger degree. These two vortices are rotated counter-clockwise

since they develop further upstream than the Sectors A and D vortices. This helps to show that the bulk swirl is present throughout the duct and develops early on in the entrance, up to the first bend.

The same trend is present in the swirl distribution for the FC3, Figs. 6.15, and FC4, 6.16, ducts. The difference in the ducts is easier to see in the subsequent comparison plots.

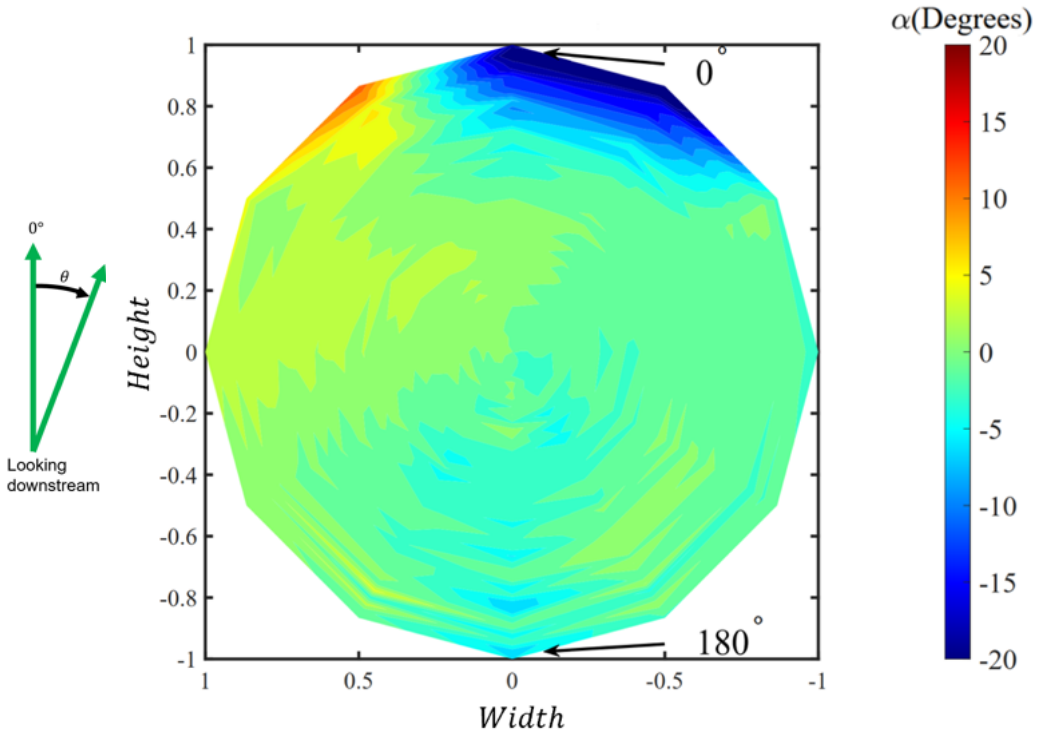

Figure 6.15: Swirl angle at the AIP for the FC3 duct

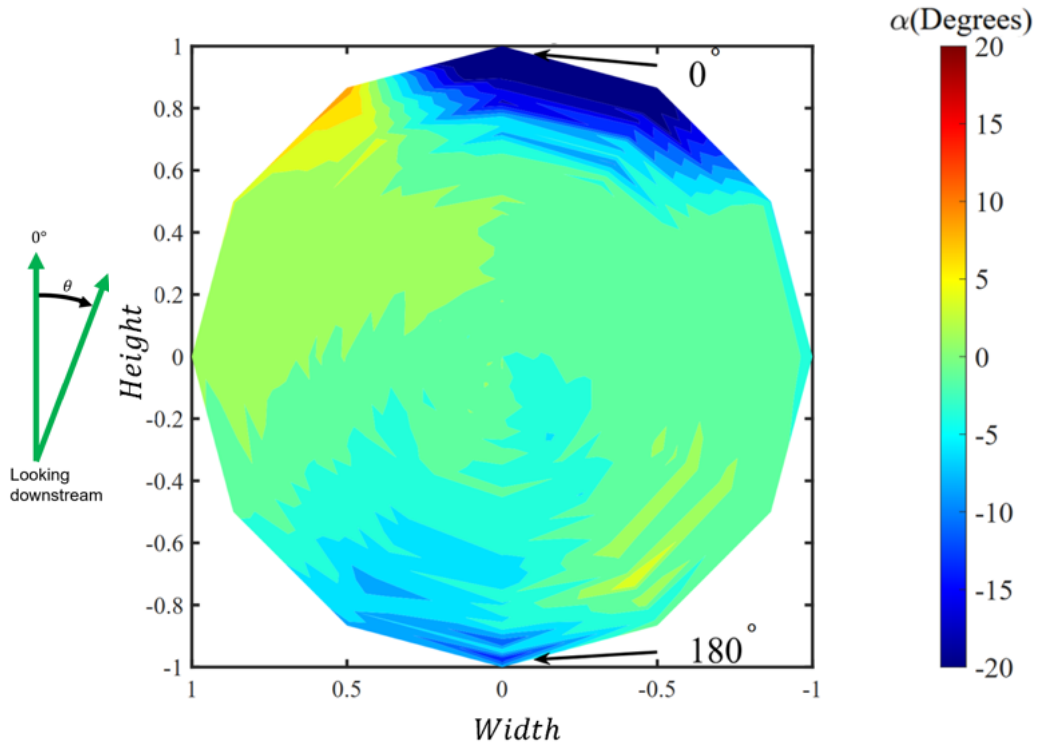

Figure 6.16: Swirl angle at the AIP for the FC4 duct

In the swirl angle polar plots for the FC ducts, the bulk swirl is reduced, most noticeable in the dark blue region at the 0° meridian. In the baseline swirl angle plot, Fig. 6.13, the dark blue, $\alpha = -20$, region extends from roughly from 335° to 50° whereas the FC plots only extend from 345° to 55°. This will be further discussed presently.

6.6.1 Comparison with the Baseline S-Duct

The comparison plots show the baseline duct subtracted from the FC ducts. Figure 6.17 shows the difference between the baseline and FC3 in swirl index.

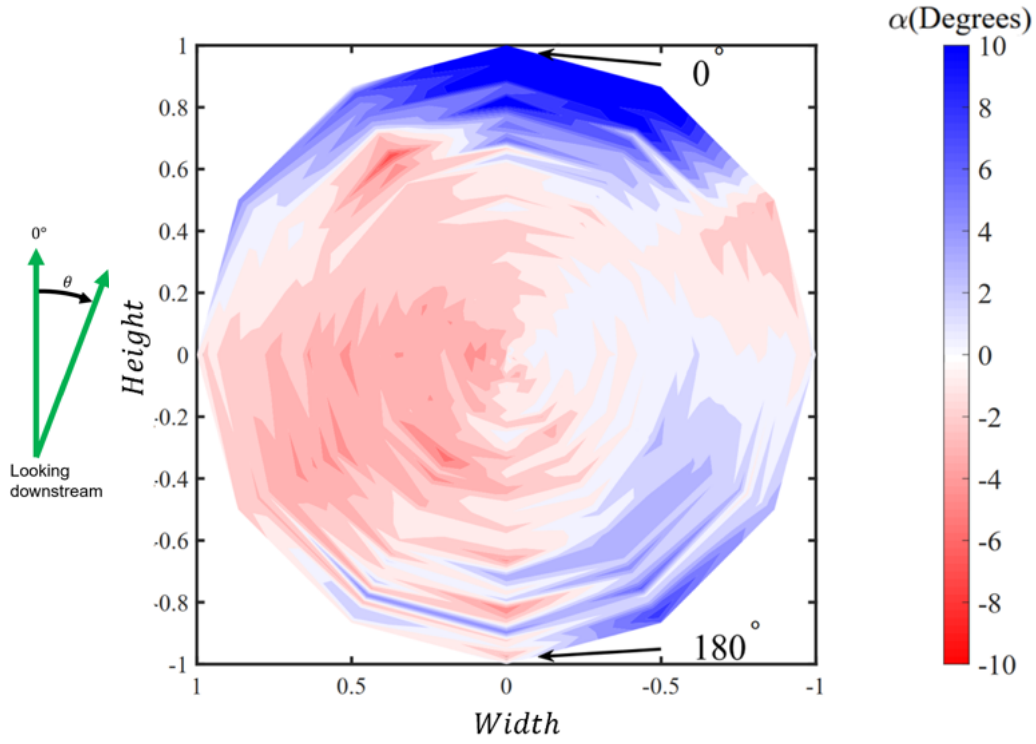

Figure 6.17: AIP swirl angle: FC3 minus baseline

The main trend in the polar plot shows a positive change in swirl, meaning that adding flow control has reduced the bulk swirl. This is emphasized by the maximum in positive values of 10° and minimum values of near -5°, near the 1 and 8 o'clock positions respectively. Using the same quadrants, used in Fig 6.14, the polar plot can be sectioned into four quadrants for discussion, Fig. 6.18.

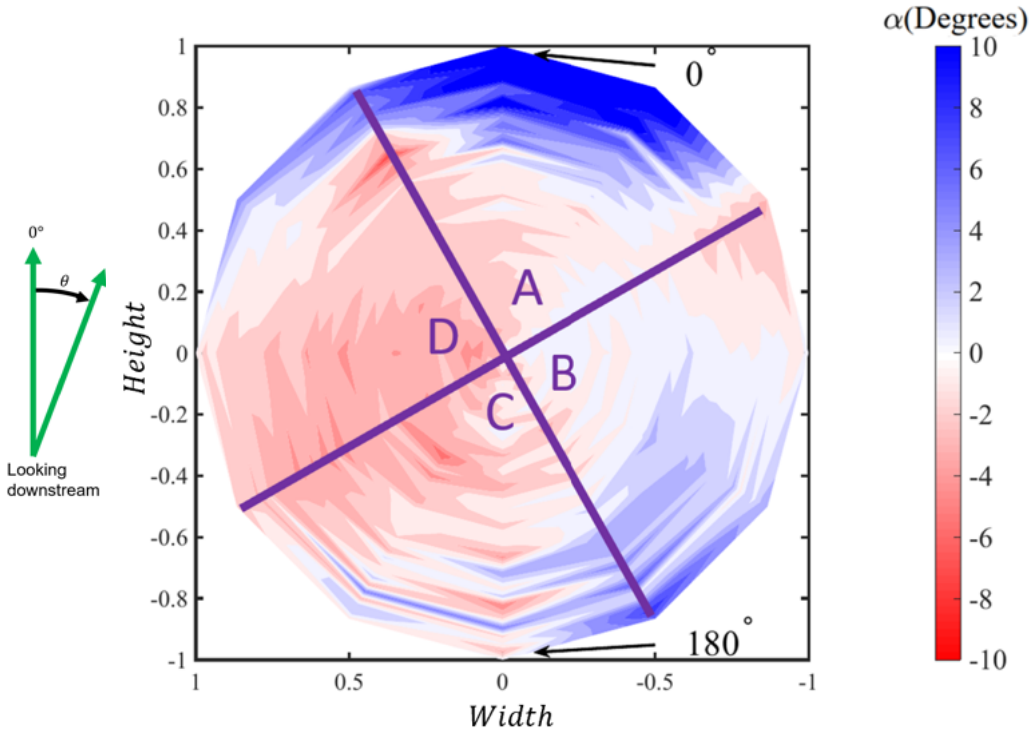

Figure 6.18: AIP swirl angle: FC3 minus baseline with annotated quadrants

Starting with sector A and D, initially all three ducts trended to large negative values of α, as low as -20° as shown in Figs. 6.13, 6.15 and 6.16. The positive value on the swirl angle comparison means that the FC3 duct had a lower magnitude of α, demonstrating an improvement this sector, presented in Fig. 6.18. In Sectors B and D, the negative trend in α values is an improvement, since these quadrants were initially positive, meaning FC3 once again, reduced the magnitude of swirl angle. This improvement on the outer regions in the areas of applied passive flow control shows how the implementation of tubercles on the inner radii can help reduce separation and therefore secondary flows that develop in those areas. The same trends are revealed when comparing the baseline to the FC4 duct in Fig. 6.19.

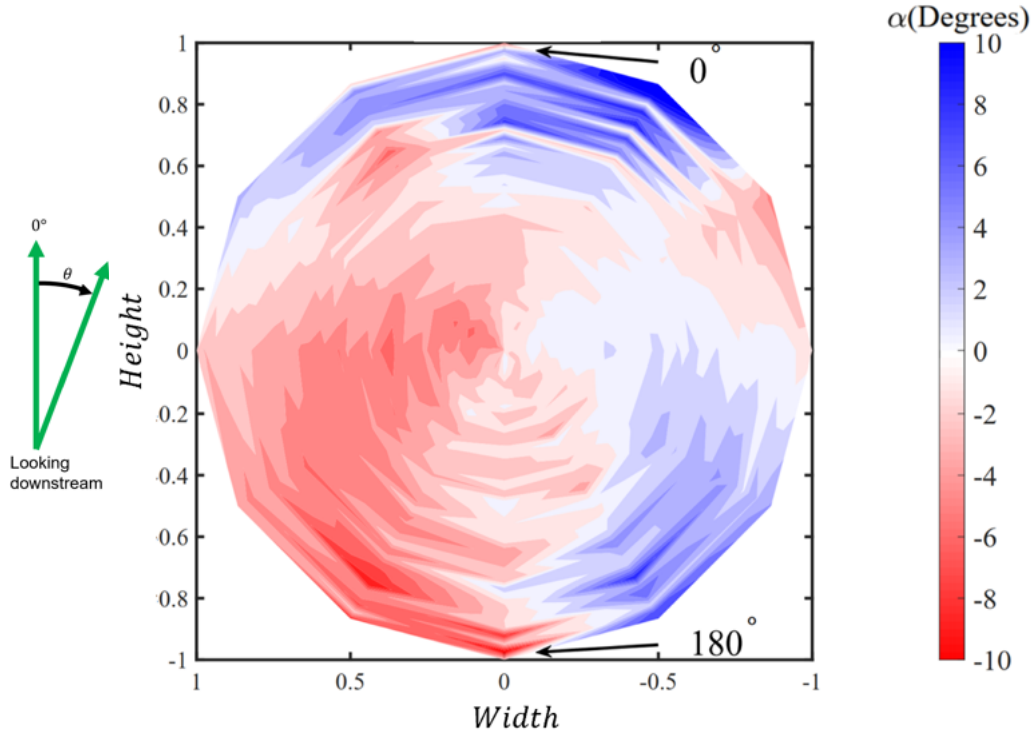

Figure 6.19: AIP swirl angle: FC4 minus baseline

Baseline bulk swirl is not as reduced with FC4 here since there are more areas of increased negative swirl angle visible. Overall, the areas of improvement are equally balanced by deterioration. The FC4 results compare well with the FC3 results, presented in the annotated comparison plot: Fig. 6.18. The differences between FC4 and FC3 are best shown in Figure 6.20 which compares FC4 to FC3

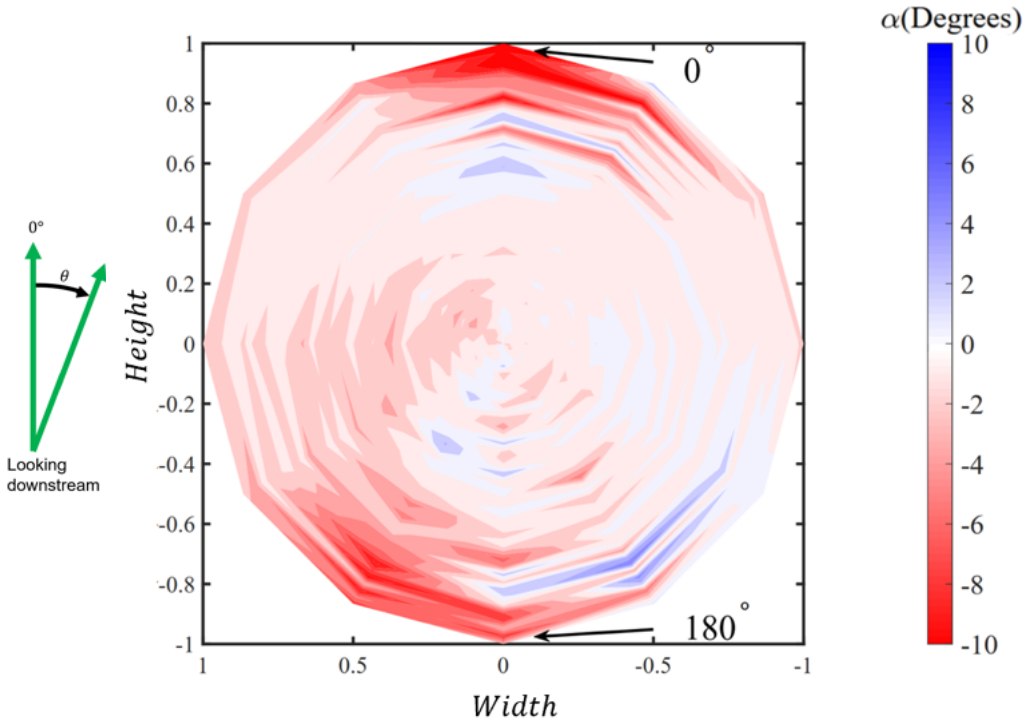

Figure 6.20: AIP swirl angle: FC4 minus FC3

The main noticeable trend is the bulk negative α comparison. In particular, note the highly negative regions at the 0° and 210° locations. These regions initially had negative swirl flow and therefore it is clear that the FC3 duct was able to reduce the magnitude of swirl angle in these regions to a greater extent then the FC4 duct could. The bulk swirl angles are presented in Table 6.5.

Table 6.5: Average bulk swirl angle

	$\overline{\alpha}$			Uncertainty	
	Value	Δ	Improvement	$\pm$	%
Baseline	-1.42	–	–	0.01	0.80%
FC3	-0.61	0.81	✓	0.01	1.87%
FC4	-1.66	-0.24	X	0.01	0.69%

The bulk swirl angle is reduced in FC3 however, it was increased for FC4. The bulk swirl that is seen in the experimental work could develop from the Coriolis effect, supported by the observations that for the Northern Hemisphere it has the correct rotation. However, the large amounts of bulk swirl would need to develop quickly within the duct. The bulk swirl could initiate from the direction of flow entering the room, the duct was rotated to different locations and no difference was found. This rotation could have been induced from proximity to the floor, again no difference was noted when the distance was increased, above 10 diameters from any obstacle. The swirl angle is quantified in coefficients to help compare results between ducts. Flow angle trends using the swirl angle help to develop three coefficients: swirl index, direcivity and pairs.

6.7 Swirl Metric Coefficients

The three swirl metric coefficients were described in detail in Section 6.6. Swirl index depicts the bulk swirl in the flow by taking an area average of the magnitude of swirl angle at the AIP. Table 6.6 presents the swirl index coefficients for all three experimental ducts.

Table 6.6: Swirl index

	SI			Uncertainty	
	Value	Δ	Improvement	$\pm$	%
Baseline	4.56	–	–	0.01	0.25%
FC3	3.20	-1.36	✓	0.01	0.36%
FC4	3.69	-0.87	✓	0.01	0.31%

The swirl index decreased with the implementation of flow control, corroborating the evidence presented in the swirl angle plots. Even if the swirl angle was symmetric at the AIP, the swirl index would not be zero since it averages the magnitude of results. The higher swirl index for the baseline duct reveals that there are more points measured at higher $|\alpha|$ than in the FC ducts.

The swirl directivity coefficient depicts bulk flow in the duct and was fully described in Section 6.6. It compares the area-averaged swirl angle normalized with the averaged magnitude of swirl angle. Table 6.7 shows the relative bulk swirl to swirl angle coefficients.

Table 6.7: Swirl directivity

	SD			Uncertainty	
	Value	Δ	Improvement	$\pm$	%
Baseline	-0.310	–	–	0.004	1.16%
FC3	-0.200	0.110	✓	0.005	2.56%
FC4	-0.449	-0.139	X	0.005	1.02%

A negative bulk swirl was measured in all three ducts. The FC3 duct has a lower bulk swirl-to-swirl index ratio than the baseline, however FC4 does not show this improvement. FC3 was able to reduce the bulk swirl, as seen in the polar comparison of Fig. 6.20. SD compares bulk swirl-to-swirl index ratio and since the FC4 SI was lower than the baseline, the relative values must be acknowledged. More of the flow angle in FC4 is from bulk swirl, however the total swirl index was reduced. The swirl pairs (SP) coefficient

depicts the CRV intensity at the AIP, based on Equation 4.11. The values and uncertainties for the three ducts are shown in Table 6.8.

Table 6.8: Swirl pair coefficient

	SP			Uncertainty	
	Value	Δ	Improvement	$\pm$	%
Baseline	0.8612	–	–	0.0004	0.04%
FC3	1.1083	0.2471	X	0.0007	0.07%
FC4	0.9618	0.1006	X	0.0005	0.05%

The swirl pairs compares the swirl index to the bulk negative or positive averaged swirl angle. Therefore, since there is a negative bulk swirl for all three ducts, α_- is the chosen parameter used in the calculation. The FC ducts have a larger magnitude of swirl-to-negative swirl, meaning the bulk swirl is reduced, as discussed previously. This also means that the secondary flows at the AIP are stronger CRV; again this was shown in the polar plots Figs. 6.17 and 6.19.

6.8 Discussion

The FC4, as seen in Fig. 6.9, had more uniform total pressure since it was able to increase the total pressure recovery in both the 0° and 180° meridian regions. Adding in passive flow control to induce stream-wise CRVs helps to mix the free-stream high-momentum flow with the low-momentum boundary layer flow. The higher momentum near the walls after the CRV develop, help to keep the flow attached and therefore the losses occurring from separation reduce. The reduction in losses is displayed at the AIP though an increase in total pressure as seen in both FC ducts. The FC4 duct showed improvement overall compared to the FC3 duct for the pressure based distortion parameters.

7 Computational Results and Discussion

The computational study was run for 15000 iterations. Results presented are compared to the experimental work to determine if the modeling technique was able to replicate the trends found. Initial static pressure surface plots are compared. Then, the total pressure ratio plots, flow quality coefficients and swirl angle plots are assessed against experiments.

7.1 Static Pressure Coefficient

The static pressure along the meridian of the S-duct was exported from *ANSYS Fluent* as a csv to *MatLab* for plotting. The C_p values were taken at the same port locations from the experimental work. Figure 7.1 shows the static pressure coefficient for the baseline CFD and experimental (Exp.) results.

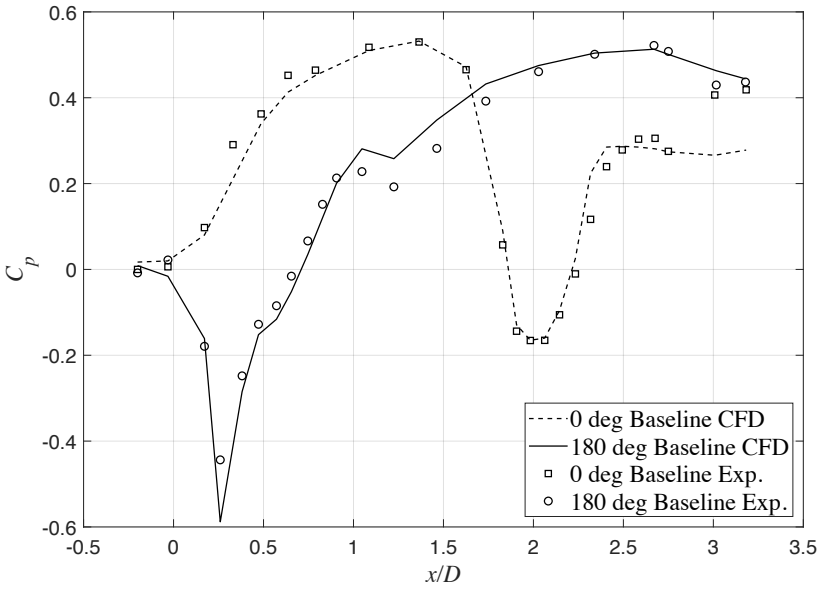

Figure 7.1: Baseline numerical and experimental static pressure coefficient

The C_p calculated for both the CFD and experimental work follow similar trends along the length of the duct. The two regions of separation noted in the experimental work occurred at the first inner radius at 180° near $x/D = 1$, and the second inner radius at 0° near $x/D = 2.5$. In the computational results, at the first inner radius the CFD predicts the separation region later than in experimental work, at an x/D after unity as opposed to slightly before. The second separation region occurs somewhat earlier in the CFD and the flow does not appear to reattach before the AIP. The 180° meridian better matches the experimental results, with notable success near the AIP where static pressure matches closely. This is corroborated with the axial velocity contour along the mid-line plane in Figure 7.2. This figure depicts an extended region of reversing flow along the 0° meridian at the AIP. The top of the velocity scale is at Mach 1 and the bottom is at Mach 0.25 of reversing flow.

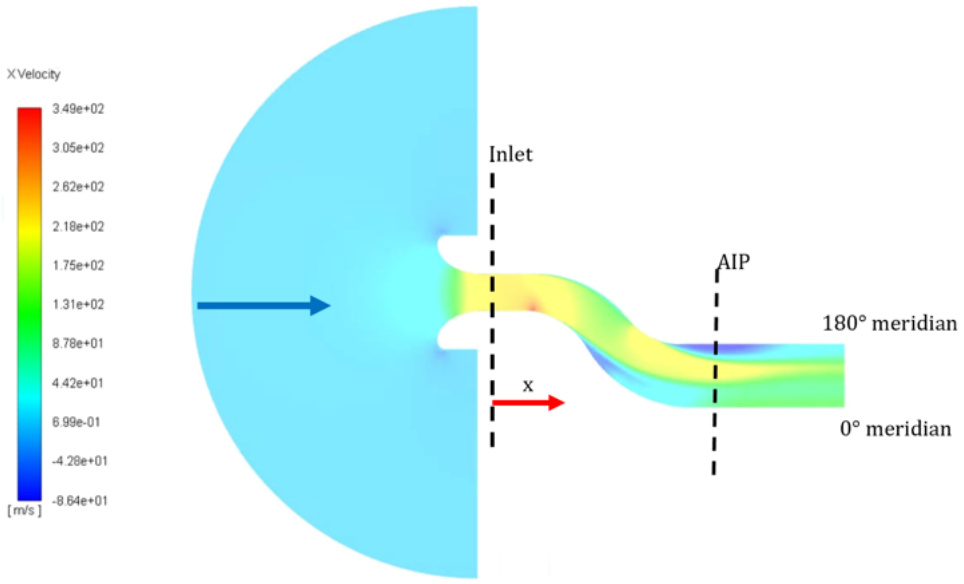

Figure 7.2: Axial velocity along the mid-line plane for the baseline S-duct

7.2 Total Pressure Ratio

The average total pressure ratio at the AIP is plotted in Figure 7.3 looking downstream in the S-ducts as described in Section 4.4.

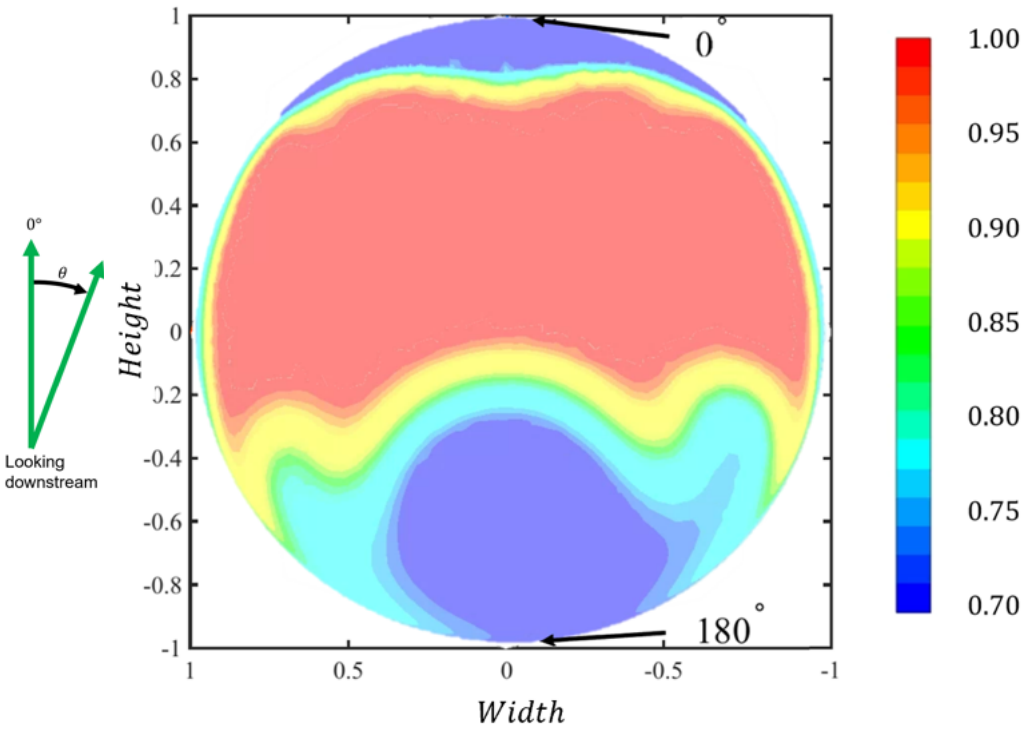

Figure 7.3: Numerical results of baseline total pressure ratio at the AIP

The trends in polar plots show similar results to the experimental work. It is important to note the asymmetry here, this feature was not considered in previous work as it was assumed the geometric symmetry would produce symmetrical flow. Due to asymmetries observed experimentally, the full S-duct was modeled, and the asymmetry was captured. There are two low pressure regions, one at 0° and the other at 180°. The larger region is located at the 180° position, downstream from the diffusion of the first inner radius. The smaller pressure deficit is located in the 0° area, downstream of the more proximate second inner radius. The value of total pressure ratio in the lower pressure regions is smaller than that observed in the experimental

work Fig. 6.7. Referring back to the coefficient of static pressure plot, Fig. 7.1, the lower C_p at the 0° and $x/D = 3.2$ region is confirmation that the flow here separated at the second inner radius and never re-attached. The same trend is seen in the average total pressure ratio $\bar{\pi}$ presented in Table 7.1.

Table 7.1: Computational and experimental average total pressure ratio at the AIP

	$\bar{\pi}$	
	CFD	Experimental
Baseline	0.8435	0.9340

The lower value for CFD average total pressure ratio, compared to experimental work agrees with the more extensive separation seen in the static pressure results and large low total pressure ratio regions of the AIP plots.

7.3 Distortion Coefficient

The pressure distortion at the AIP, described in Section 6.3, is shown in Table 7.2. The computational distortion coefficient over predicts the $DC(60)$ by 19%.

Table 7.2: Computational and experimental distortion coefficient

	$DC(60)$	
	CFD	Experimental
Baseline	0.5670	0.4774

The separation, and therefore total pressure loss is more extensive in the CFD and therefore the pressure varies more across the AIP. This shows up in the pressure based distortion coefficients as a higher distortion.

7.4 Radial Distortion Coefficient

The radial distortion coefficient at the AIP, described in Section 6.4, is shown in Table 7.3. The computational results over predicts radial distortion coefficient by 89% over the experimental work. $DPRP_{\max}$ reports the maximum region of radial distortion and with the lower regions of pressure at the 0° and 180°, the pressure variation at the outermost ring is larger than that observed in the experimental work.

Table 7.3: Computational and experimental radial distortion

	$DPRP_{\max}$	
	CFD	Experimental
Baseline	0.0708	0.0374

This reflects the ring with the worst pressure differences in the AIP. Since the second inner radius does not reattach in the CFD work, the $DPRP_{\max}$ shows a higher variation in total pressure. In both the experimental and numerical work, the outer ring has the worst radial distortion section of the AIP.

7.5 Angular Distortion Coefficient

The angular distortion coefficient at the AIP, described in Section 6.5, is shown in Table 7.4. Similar to the radial distortion coefficient, the computational work over-predicts the angular distortion coefficient with a difference of 220% over the experimental data. $DPCP_{\text{ave}}$ only accounts for values below the average. Since the pressure variation in the CFD results is greater then experimental variation (as CFD cannot capture the flow reattachment at the

second inner radius) the predicted distortion coefficients are thus higher than the real value.

Table 7.4: Computational and experimental angular distortion

	$DPCP_{\text{ave}}$	
	CFD	Experimental
Baseline	0.1785	0.0560

7.6 Swirl Angle

Using techniques described in Section 4.4.6 the CFD swirl angle, α, depicts the distribution at the AIP for the baseline duct, shown in Figure 7.4.

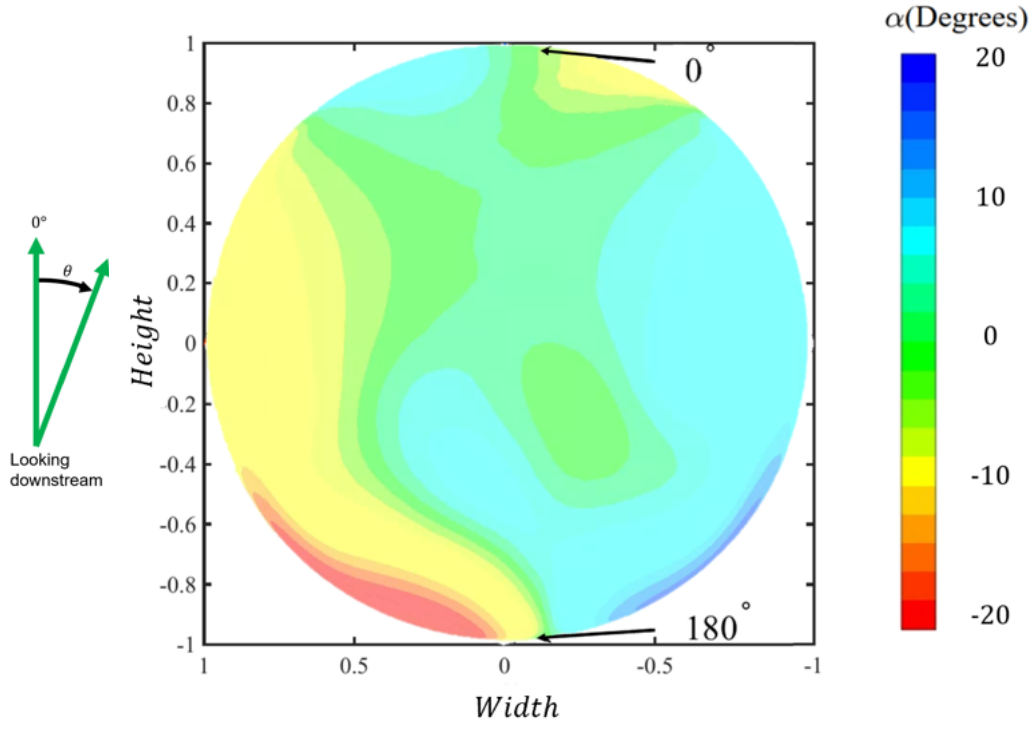

Figure 7.4: Computationally determined flow angle for the baseline S-duct at the AIP

The trends in the contours plot of α is similar to that of the experimental work as there are four quadrants. However, the CFD predicts a reduced amount of bulk swirl, as shown in Fig. 7.5.

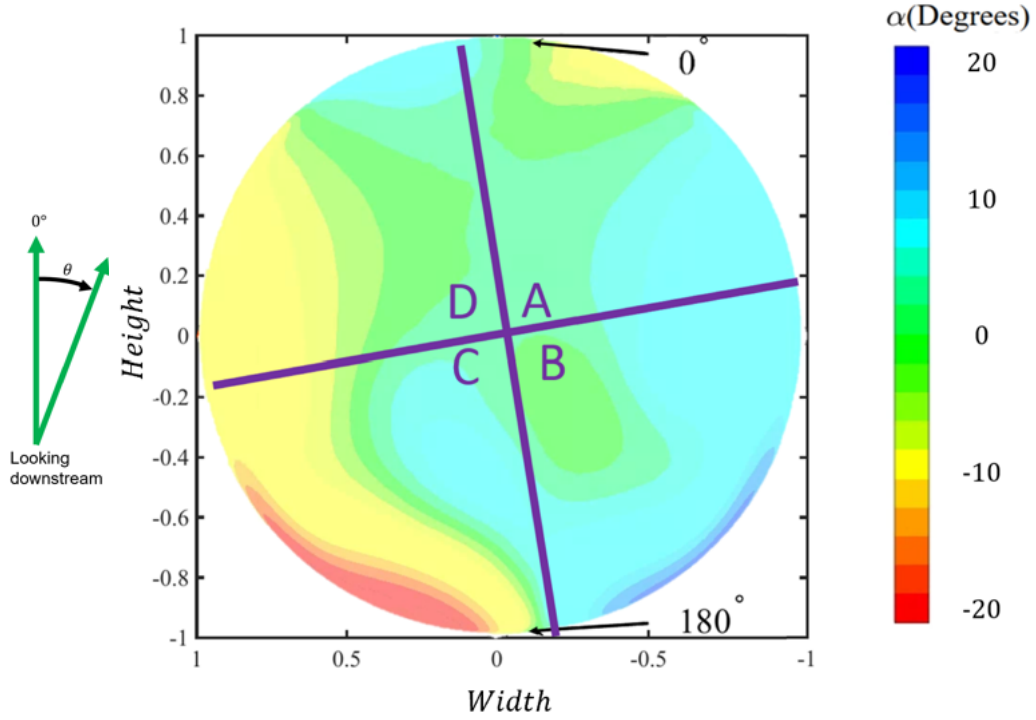

Figure 7.5: Annotated computationally determined flow angle for the baseline S-duct at the AIP

The swirl angle present in the CFD results showed similar trends in the four quadrants of rotational flow. The higher flow angles are located at the 180° meridian region of the duct, contrary to experimental work at 0°. The macro trend of negative bulk swirl is consistent with experimental observations. The bulk swirl present in the contour plots, is qualified in Table 7.5.

Table 7.5: Computational and experimental comparison of bulk swirl angle

	$\overline{\alpha}$	
	CFD [°]	Experimental [°]
Baseline	-0.48	-1.42

The numerical work is able to replicate the bulk swirl in the duct. This is significant since S-ducts were mistakenly assumed to be symmetric in previous work and a full duct simulation with a perfectly symmetrical duct shows that flow asymmetry does occur.

7.7 Swirl Metric Coefficients

The other swirl metric coefficients, described in Section 6.7, compare well to the experimental work. For example, this can be seen in Table 7.6 where the swirl index values differs by 5%. However, as noted in the swirl angle contour plots, the distribution of α differs in the CFD results.

Table 7.6: Computational and experimental swirl index

	SI	
	CFD [°]	Experimental [°]
Baseline	4.79	4.56

The swirl directivity (SD), describing the bulk rotation, Table 7.7, differing from experimental work by 36%.

Table 7.7: Computational and experimental swirl directivity

	SD	
	CFD	Experimental
Baseline	-0.199	-0.310

The computational predictions of swirl pair coefficient, SP, again displays similar results to experimental findings. Table 7.8 presents reasonably

matched SP for the numerical and experimental work, differing by just 10%.

Table 7.8: Computational and experimental swirl pair coefficient

	SP	
	CFD	Experimental
Baseline	0.9458	0.8612

The computational study has shown the separation starts earlier, and takes a longer axial distance to recover in the computational work leading to an over prediction of losses and distortion.

7.8 Discussion of Computational Study

This chapter has presented meridian static pressure coefficient, AIP total pressure and flow angle polar plots and coefficients. The static pressure coefficient showed that the numerical work predicted late separation and no recovery on the second inner radius, therefore there is a difference in static pressure coefficient the AIP. Through modeling the full S-duct there was the presence of asymmetry and bulk swirl at the AIP, this was not seen by other authors. In the total pressure recovery plot there were similar trends compared to the experimental work, however magnitudes varied.

Similar to the current work, divergence between the CFD results and experimental work was also seen by other authors: Schneider and Hickling *et al.* [44, 43]. The work performed by Hickling with the Realizable $k-\epsilon$ model did not show the difference in static pressure at the AIP and predicted a smaller extent of separation, therefore under-predicting distortion [43]. In using the realizable $k-\epsilon$ model, Hickling *et al.* were able to match total pressure but they saw smaller differences in distortion coefficients and greater differences in swirl metrics, compared to current work. In this work the separation re-

gion was predicted earlier than experimentally determined. There is an over prediction of losses throughout the duct from larger separation regions and recirculating flow. Improvement in correlating the separation region at the inner radii through modifying the turbulence model could aid in creating a better model. An important piece discovered in this work is the asymmetry and bulk swirl noted in the computational work, further CFD must be done to locate the cause and initiation of this phenomenon. The computational work in the current thesis has created a solid basis for automation of computationally optimized S-duct design.

8 Conclusions

An experimental campaign was conducted at RMC to improve flow conditions in an S-duct inlet through implementation of flow control in the form of tubercles. This was complemented by computational work designing an automation system which takes three tubercle parameters and outputs the mesh for CFD. The numerical campaign was continued by simulating the baseline S-duct to compare with the experimental results. The innovation in this thesis includes the design a tubercle configuration for passive flow control that effectively reduced losses and swirl over a baseline diffusing S-duct designed for Mach 0.8 flight. Secondly, a novel computer automation methodology was developed for the design of future tubercle-based passive flow control for the S-ducts and most importantly, the thesis presents a unique finding of bulk swirl at the duct-engine interface for both experimental and computational observations.

In the current experimental work, a new data acquisition apparatus was used and validated by matching previous experimental work. Measurements of static pressure were taken at the intake, along the meridians and across the AIP of the ducts, while total pressure was only measured at the inlet and AIP. The static pressure coefficients along the S-duct showed two regions of separation for the baseline S-duct, corresponding to both inner radii. A significant finding of this work was that these regions of separation mitigated or elimi-

nated with the implementation of flow control. The reduced separated flow led to higher and more uniformly distributed total pressure at the AIP, leading to lower pressure-based distortion coefficients for the flow control ducts. Two regions of low pressure were apparent at the AIP, located downstream of both inner radii. The flow angle, measured at the AIP, indicated that the reduction of separation also reduced the intensity of rotation. The new flow control duct had similar, but higher values for swirl index, directivity and pairs coefficients compared to the previous flow control duct. Results from all ducts revealed the presence of two pairs of counter rotating vortices and negative bulk swirl when looking downstream. The benefit of more uniform conditions in total pressure is improved compressor performance and reduced cyclic loading on the compressor blades. Furthermore, having a widely varying flow angle can cause rotating stall or even surge of the engine, so it must be designed considering these operational conditions.

The automation system was successful in taking the input of three tubercle key parameters and outputting a mesh that did not need modifications before its implementation into the CFD solver. This can be used in future work to develop an optimization system to numerically model and design an S-duct before its experimental testing. In the numerical study on the baseline, the static pressure coefficient predicted late separation and no reattachment on the second inner radius before the AIP. The static pressure along the duct was comparable to the experimental work overall before the regions of separation. The total pressure compared in trend however, with the low pressure regions lower in magnitude and larger in size than experimental results for those features. The swirl was not as evident in the numerical work from the second inner radius, however the trends from the first inner radius were present. The swirl coefficients were comparable to the experimental work, notably predict-

ing the bulk swirl measured experimentally. In previous studies, the duct was assumed to be geometrically symmetric and only half the duct was modeled. In the current work, the full duct was modeled rendering detection of flow asymmetry possible.

9 Recommendations

In the experimental work, further investigation should be conducted into the presence of the bulk swirl for the baseline S-duct. The influence of inlet Mach number versus bulk swirl would help to describe this flow phenomenon and develop a better understanding of it. Additionally, further work on using a straight diffuser and comparing results and differences to the S-duct may help to develop a better understanding of flow angle formation. Development of passive flow control using tubercles should be continued, with the potential to develop the design properly using CFD before experimental testing.

This work developed a methodology to allow an S-duct design optimization. The continuation of this is recommended, using the input parameters of positive and negative tubercle amplitude and wavelength. Using the constructed automation in *Python*, future work can expand upon this and implement a complete optimization loop. Initially it would be ideal to test this with an optimization of design using a set number of ducts.

Future work should expand the CFD study using DDES to help model three-dimensional flows. It is important to locate the cause of bulk swirl and asymmetry in the flow. The ability to combine this modeling technique with an optimization loop is limited since at present, it is highly computationally intensive. Another potentially more feasible option is to investigate the turbu-

lence parameters in the $k-\omega$ SST or realizable $k-\epsilon$ models to better match S-duct experimental results. Since these are less computationally demanding, they could be better suited for design optimization. The modeling technique chosen will need to be validated by comparing trends over multiple S-ducts before implementation using the proposed automation methodology. The automation of the mesh generation was validated, however future work needs to be done to compare the trend between S-ducts in numerical simulations.

References

[1] "Dassault Falcon 900," 2020. [Online]. Available: https://www.wikiwand.com/en/Dassault_Falcon_900

[2] A. R. Paul, P. Ranjan, V. K. Patel, and A. Jain, "Comparative Studies on Flow Control in Rectangular S-Duct Diffuser Using Submerged-Vortex Generators," *Aerospace Science and Technology*, vol. 28, no. 1, pp. 332–343, 2013. [Online]. Available: https://www.sciencedirect.com/science/article/abs/pii/S127096381200199X

[3] "Flippers Provide Lift, Reduce Drag," 2016 Accessed February 17 2021. [Online]. Available: https://asknature.org/strategy/flippers-provide-lift-reduce-drag/

[4] Z. Wei, T. H. New, and Y. D. Cui, "An Experimental Study on Flow Separation Control of Hydrofoils with Leading-Edge Tubercles at Low Reynolds Numbers," *Ocean Engineering*, vol. 108, pp. 336–349, 2015.

[5] C. Rider, A. Asghar, W. D. E. Allan, G. Ingram, R. Stowe, and R. Pimentel, "Investigation of a Passive Flow Control Device in an S-Duct Inlet at High Subsonic flow," *ASME Turbo Expo 2021: Turbine Technical Conference and Exposition*, no. GT2021-60230, Accepted June 2020.

[6] C. G. Caro, T. J. Pedley, R. C. Schroter, and W. A. Seed, *Mechanics of the Circulation*. Cambridge University Press, 2011, ch. 5: Flow in Pipes, pp. 45–70. [Online]. Available: http://www.bg.ic.ac.uk/research/k.parker/homepage/MechanicsoftheCirculation/Chap_05/_Chapter_05.htm

[7] W. S. Saric, "Gortler Vortices," *Fluid Mechanics*, 1994. [Online]. Available: https://www.annualreviews.org/doi/pdf/10.1146/annurev.fl.26.010194.002115

[8] "Couette Flow 4: Taylor Vortices," 2015 Accessed December 21 2020. [Online]. Available: https://malagabay.wordpress.com/2015/02/01/couette-flow-4-taylor-vortices/

[9] A. Bailes, "The Basic Principles of Duct Design, Part 1," May 2017. [Online]. Available: https://www.energyvanguard.com/blog/basic-principles-duct-design/

[10] A. G. Harouni, "Flow Control of a Boundary Layer Ingesting Serpentine Diffuser Via Blowing and Suction," *Aerospace Science and Technology*, 2014.

[11] P. Martínez-Filgueira, U. Fernandez-Gamiz, E. Zulueta, I. Errasti, and B. Fernandez-Gauna, "Parametric Study of Low-Profile Vortex Generators," *International J. of Hydrogen Energy*, vol. 42, no. 28, pp. 17 700–17 712, 2017.

[12] N. Rostamzadeh, K. L. Hansen, R. M. Kelso, and B. B. Dally, "The Formation Mechanism and Impact of Streamwise Vortices on NACA 0021

Airfoil's Performance with Undulating Leading Edge Modification," *AIP Physics of Fluids*, no. 10.1063/1.4896748, 2014.

[13] A. Furman and C. Breitsamter, "Turbulent and Unsteady Flow Characteristics of Delta Wing Vortex Systems," *Aerospace Science and Technology*, vol. 24, pp. 32–44, 2013.

[14] M. J. Brear, Z. Warfield, J. F. Mangus, S. Branddom, J. D. Paduano, and J. S. Philhower, "Flow Separation within the Engine of an Uninhabited Combat Air Vehicle (UCAV)," *4TH ASME JSME Joint Fluids Engineering Conference*, no. FEDSM2003-45579, 2003.

[15] G. Tanguy, D. G. MacManus, P. K. Zachos, and D. Gil-Prieto, "Passive Flow Control Study in an S-duct Intake Using Stero Particle Image Velocimetry," *AIAA Journal*, vol. 55, no. 6, pp. 1862–1877, 2017.

[16] A. Dropkin, D. Custodio, C. W. Henoch, and H. Johari, "Computation of Flowfield Around an Airfoil with Leading-Edge Protuberances," *AIAA J. of Aircraft*, vol. 49, pp. 1345–1357, 2012.

[17] M. Rowe, "Measurements and Computation of Flow in Pipe Bends," in *J. of Fluid Mechanics*, vol. 43, no. 4, 1970, pp. 771–783.

[18] A. C. Rabe, "Effectiveness of a Serpentine Inlet Duct Flow Control Scheme at Designand Off-Design Simulated Flight Conditions," Ph.D. dissertation, Virginia Polytechnic Institute and State University, Aug. 2003. [Online]. Available: https://pdfs.semanticscholar.org/d89b/f8e7eeb3fffdba8cdb22bfcc068f5eecd8f5.pdf

[19] *Aeroprobe Revolutionary Technology*, Revision a ed., 200 Technology Drive, Christainsburg, VA 24073, United States, Jan. 2018.

[20] A. Asghar, S. Sidhu, W. D. E. Allan, G. Ingram, T. M. Hickling, and R. Stowe, "Investigation of a Passive Flow Control Device in an S-Duct Inlet of a Propulsion System with High Subsonic Flow," in *Proceedings of ASME Turbo Expo 2018: Turbine Technical Conference and Exposition*, no. GT2018-76636, Oslo, Norway, 2018.

[21] S. S. Sidhu, R. E. Perez, W. D. E. Allan, and A. Asghar, "Novel Parameters for the Performance Evaluations of Leading Edge Tubercles on Airfoils," in *American Institute of Aeronautics and Astronautics*, no. AIAA-2020-2691, 2020.

[22] W. R. Dean, "XVI. Note on the Motion of Fluid in a Curved Pipe," *The London, Edinburgh, and Dublin Philosophical Magazine and J.of Science*, vol. 4:20, no. DOI: 10.1080/14786440708564324, pp. 208–223, 1927.

[23] M. D. Bolzon, R. M. Kelso, and M. Arjomandi, "Tubercles and Their Applications," *J.of Aerospace Engineering*, vol. 10, no. 04015013, 2015.

[24] W. G. Steenken, *Aircraft Propulsion Systems Technology and Design*. GE Aircraft Engines, 1989, ch. 6 :Engine Operability, pp. 337–380.

[25] L. Jenkins, S. A. Gorton, and S. Anders, "Flow Control Device Evaluation for an Internal Flow with an Adverse Pressure Gradient," *40th AIAA Aerospace SciencesMeeting and Exhibit*, no. AIAA-2002-0266, 2002.

[26] B. G. Allan, C. S. Yao, and J. C. Lin, "Generator Vanes and Jets on a Flat Plate," *AIAA*, no. AIAA-2002-3160, 2002.

[27] J. B. Parham, M. Fitzgerald, and E. de la Rosa Blanco, "Flow Control for Boundary Layer Ingestion in an S-duct Diffuser," *49th AIAA Aerospace Sciences Meeting including the New Horizons Forum and Aerospace Exposition*, no. AIAA-2011-822, 2011.

[28] J. C. Vaccaro, Y. Elimelech, Y. Chen, O. Sahni, K. E. Jansen, and M. Amitay, "Experimental and Numerical Investigation on Steady Blowing Flow Control within a Compact Inlet Duct," *International J. of Heat and Fluid Flow*, vol. 54, pp. 143–152, 2015.

[29] P. T. Soderman, "Aerodynamic Effects of Leading-Edge Serrations on a Two-Dimensional Airfoil," NASA Ames Research Center, Tech. Rep. NASA TM X-2643, 1972.

[30] P. Watts and F. E. Fish, "The Influence of Passive, Leading Edge Tubercles on Wing Performance," *Proc 12th Internat Symp Unmanned Untethered Submersible Tech.*, 2001, Durham, NH: Autonomous Undersea Systems Institute.

[31] H. Johari, C. Henoch, D. Custodio, and A. Levshin, "Effects of Leading-Edge Protuberances on Airfoil Performance," *AIAA Journal*, vol. 45, no. 11, pp. 2634–2642, Nov. 2007, DOI: 10.25141/1.28497.

[32] D. Custodio, "The Effects of Humpback Whale-like Leading Edge Protuberances on Hydrofoil Performance," Master's thesis, Worcester Polytechnic Institute, 2007.

[33] K. L. Hansen, R. M. Kelso, and B. B. Dally, "Performance Variations of Leading-Edge Tubercles for Distinct Airfoil Profiles," *AIAA Journal*, no. 49, pp. 185–194, 2011.

[34] A. Asghar, W. D. E. Allan, M. LaViolette, and R. Woodason, "Influence of a Novel 3D Leading Edge Geometry on the Aerodynamic Performanc of Low Pressure Turbine Blade Cascade Vanes," in *Proceedings of ASME Turbo Expo 2014: Turbine Technical Conference and Exposition*, no. GT2014-25899, Dusseldorf, Germany, 2014.

[35] A. Asghar, W. D. E. Allan, S. A. Pym, and J. P. Clark, "A Low Reynolds Number Experimental Evaluation of Tubercles on a Low-Pressure Turbine Cascade," in *Proceedings of ASME Turbo Expo 2018: Turbine Technical Conference and Exposition*, no. GT2019-91699, Pheonix, USA, 2019.

[36] M. D. Bolzon, R. M. Kelso, and M. Arjomandi, "Parametric Study of the Effects of a Tubercle's Geometry on Wing Performance Through the Use of the Lifting-Line Theory," *AIAA SciTech Forum*, no. 10.2514/6.2016-0295, 2016.

[37] M. Ibrahim, A. Alsultan, S. Shen, and R. S. Amano, "Advances in Horizontal Axis Wind Turbine Blade Designs: Introduction of Slots and Tubercle," *J. of Energy Resources Technology, ASME*, vol. 137, no. 051205, 2015, dOI: 10.1115/1.4030399.

[38] W. Shi, R. Rosli, M. Atlar, R. Norman, D. Wang, and W. Yang, "Hydrodynamic Performance Evaluation of a Tidal Turbine with Leading-Edge Tubercles," *Ocean Engineering*, vol. 117, no. 0029-8018, pp. 246–253, 2016.

[39] W. Shi, M. Atlar, R. Norman, B. aktas, and S. Turkment, "Numerical Optimization and Experimenal Validation for a Tidal Turbine Blade

with Leading-Edge Tubercles," *Renewable Energy*, vol. 96, no. 0960-1481, pp. 42–55, 2016.

[40] D. Serson, J. R. Meneghini, and S. J. Sherwin, "Direct Numerical Simulations of the Flow around Wings with Spanwise Waviness," *J. Fluid Mec*, vol. 826, no. doi:10.1017/jfm.2017.475, pp. 714–731, 2017.

[41] M. D. Bolzon, R. M. Kelso, and M. Arjomandi, "Performance effects of a single tubercle terminating at a swept wing's tip," *Experimental Thermal and Fluid Science*, vol. 85, pp. 52–68, 2017.

[42] T. Hickling, "Tubercles as Passive Flow Control in Transonic S-Duct Diffusers," Master's thesis, Durham University, Apr. 2018.

[43] T. Hickling and G. Ingram, "Reynolds-Averaged Navier–Stokes Modelling in Transonic S-Ducts with Passive Flow Control," *J.of Power and Energy*, vol. 234, no. 1, pp. 31–45, 2019.

[44] M. Schneider, "Delayed Detached Eddy Simulations and Passive Flow Control in Transonic S-Duct Diffusers," Master's thesis, Durham University, 2019.

[45] A. Vakili, J. M. Wu, P. Liver, and M. K. Bhat, "Measurements of Compressible Secondary Flow in a Circular S-Duct," *AlAA 16th Fluid and Plasma Dynamics Conference*, no. AIAA-83-1739, 1983.

[46] A. M. K. P. Taylor, J. H. Whitelaw, and M. Yianneskis, *Developing Flow in S-Shaped Ducts*, Contract Report 3759, Prepared for Lewis Research Center under Contract NASW-3435 ed., NASA, 1984.

[47] A. Vakili and J. M. Wu, "Comparison of Experimental and Computational Compressible Flow in a S-Duct," *AIAA*, no. AIAA-84-0033, 1984.

[48] S. R. Welborn, B. A. Reichert, and T. H. Okiishi, "An Experimental Investigation of the Flow in a Diffusing S-Duct," *AIAA/SAE/ASME/ASEE 28th Joint Propulsion Conference and Exhibit*, no. AIAA-92-3622, 1992.

[49] J. H. Whitelaw and S. C. M. Yu, "Velocity Measurements in an S-Shaped Diffusing Duct," *Experiments in Fluids*, vol. 15, pp. 364–367, 1992.

[50] G. J. Harloff, J. R. DeBonis, C. F. Smith, and J. E. Bruns, "Three-Dimensional Compressible Turbulent Computations for a Nondiffusing S-Duct," NASA, Tech. Rep. NASA Contractor Report 4391, Prepared for Lewis Research Center under Contract NAS3-25266, 1992.

[51] G. J. Harloff, B. A. Reichert, and S. R. Wellborn, "Navier-Stokes Analysis and Experimental Data Comparison of Compressible Flow in a Diffusing S-Duct," *10th Applied Aerodynamics Conference*, no. AIAA-922699, pp. 719–728, 1992.

[52] B. H. Anderson, "Application of Computational Fluid Dynamics to the Study of Vortex Flow Control for the Managment of Inlet Distortion," *AlAA/ASME/SAE 28th Joint Propulsion Conference and Exhibit*, no. AIAA-92-3177, 1992.

[53] J. H. Whitelaw and S. C. M. Yu, "Turbulent Flow Characteristic in an S-shaped Diffusing Duct," *Flow Measurement Instrumentation*, vol. 4, no. 3, pp. 171–180, 1993.

[54] B. H. Anderson, D. R. Reedy, and K. Kapoor, "Study on Computing Separating Flows Within a Diffusing Inlet S-Duct," *J.of Propulsion and Power*, vol. 5, p. 661, 1994.

[55] M. E. H. Benhamaza, L. Khezzar, and A. J. Marquis, "Flow Characteristics Inside a Diffuser of Complex Shape," *SAGE*, vol. 213, pp. 278–289, 1999.

[56] B. Bouldin and Y. Sheoran, "Inlet Flow Angularity Descriptors Proposed for Use With Gas Turbine Engines," *SAE Technical Paper Series*, no. 2002-01-2919, 2002.

[57] N. C. Bissinger and T. Breuer, *Gas Turbine Compatibility - Intake Aerodynamic Aspects*. John Wiley and Sons Ltd., 2010, ch. EAE487.

[58] A. J. Anabtawi, R. F. Blackwelder, P. B. S. Lissaman, and R. H. Liebeck, "An Experimental Investigation of Boundary Layer Ingestion in a Diffusing S-Duct With and Without Passive Flow Control," *37th AIAA Aerospace Sciences Meeting and Exhibit*, no. AIAA-99-0739, 1999.

[59] J. W. Hamstra, D. N. Miller, and P. P. Truax, "Active Inlet Flow Control Technology Demonstration," *The Aeronautical Journal*, vol. 104, pp. 473–481, 2000, issue 1040.

[60] Y. P. Kohama, "Three-Dimensional Boundary Layer Transition Study," *Institute of Fluid Science*, vol. 79, pp. 800–808, 2000.

[61] A. S. Leuers, "Flow Control Techniques in a Serpentine Inlet: An Enabling Technology to Increase the Military Viability of Unmanned Air Vehicles," Master's thesis, Massachusetts Institute of Technology, 2003.

[62] S. Tournier, "Flow Analysis and Control in a Subsonic Inlet," Master's thesis, Massachusettes Institute of Technology, 2005.

[63] S. E. Tournier and J. D. Paduano, "Flow Analysis and Control in a Transonic Inlet," *23rd AIAA Applied Aerodynamics Conference*, 2003.

[64] S. Nguyen, "Computational Fluid Dynamics Simulations of a Diffusing S-Duct Using Overset Grids," Master's thesis, California State University, Long Beach, CA, USA, 2013.

[65] S. A. Gorton, L. R. Owens, L. N. Jenkins, B. G. Allan, and E. P. Schuster, "Active Flow Control on Boundary Layer Ingesting Inlet," *42nd AIAA Aerospace Sciences Meeting and Exhibit*, vol. 42, no. AIAA 2004-1203, pp. 1–12, 2004.

[66] B. L. Berrier and B. G. Allan, "Experimental and Computational Evaluation of Flush-Mounted, S-Duct Inlets," *42nd AIAA Aerospace Sciences Meeting and Exhibit*, no. AIAA 2004-0764, 2004.

[67] B. L. Berrier, M. B. Carter, and B. G. Allan, "High Reynolds Number Investigation of Flush-Mounted, S-Duct Inlet With Large Amounts of Boundary Layer Ingestion," *NASA*, no. TP-2005-213766, 2005.

[68] B. G. Allan, L. R. Owens, and J. C. Lin, "Optimal Design of Passive Flow Control for a Boundary-Layer-Ingesting Offset Inlet Using Design-of-Experiments," *44th AIAA Aerospace Sciences Meeting and Exhibit*, no. AIAA 2006-1049, 2006.

[69] L. R. Owens, B. G. Allan, and S. A. Gorton, "Boundary-Layer Ingesting Inlet Flow Control," *AIAA J. of Aircraft*, vol. 45, no. 4, pp. 1431–1441, 2008.

[70] W. Jin, R. R. Taghavi, and S. Farokhi, "Asymmetrical Flow Simulation of Icing Effects in S-Duct Inlets at Angle of Attack," *Int. J. Turbo Jet-Engines*, vol. 28, pp. 93–108, 2011.

[71] A. M. Ferrar, "Measurements of Flow in Boundary Layer Ingesting Serpentine Inlets," Master's thesis, Virginia Polytechnic Institute and State University, 2011.

[72] F. Papadopoulos, I. Valakos, and I. K. Nikolos, "Design of an S-Duct Intake for UAV Applications," Master's thesis, Technical Univeristy of Crete, 2012.

[73] N. J. Georgiadis and D. A. Yoder, "Recalibration of the Shear Stress Transport Model to Improve Calculation of Shock Seperated Flow," *51st Aerospace Sciences Meeting sponsored by the American Institute of Aeronautics and Astronautics*, no. AIAA-2013-0685, 2013.

[74] D. Gil-Prieto, D. G. MacManus, P. K. Zachos, G. Tanguy, F. Wilson, and N. Chiereghin, "Delayed Detached-Eddy Simulation and Particle Image Velocimetry Investigation of S-Duct Flow Distortion," *AIAA Journal*, vol. 55, no. 6, pp. 1893–1908, 2017, 10.2514/1.J055468.

[75] D. Gil-Prieto, D. G. MacManus, P. K. Zachos, and G. Tanguy, "Convoluted Intake Distortion Measurements Using StereoParticle Image Velocimetry," *AIAA Journal*, vol. 55, no. 6, pp. 1878–1894, 2017.

[76] D. G. MacManus, N. Chiereghin, D. Gil-Prieto, and P. K. Zachos, "Complex Aeroengine Intake Ducts and Dynamic Distortion," *AIAA Journal*, vol. 55, no. 7, pp. 2395–2421, 2017.

[77] A. D'Ambros, T. Kipouros, P. Zachos, M. Savill, and E. Benini, "Computational Design Optimization for S-Ducts," *Designs MDPI*, 2018.

[78] D. Gil-Prieto, D. G. MacManus, P. K. Zachos, and A. Bautista, "Assessment Methods for Unsteady Flow Distortion in Aero-Engine Intakes," *Aerospace Science and Technology*, vol. 72, pp. 292–304, 2018.

[79] A. Asghar, R. A. Stowe, W. D. E. Allan, and D. Alexander, "Entrance Aspect Ratio Effect on S-Duct Inlet Performance at High-Subsonic Flow," *J. Eng. Gas Turbines and Power*, vol. 139, no. 052602, 2017.

[80] *Effect of Offset and Length of an S-Duct Diffuser on the Performance of an Inlet with High-Subsonic Flow*, ser. GT 2018, no. GT2018-76661, Charlotte, NC USA, 2017.

[81] A. Asghar, R. A. Stowe, W. D. E. Allan, and D. Alexander, "Performance Evaluation of an S-Duct Diffuser of a Flight-Vehicle Inlet in High-Subsonic Flow," in *Proceedings of ASME Turbo Expo 2015: Turbine Technical Conference and Exposition*, no. GT2015-43740, 2015.

[82] *Pressure Equalization Method for Passive Flow Control of an S-Duct Intake for High Subsonic Speeds*, no. GT2018-75793, Oslo, Norway, 2018.

[83] A. Hancock, "Delayed Detached Eddy Simulations in Transonic S-Duct Diffusers and Flow Characteristics of a Transonic Y-Shaped Diffusing Duct," Masters Thesis, Durham University, Apr. 2020.

[84] D. J. McConalogue and R. S. Srivastava, "Motion of a Fluid in a Curved Tube," *Proceedings of the Royal Society of London. Series A. Mathematical and Physical Sciences*, vol. 307, no. 1488, pp. 37–53, 1968, the Royal Society London.

[85] A. Hellsten, "Some Improvements in Menter's k-ω SST Turbulence Model," *AIAA Fluid Dynamics*, no. AIAA-98-2554, 1997.

[86] D. D. Apsley and M. A. Leschziner, "Advanced Turbulence Modelling of Separated Flow in a Diffuser," *Flow, Turbulence and Combustion*, vol. 63, pp. 81–112, 1999.

[87] N. E. May, "A New Vortex Generator Model for Use in Complex configuration CFD Solvers ," *AIAA: 19th Applied Aerodynamics Conference*, no. AIAA-2001-2434, 2001.

[88] D. K. Beale, K. B. Cramer, and P. S. King, "Development of Improved Methods for Simulating Aircraft Inlet Distortion in Turbine Enigne Ground Tests," *22nd AIAA Aerodynamic Measurement Technology and Ground Testing Conference*, no. AIAA-2002-3045, 2002.

[89] R. D. D. Menzies, K. J. Badcock, G. N. Barakos, and B. E. Richards, "Validation of the Simulation of Flow in an S-Duct," *20th AIAA Applied Aerodynamics Conference*, no. AIAA 2002-2808, 2002.

[90] K. Sasha, S. N. Singh, V. Seshadri, and S. Mukhopadhyay, "Computational Analysis on Flow Through Transonic S-Diffusers: Effect of Inlet Shape," *J. of Aircraft*, vol. 44, no. 1, pp. 187–194, 2007.

[91] G. A. Gerolymos and I. Vallet, "Reynolds-Stress Model Prediction of 3-D Duct Flows," *Flow Turbulence Combustion*, vol. 96, pp. 45–93, 2016.

[92] D. Gil-Prieto, D. G. MacManus, P. K. Zachos, G. Tanguy, F. Wilson, and N. Chiereghi, "Dynamic Flow Distortion Investigation in an S-duct Using DDES and SPIV Data," *34th AIAA Applied Aerodynamics Conference*, no. AIAA 2016-3562, 2016.

[93] P. Aref, M. Goreyshi, A. Jirasek, and M. J. Satchell, " CFD Validation and Flow Control of RAE-M2129 S-Duct Diffuser Using CREATE - AV Kestrel Simulation Tools," *MDPI Aerospace*, vol. 5, no. 31, 2018.

[94] T. Hickling, "Full Set of Tubercle Results," unpublished Presentation at Durham University, UK.

[95] A-Tech Instruments Ltd, *MicroDaq 2 Pressure Scanner*, Jun. 2015.

[96] MathWorks, "Savitzky-Golay Filtering," 2021. [Online]. Available: https://www.mathworks.com/help/signal/ref/sgolayfilt.html

[97] D. Gil-Prieto, P. K. Zachos, D. G. MacManus, and G. McLelland, "Unsteady Characteristics of S-Duct Intake Flow Distortion," *Aerospace Science and Technology*, vol. 84, pp. 938–952, 2019.

[98] ANSYS Inc, "4.5.1 Standard k- ω Model," 2009. [Online]. Available: https://www.afs.enea.it/project/neptunius/docs/fluent/html/th/node66.htm

[99] M. Schneider, "Delayed Detached Eddy Simulations and Passive Flow Control in Transonic S-Duct Diffusers," Apr. 2019, Durham University Masters of Engineering Research Project, 2019.

[100] R. J. Moffat, "Describing the Uncertainties in Experimental Results," *Experimental Thermal and Fluid Science*, vol. 1, no. 1, pp. 3–17, 1988.

[101] S. Kline and F. Mcclintock, "Describing Uncertainties in Single-Sample Experiments," *Mechanical Engineering*, vol. 75, pp. 3–8, 1953.

Appendices

A Uncertainty Analysis

The uncertainty analysis is presented for each flow control metric equation. The equations are presented with partial derivatives for each variable, then combined for the uncertainty equation based on the root-sum-square (RSS) method with partial derivatives using the technique developed by Moffat, and Kline and McClintock [100, 101]. The uncertainties for each variable are presented in Table A.1 based on averaging the *AeroProbe* data with 1500 points and the μ-*DAQ* data with 600 points.

Table A.1: Uncertainty for variables using averaging of points

Variable	Value	Unit
δ_u	2.30×10^{-5}	$\frac{\text{m}}{\text{s}}$
δ_v	2.30×10^{-5}	$\frac{\text{m}}{\text{s}}$
$\delta_{p_{s,x}}$	7.03×10^{-4}	kPa
$\delta_{p_{s,1}}$	7.03×10^{-4}	kPa
$\delta_{p_{0,1}}$	8.96×10^{-4}	kPa
$\delta_{p_{0,j}}$	5.14×10^{-3}	kPa
$\delta_{p_{s,2}}$	8.96×10^{-1}	kPa
$\delta_{p_{0,2,i,k}}$	8.96×10^{-1}	kPa
$\delta_{p_{0,2,i}}$	8.96×10^{-1}	kPa
$\delta_{p_{0,2}}$	8.96×10^{-1}	kPa

A.1 Coefficient of Static Pressure

This section presents the uncertainty calculation for the coefficient of static pressure. The coefficient of static pressure is based on Equation 4.1, repeated here as Equation A.1, and the partial derivative of each variable can be taken shown below.

$$C_p = \frac{p_{s,x} - p_{s,1}}{p_{0,1} - p_{s,1}} \tag{A.1}$$

$$\frac{\partial C_p}{\partial p_{0,1}} = \frac{p_{s,x} - p_{s,1}}{(p_{0,1} - p_{s,1})^2} \tag{A.2}$$

$$\frac{\partial C_p}{\partial p_{s,x}} = \frac{1}{p_{s,1} - p_{0,1}} \tag{A.3}$$

$$\frac{\partial C_p}{\partial p_{s,1}} = \frac{p_{0,1} - p_{s,x}}{(p_{0,1} - p_{s,1})^2} \tag{A.4}$$

The uncertainty can then be calculated for the coefficient of pressure using these equations and the values in Table A.1.

$$\delta_{C_p} = \sqrt{\left(\frac{\partial C_p}{\partial p_{0,1}}\delta_{p_{0,1}}\right)^2 + \left(\frac{\partial C_p}{\partial p_{s,x}}\delta_{p_{s,x}}\right)^2 + \left(\frac{\partial C_p}{\partial p_{s,1}}\delta_{p_{s,1}}\right)^2} \tag{A.5}$$

The coefficient of pressure uncertainty is on the order of magnitude of 10^{-4} which cannot be visibly plotted on the C_p figures, for this reason, the uncertainty is noted but not shown.

A.2 Total Pressure Coefficient

The total pressure coefficient is calculated using Equation 4.2, repeated here as Equation A.6, where the uncertainty can be found with the partial derivatives, shown below.

$$\pi = \frac{\bar{p}_{0,2}}{\bar{p}_{0,1}} \tag{A.6}$$

$$\frac{\partial \pi}{\partial \bar{p}_{0,2}} = \frac{1}{p_{0,1}} \tag{A.7}$$

$$\frac{\partial \pi}{\partial \bar{p}_{0,1}} = -\frac{p_{0,2}}{(p_{0,1})^2} \tag{A.8}$$

The uncertainty can then be calculated for the total pressure coefficient using these equations and the values in Table A.1.

$$\delta_\pi = \sqrt{\left(\frac{\partial \pi}{\partial \bar{p}_{0,2}} \delta_{\bar{p}_{0,2}}\right)^2 + \left(\frac{\partial \pi}{\partial \bar{p}_{0,1}} \delta_{\bar{p}_{0,1}}\right)^2} \tag{A.9}$$

A.3 Distortion Coefficient

The distortion coefficient is calculated using Equation 4.3 where the partial derivative can be taken for each variable, shown below.

$$DC(60) = \frac{\bar{p}_{0,2} - \bar{p}_{0,j}}{\bar{p}_{0,2} - \bar{p}_{s,2}} \tag{A.10}$$

$$\frac{\partial DC(60)}{\partial \bar{p}_{0,2}} = \frac{\bar{p}_{0,j} - \bar{p}_{s,2}}{(\bar{p}_{0,2} - \bar{p}_{s,2})^2} \tag{A.11}$$

$$\frac{\partial DC(60)}{\partial \bar{p}_{0,j}} = \frac{1}{\bar{p}_{s,2} - \bar{p}_{0,2}} \tag{A.12}$$

$$\frac{\partial DC(60)}{\partial \bar{p}_{s,2}} = \frac{\bar{p}_{0,2} - \bar{p}_{0,j}}{(\bar{p}_{0,2} - \bar{p}_{s,2})^2} \tag{A.13}$$

The uncertainty can then be calculated for the distortion coefficient using the above equations and values in Table A.1.

$$\delta_{DC(60)} = \sqrt{\left(\frac{\partial DC(60)}{\partial \bar{p}_{0,2}}\delta_{p_{0,2}}\right)^2 + \left(\frac{\partial DC(60)}{\partial \bar{p}_{0,j}}\delta_{p_{0,j}}\right)^2 + \left(\frac{\partial DC(60)}{\partial \bar{p}_{s,2}}\delta_{p_{s,2}}\right)^2} \tag{A.14}$$

A.4 Radial Distortion Coefficient

The distortion coefficient is calculated using Equation 4.3, repeated here as Equation A.15, where the partial derivative can be taken for each variable, shown below.

$$DRPR_{\max} = \frac{\bar{p}_{0,2} - \bar{p}_{0,2,i}}{\bar{p}_{0,2}} \tag{A.15}$$

$$\frac{\partial DRPR_{\max}}{\partial \bar{p}_{0,2}} = \frac{\bar{p}_{0,2,i}}{\bar{p}_{0,2}} \tag{A.16}$$

$$\frac{\partial DRPR_{\max}}{\partial \bar{p}_{0,2,i}} = -\frac{1}{\bar{p}_{0,2}} \tag{A.17}$$

The uncertainty can then be calculated for the radial distortion coefficient using these equations and the values in Table A.1.

$$\delta_{DRPR_{\max}} = \sqrt{\left(\frac{\partial DRPR_{\max}}{\partial \bar{p}_{0,2}}\delta_{p_{0,2}}\right)^2 + \left(\frac{\partial DRPR_{\max}}{\partial \bar{p}_{0,2,i}}\delta_{p_{0,2,i}}\right)^2} \tag{A.18}$$

A.5 Angular Distortion Coefficient

The angular distortion coefficient is a piece-wise function and the uncertainty was calculated accordingly. The partial derivatives, based on Equation 4.5, repeated as Equation A.19, are shown below.

$$C_\theta = \frac{1}{5}\sum_{i=1}^{5}\left(1 - \frac{\sum_{k=1}^{12}\begin{cases}\frac{\bar{p}_{0,2,i,k}}{\bar{p}_{0,2,i}}, & \bar{p}_{0,2,i,k} < \bar{p}_{0,2,i} \\ 0 & \bar{p}_{0,2,i,k} \geq \bar{p}_{0,2,i}\end{cases}}{\sum_{k=1}^{12}\begin{cases}1 & \bar{p}_{0,2,i,k} < \bar{p_0}_{,2,i} \\ 0 & \bar{p}_{0,2,i,k} \geq \bar{p}_{0,2,i}\end{cases}}\right) \tag{A.19}$$

$$\frac{\partial C_\theta}{\partial p_{0,2,i,k}} = \frac{1}{5}\sum_{i=1}^{5}\left(1 - \frac{\sum_{k=1}^{12}\begin{cases}-\frac{1}{p_{0,2,i}}, & \bar{p}_{0,2,i,k} < \bar{p}_{0,2,i} \\ 0 & \bar{p}_{0,2,i,k} \geq \bar{p}_{0,2,i}\end{cases}}{\sum_{k=1}^{12}\begin{cases}1 & \bar{p}_{0,2,i,k} < \bar{p_0}_{,2,i} \\ 0 & \bar{p}_{0,2,i,k} \geq \bar{p}_{0,2,i}\end{cases}}\right) \tag{A.20}$$

$$\frac{\partial C_\theta}{\partial p_{0,2,i}} = \frac{1}{5}\sum_{i=1}^{5}\left(1 - \frac{\sum_{k=1}^{12}\begin{cases}\frac{p_{0,2,i,k}}{(p_{0,2,i})^2}, & \bar{p}_{0,2,i,k} < \bar{p}_{0,2,i} \\ 0 & \bar{p}_{0,2,i,k} \geq \bar{p}_{0,2,i}\end{cases}}{\sum_{k=1}^{12}\begin{cases}1 & \bar{p}_{0,2,i,k} < \bar{p_0}_{,2,i} \\ 0 & \bar{p}_{0,2,i,k} \geq \bar{p}_{0,2,i}\end{cases}}\right) \tag{A.21}$$

The uncertainty can then be calculated for the angular distortion coefficient using these equations and the values in Table A.1.

$$\delta_{C_\theta} = \sqrt{\left(\frac{\partial C_\theta}{\partial p_{0,2,i,k}}\delta_{p_{0,2,i,k}}\right)^2 + \left(\frac{\partial C_\theta}{\partial p_{0,2,i}}\delta_{p_{0,2,i}}\right)^2} \tag{A.22}$$

A.6 Swirl Index

The uncertainty for the swirl index, calculated with Equation 4.7, repeated as Equation A.23, can be found using the RSS method with partial derivatives, shown below.

$$SI = \text{atan}\left(\frac{v_\theta}{u}\right) \tag{A.23}$$

$$\frac{\partial SI}{\partial v_\theta} = \frac{u^2}{v_\theta^2 + u^2} \tag{A.24}$$

$$\frac{\partial SI}{\partial u} = -\frac{v_\theta^2}{v_\theta^2 + u^2} \tag{A.25}$$

The uncertainty can then be calculated for the swirl index using these equations and the values in Table A.1.

$$\delta_{SI} = \sqrt{\left(\frac{\partial SI}{\partial v_\theta}\delta_{v_\theta}\right)^2 + \left(\frac{\partial SI}{\partial u}\delta_u\right)^2} \tag{A.26}$$

A.7 Swirl Directivity

The uncertainty for the swirl directivity, calculated with Equation 4.10, repeated as Equation A.27, can be found using the RSS method with partial derivatives, shown below.

$$SD = \frac{\overline{\alpha}}{\overline{|\alpha|}} \tag{A.27}$$

$$\frac{\partial SD}{\partial \overline{|\alpha|}} = \frac{\partial SI}{\partial \overline{|\alpha|}} \tag{A.28}$$

$$\frac{\partial SD}{\partial \overline{|\alpha|}} = \frac{1}{\frac{\partial SD}{\partial \overline{|\alpha|}}} \tag{A.29}$$

The uncertainty can then be calculated for the swirl directivity using these equations and the values in Table A.1.

$$\delta_{SD} = \sqrt{\left(\frac{\partial SD}{\partial \overline{|\alpha|}}\delta_\alpha\right)^2 + (\frac{\partial SD}{\partial \overline{|\alpha|}}\delta_\alpha)^2} \tag{A.30}$$

A.8 Swirl Pairs

The uncertainty for the swirl pair coefficient, calculated with Equation 4.12, repeated as Equation A.31, can be found using the RSS method with partial derivatives, shown below.

$$SP = \frac{\overline{|\alpha|}}{2 \times \max\left[|\overline{\alpha^-}|, |\overline{\alpha^+}|\right]} \tag{A.31}$$

$$\frac{\partial SP}{\partial \overline{|\alpha|}} = \frac{\partial SI}{\partial \overline{|\alpha|}} \tag{A.32}$$

$$\frac{\partial SP}{\partial \overline{|\alpha^-|}} = \frac{1}{\frac{\partial SP}{\partial \overline{|\alpha|}}} \tag{A.33}$$

$$\frac{\partial SP}{\partial \overline{|\alpha^+|}} = \frac{1}{\frac{\partial SP}{\partial \overline{|\alpha|}}} \tag{A.34}$$

The uncertainty can then be calculated for the swirl pair coefficient using these equations and the values in Table A.1. Equation A.35 and A.36 are used in cases that α^- or α^+ are used, respectively.

$$\delta_{SP} = \sqrt{\left(\frac{\partial SP}{\partial \overline{|\alpha|}}\delta_\alpha\right)^2 + \left(\frac{\partial SP}{\partial \overline{|\alpha^-|}}\delta_\alpha\right)^2} \tag{A.35}$$

$$\delta_{SP} = \sqrt{\left(\frac{\partial SP}{\partial \overline{|\alpha|}}\delta_\alpha\right)^2 + \left(\frac{\partial SP}{\partial \overline{|\alpha^+|}}\delta_\alpha\right)^2} \tag{A.36}$$